DEPARTAMENTO DE FISIOLOGÍA MÉDICA Y BIOFÍSICA

FACULTAD DE MEDICINA

UNIVERSIDAD DE SEVILLA

INSITUTO DE BIOMEDICINA DE SEVILLA

Hypoxia and Alzheimer's disease: the processing of amyloid precursor protein and the role of prolyl-hydroxylase 3 in microglia

Trabajo presentado para optar al grado de Doctor

por la Universidad de Sevilla, 2018.

Manuel Alejandro Sánchez García

Contents

1. Abbreviations

AD	Alzheimer's disease	IβS	Interferon-β-induced signature
ADAM	A disintegrin metalloprotease	logFC	Log_2 Fold change
APH	Anterior pharynx defective	MCI	Mild-cognitive impairment
ASH	Acute sustained hypoxia	MDM	Monocyte-derived macrophage
ATP	Adenosine triphosphate	MPI	Microglia proximity index
Aβ	Amyloid-β	NF-κB	Nuclear factor-κB
AβPP	Amyloid-β precursor protein	NFTs	Neurofibrillary tangles
BSA	Bovine serum albumin	O_2	Oxygen
C83 or αCTF	α C-terminal fragment	*p*	P-value
C99 or βCTF	B C-terminal fragment	PBS	Phosphate-buffered saline
CNS	Central Nervous System	PCR	Polymerase Chain Reaction
CO_2	Carbon dioxide	PHD	Prolyl 4-hydroxylase domain
COPD	Chronic obstructive pulmonary disease	PS	Presinilin
CSH	Chronic sustained hypoxia	P-Tau	Hyperphosphorylated-Tau
dH_2O	Distilled water	qRT-PCR	Reverse transcription real-time polymerase chain reaction
dNTP	Deoxyribonucleotide	ROS	Reactive oxygen species
FACS	Fluorescence-activated cell sorting	sAD	Sporadic Alzheimer's disease
fAD	Familial Alzheimer's disease	SDS-PAGE	Sodium dodecyl sulfate polyacrylamide gel electrophoresis
fAβ	Fibrillar amyloid-β	sAβPPα	Soluble amyloid-β precursor protein α
FIH	Factor inhibiting HIF	sAβPPβ	Soluble amyloid-β precursor protein β
GSEA	Gene set enrichment analyses	Thio-S	Thioflavine-S
GWAS	Genome-wide association studies	TNFα	Tumor necrosis factor α
HIF	Hypoxia-inducible factor	TLR	Toll-like receptor
HMS	Hypoxia-induced microglia signature	VEGF	Vascular endothelial growth factor
HREs	Hypoxia-response elements	VHL	von Hippel-Lindau tumor suppressor
IDE	Insulin-degrading enzyme	WB	Western blot
IFN	Interferon		

2. Introduction

2.1. Alzheimer's disease

2.1.1. Main hallmarks and physiopathology

Frau Auguste Deter, a 51-year-old patient with aphasia and memory loss, was admitted at Frankfurt Asylum in 1901, where Dr. Alois Alzheimer got interested in her clinical picture. After her death, in 1907, Dr. Alois Alzheimer published his "Peculiar Disease of the Cerebral Cortex", a histological analysis of Auguste's brain cortex describing deposits of plaques and fibrils rearranged into bundles and networks. He had just made the first description of a frequent kind of dementia in the elderly and its main histopathological hallmarks; a condition that was deservedly named after him as Alzheimer's disease (AD) (Hunting, 2015; Kay et al., 1964; Strassnig & Ganguli, 2005).

Patients suffering from this progressive neurodegenerative disease show extensive cortical atrophy, presumably causing subsequent dementia, and prominent lateral ventricles enlargement (Dickerson et al., 2009). The presence of microinfarctions is also frequent, as cerebrovascular disorders are usually linked to aging in general and AD in particular (Serrano-Pozo et al., 2011). Microscopically, AD is characterized by the presence of extracellular protein deposits called amyloid plaques and dystrophic neurites containing fibers of hyperphosphorylated Tau (P-Tau) protein called neurofibrillary tangles (NFTs), which can also appear as extracellular aggregates. These AD distinctive features correlate with microglial activation, astrogliosis, synapse loss, and neuronal damage, which culminate in dementia. Particularly, vascular dysregulation and synapse loss are considered as the more predictive features for cognitive decline in the disease (DeKosky & Scheff, 1990; Iturria-Medina et al., 2016).

Amyloid plaques emerge from accumulation, aggregation, and deposition of amyloid-β (Aβ) peptides and display diverse morphology and neuronal toxicity. In spite of the different attempts to chronologically classify amyloid plaques on the basis of their formation and evolution, a more practical approach has been used to

discriminate between two main types of amyloid plaques according to their staining properties and morphology. Dense-core plaques exhibit Thioflavine-S (Thio-S) staining due to their β-sheet structure and are associated with neuronal damage and glial activation (Itagaki et al., 1989; Serrano-Pozo, Muzikansky, et al., 2013). These dense-core plaques can be subsequently subdivided into filamentous plaques or compact plaques. Dense-core filamentous plaques exert higher toxic effects on surrounding neurons than compact plaques due to their more fibrillar conformation (Yuan et al., 2016). Unlike dense-core plaques, diffuse plaques cannot be visualized upon Thio-S staining and do not display surrounding neuronal damage. Indeed, diffuse plaques are a frequent aging-related feature in cognitively healthy subjects. Interestingly, even though dense-core amyloid plaques produce neuronal damage, there is no clear association between plaque burden and the degree of cognitive impairment (Arriagada et al., 1992; Giannakopoulos et al., 2003).

On the other hand, microtubule-associated Tau protein in a misfolded and hyperphosphorylated state constitute the main component of NFTs. The hyperphosphorylation event takes place in specific regions of tau protein and it has been suggested to precede tau protein aggregation (Augustinack et al., 2002). The NFTs can be found within neurons as diffuse puncta that do not correlate with evident neuronal alterations or as inner neuronal fibrils that impair neuronal morphology. Extracellular NFTs emerge from tangle-bearing neurons death (Braak et al., 1994; Su et al., 1993). Both the amount and distribution of NFTs parallel AD neurodegeneration and corresponding cognitive decline, although it is unclear whether it constitutes an essential step for subsequent neuronal death or a protective mechanism exerted by neurons (Bierer et al., 1995; Serrano-Pozo et al., 2011).

Despite the massive amount of data generated regarding AD in the last century, we barely understand the molecular mechanisms involved in this disease that affects more than 24 million people worldwide. Available approved treatments target AD symptoms but cannot slow down the disease progression, and future perspectives include a 4-fold increase in AD prevalence in the next 40 years (Farlow et al., 2008). Therefore, AD represents one of the biggest challenges for public health and

involves remarkable economical issues, what justifies the intense search for underlying causative mechanisms to target this disorder (Kumar et al., 2015; Reitz & Mayeux, 2014).

2.1.2. Aβ accumulation

Aβ peptides are produced in physiological conditions and cleared by different mechanisms, but their accumulation and deposition occur upon imbalance between Aβ generation and removal by degradation and drainage (Hardy et al., 2002; Selkoe & Dennis, 2003; Tarasoff-Conway et al., 2015; Zlokovic et al., 2000). Aβ generation can result from sequential cleavages of Aβ precursor protein (AβPP), a type-I transmembrane protein encoded in *App* gene, which is located in human chromosome 21 (**Figure 1**) (George-Hyslop et al., 1987; Zhang et al., 2011). Despite having been extensively studied, the physiological function of AβPP remains largely elusive. In this sense, several functions have been proposed for AβPP protein including synaptogenesis, neurite outgrowth, cell adhesion, protein trafficking and signaling receptor but most of these functions require further *in vivo* validation (Zheng & Koo, 2006).

AβPP can be processed by α-cleavage or β-cleavage. The non-amyloidogenic pathway, the main route of Aβ processing, is initiated by α-cleavage of AβPP in the plasma membrane. This proteolytic activity takes place within the Aβ domain of AβPP, preventing Aβ generation and producing a large soluble peptide called soluble amyloid precursor protein α (sAβPPα), with reported neurotrophic activities, and an 83 amino acid C-terminal fragment (αCTF or C83) with no clear functions (Nhan et al., 2015; Sisodia, 1992). The A disintegrin and metalloprotease (ADAM) family members ADAM9, ADAM10, and ADAM17/TACE are located in the plasma membrane and carry out the α-cleavage, although the main α-secretase activity is catalyzed by ADAM10. αCTF constitutes the substrate for ɣ-secretase complex, which is integrated by four different subunits: presenilin (PS) 1 or PS2, nicastrin, PS enhancer 2 and anterior pharynx defective 1a or 1b (APH1a or APH1b) (De Strooper et al., 2012). P83 and AICD fragments result from the catalytic activity of this complex. Unlike P83, which is rapidly degraded, AICD has been proposed to possess signal transduction functions. In the presence of

caspases, AICD can be subsequently cleaved, releasing C31 fragment, which exerts cytotoxic effects (Park et al., 2009).

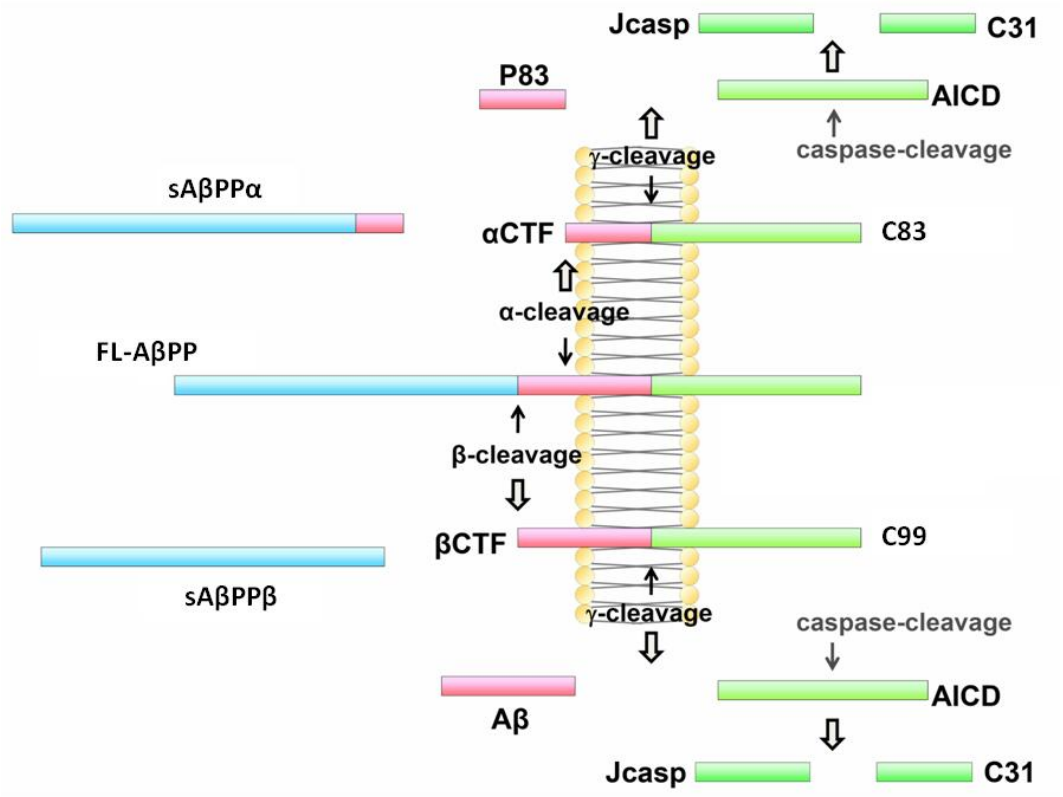

Figure 1. Schematic diagram of amyloid-β precursor protein (AβPP) processing, adapted from Zhang et al., 2011 (Y. Zhang et al., 2011).

In the non-amyloidogenic AβPP processing, sequential α-cleavage and ɣ-cleavage prevent amyloid-β (Aβ) production. In the amyloidogenic AβPP processing, β-cleavage conserves intact Aβ peptide structure and ɣ-cleavage separates different Aβ peptide versions from AICD fragment. sAβPPα, soluble amyloid-β precursor protein α; sAβPPβ, soluble amyloid-β precursor protein β; αCTF or C83, α C-terminal fragment; βCTF or C99, β C-terminal fragment.

The amyloidogenic pathway originates from β-cleavage of AβPP by BACE1, considered as the rate-limiting enzyme for Aβ generation. This enzyme catalyzes the cleavage of AβPP by proteolysis in a different position from α-cleavage that keeps intact the Aβ peptide within a longer fragment of 99 amino acids C-terminal fragment (βCTF or C99). Unlike sAβPPα, the soluble peptide produced upon BACE1 proteolytic cleavage of AβPP called soluble amyloid precursor protein β (sAβPPβ) does not seem to show neurotrophic functions. β-cleavage is followed by ɣ-cleavage, what results in AICD and Aβ peptides production of different lengths,

being $A\beta_{1-40}$ and $A\beta_{1-42}$ the most frequent ones (Haass et al., 2012; Saido & Leissring, 2012; Zhang et al., 2011; Zheng & Koo, 2006).

Aβ can be cleared from the brain by various overlapping and interacting clearance systems including cellular uptake and enzymatic degradation, transport across the blood–brain barrier and blood–cerebrospinal fluid barrier, interstitial fluid bulk flow, and cerebrospinal fluid absorption into the circulatory and lymphatic systems (Tarasoff-Conway et al., 2015). However, experimental evidence suggests that the contribution of Aβ-degrading enzymes to counterbalance Aβ production through irreversible catalysis is of particular relevance. Neprilysin and insulin-degrading enzyme (IDE) are both among the most relevant and extensively characterized Aβ-degrading enzymes. Although IDE is a ubiquitously expressed protein in the brain, neprilysin expression is restricted to neuronal presynaptic terminals (Fukami et al., 2002; Jha et al., 2015). On the other hand, BACE2 protein is the Aβ-degrading enzyme with the highest *in vitr*o capacity of Aβ proteolysis and is expressed in glial cells, but not in neurons (Saido & Leissring, 2012).

2.1.3. Etiology and epidemiology

AD cases are classified into familial AD (fAD) or sporadic AD (sAD) according to their etiology. fAD represents a 4 % of all AD cases and is caused by autosomal dominant mutations that directly impact on AβPP processing. These mutations affect *App* gene, encoding for AβPP, *Psen1* gene, encoding for PS1, or *Psen2* gene, encoding for PS2. As a result, patients carrying these mutations increase Aβ generation, leading to fAD, cerebral amyloid angiopathy or both (Bettens et al., 2013; Rovelet-Lecrux et al., 2006). Therefore, a scenario of pure Aβ accumulation-driven AD is provided by these mutations in which amyloid plaque formation precedes vascular pathology, NFTs, neuronal damage, and dementia. In this sense, the amyloid cascade hypothesis was proposed by Hardy and Higgins, claiming that Aβ deposition was the causative event for AD pathology. Accordingly, Aβ accumulation leads to downstream effects and eventual dementia (Hardy & Higgins, 1992).

On the other hand, the vast majority of AD cases are classified as sAD because the upstream events leading to Aβ accumulation remain unknown. Genome-Wide

Association Studies (GWAS) performed in different cohorts of patients have revealed that genetic modifications altering endolysosomal function, lipid metabolism or immune response are more likely to predispose to sAD. Genetic polymorphisms in *Clu*, *Cr1*, *Picalm*, *Bin1*, *Epha1*, *Abca7*, *Cd33 or Trem2* genes are among the alleles implicated in endolysosomal, lipid metabolism and immune responses impairment associated with sAD. In particular, the most relevant genetic risk factor for sAD is *Apoe* ε4 allele, encoding for the most abundant apolipoprotein in the human brain and involved in lipid transport and metabolism, Aβ aggregation and clearance, synaptic plasticity, and neuroinflammation (Pimenova et al., 2018).

In spite of the increasing number of risk genetic factors identified, a growing body of evidence involves epigenetic modifications and environment as essential determinants in the development sAD (Bettens et al., 2013; Corder et al., 1993; Pimenova et al., 2018; Yu et al., 2014). In this sense, population-based studies on demented subjects reported a correlation between the combination of AD and cerebrovascular impairment and dementia (Neuropathology Group. Medical Research Council Cognitive Function and Aging Study, 2001; Schneider et al., 2007). Indeed, several studies suggest that factors predisposing to cerebrovascular disease or stroke are also associated with AD, although the precise link between these conditions is unclear. Among these factors, atrial fibrillation, atherosclerosis, and diabetes are common predisposing conditions for both AD and ischemic stroke in the elderly. In fact, *Apoe* ε4 allele expression not only increases AD development but also induces a 3-fold increase in vascular disease (Kalaria, 2000).

Recent epidemiological studies have specifically reported comorbidity between hypoxia-associated conditions and dementia. Resulting hypoxia from sleep-disordered breathing old patients consistently associated with dementia and mild cognitive impairment (MCI) (Yaffe et al., 2011). Studies on chronic obstructive pulmonary disease (COPD) have also revealed an increased risk of MCI and dementia that is proportional to duration the of COPD (Rusanen et al., 2013; Singh et al., 2014). In contrast, treatment with continuous positive airway pressure to obstructive sleep apnea patients also suffering from AD, slows down or even improves cognitive impairment (Cooke et al., 2009).

Results	Behavior	NA	NA	NA	NA	↓ MWM	NA	NA	NA	NA	NA	= MWM	NA	↓ MWM, ↓ TST + OF	↓ MWM	NA	↓ MWM
	Synapses	NA	NA	NA	NA	NA	NA	NA	NA	NA	NA	NA	NA	NA	↓ syn., ↓ EM	NA	↓ syn., ↓ EM
	Tau	↑ tau	NA	NA	NA	NA	NA	NA	NA	NA	NA	NA	NA	↑ p-tau, = tau	↑ p-tau	NA	= NFT number; ↑ p-tau/tau ratio (at 4 mo)
	Neprilysin	NA	NA	NA	NA	NA	NA	NA	NA	NA	NA	NA	NA	NA	↓ Neprilysin	↓ *Mme*, ↓ Neprilysin level & activity	↓ Neprilysin
	Aβ	↑ Aβ	↑ $Aβ_{40}$, ↑ $Aβ_{42}$	↑ $Aβ_{40}$, ↑ $Aβ_{42}$	↑ $Aβ_{40}$, ↑ $Aβ_{42}$, ↑ plaque number	NA	↑ $Aβ_{42}$	↑ soluble & FA-$Aβ_{42}$, ↑ plaque area & number	NA	NA	↑ $Aβ_{42}$, ↑ intraneuronal Aβ, = $Aβ_{40}$	↑ $Aβ_{40}$ = $Aβ_{42}$	↑ $Aβ_{42}$, ↑ plaque area & number	↑ soluble & FA hu $Aβ_{42}$ & $Aβ_{40}$, ↑ soluble mu $Aβ_{42}$ & $Aβ_{40}$, ↑ plaque area & number	NA	↑ soluble & FA hu $Aβ_{42}$/$Aβ_{40}$ ratio, ↑ plaque area & number
	γ-secretase	NA	↑ Presenilin-1	NA	NA	NA	↑ *Aph1a* & Aph1a, = Presenilin-1, = Nicastrin, = Pen2	= Presenilin 1	↑ Aph-1a	NA	↑ *Psen1*, ↑ *Psen2*	NA	NA	NA	NA	NA	↑ Aph1a, ↑ Nicastrin, ↑ Pen2, = Presenilin-1
	BACE	NA	NA	↑ *Bace1* & Bace1	NA	↑ *Bace1* (in wt)	NA	↑ *Bace1* & Bace1	NA	↑ *Bace1* & Bace1	↑ *Bace1*	= Bace1	NA	NA	= Bace1	NA	↑ Bace1 (in wt)
	APP	↑ AβPP	NA	↑ C99	↑ C99	↑ C99	↑ sAβPPwt, = AβPP, ↓ AβPP-CTFs	↑ C99, = AβPP	↓ HA-C99	↑ C99/C83 ratio	↑ Appa, ↑ Appb	= AβPP	NA	NA	NA	NA	↑ AβPP, = C99/C83 ratio
CO_2 level		5%	5%	5%	5%	NA	5%	NA	5%	NA	5%	NA	5%	NA	NA	NA	NA
Hypoxia duration		4 & 8 h followed by 20% O_2 for 24 or 48 h	24 h	12 & 24 h	12 h	16 h/day for 1 mo	2, 4, 8, 12 & 20 h	2, 4 & 8 h	4 h	Once daily for 60 d	1, 3, 6, 12, 24, 48 & 72 h	<0.03%	5% vs 21% every 10 min for 8 h per day during 8 weeks	Embryos: from 6 hpf to 24 or 48 hpf stage. Adults: 3 h	1% vs 21% 10 min vs 20 min for 8 cycles	Once daily for 60 d	6 h/day for 7 to 20 of gestation followed by normoxia up to age 3, 6 & 9 mo	6 h/day for 30 d followed by up to 5 mo normoxia prior to sacrifice
Hypoxia level		NA	2.5% O_2	2% O_2	2% O_2	8% O_2	NA	1% O_2	NA	NA, until "first gasping breath"	3% O_2	5% O_2	Embryos: ≈10% of controls, Adults: ≈17% of controls	1% O_2	NA, until "first gasping breath"	11.1% O_2	11.1% O_2
Hypoxia method		Sealed but not 100% leak-proof* chamber	Incubator	Incubator	Incubator	Semisealable hypoxia chamber	1 mM $NiCl_2$	Incubator	1 mM $NiCl_2$	Sealed 125 mL jar with fresh air	Incubator	Hypoxia chamber	Bubbling N2 to the medium	Incubator	Sealed 125 mL jar with fresh air	Hypobaric chamber	Hypobaric chamber
Model		Rat cortical neuron primary culture	Rat cortical astrocyte primary culture	SH-SY5S-APP_{swe} cells	HEK-APP_{695wt}	APP23 mice (8 mo, M:F 1:1)	HeLa-APP_{swe} cells	N2a-APP_{695wt} cells	SH-SY5S-C99 cells	APP_{swe}/$PS1_{A246E}$ mice (9 mo, F)	SK-N-BE neuroblastoma cells	3xTg mice (6 mo, M)	Zebra fish embryos & adults	SH-SY5S-APP_{wt} cells	APP_{swe}/$PS1_{dE9}$ mice (6 mo)	APP_{swe}/$PS1_{A246E}$ pregnant mice	NB7 (SJ-N-CG) neuroblastoma cells	APP_{swe}/$PS1_{dE9}$ mice (3 mo)
Author / year		Chen et al. 2003	Smith et al. 2004	Sun et al. 2006			Wang et al. 2006	Zhang et al. 2007	Li et al. 2009		Guglielmotto et al 2009	Shiota et al. 2013	Moussavi Nik et al. 2012		Gao et al. 2013	Zhang et al 2013	Kerridge et al 2015	Liu et al. 2016

Table 1. Literature review on regulation of amyloid-β (Aβ) metabolism by hypoxia (Serrano-Pozo et al., 2017).

Abbreviations: ↓, significant decrease; ↑, significant increase; =, no significant change; d, days; EM, electron microscopy; F, female; FA, formic acid; h, hours; hu, human; M, male; *Mme* = neprilysin mRNA; mo, month; mu, murine; MWM, Morris

water maze (↓ indicates worse performance); NA, not available; NFT, neurofibrillary tangle; OF, open field; syn, synaptophysin; TST, tail suspension test (↓ indicates worse performance). Note, mRNAs are expressed in *Italics*, whereas proteins are Capitalized.

Several studies have attributed this comorbidity between hypoxia-associated conditions and AD to a more pro-amyloidogenic AβPP processing that culminates in increased Aβ accumulation through a number of mechanisms. However, the methodological approaches conducted in these studies were based on *in vitro* models, hypoxia/reoxygenation repetitive cycles, hypobaric chambers, or even asphyxiation strategies (**Table 1**), what can explain the disparity of the results obtained (Chen et al., 2003; Guglielmotto et al., 2009; Li et al., 2009; Sun et al., 2006; Zhang et al., 2013). Therefore, there is a lack of investigations addressing pure hypoxia contribution to AβPP processing and Aβ dynamics *in vivo* under fine-controlled conditions.

2.2. Hypoxia

2.2.1. Hypoxia and response mechanisms

Aerobic organisms require an appropriate oxygen (O_2) supply to maintain systemic and cellular homeostasis. O_2 serves as a substrate for enzymatic activities in signaling pathways and remarkably, constitutes the final electron acceptor in the mitochondrial respiratory chain after oxidative phosphorylation, the main source of energy in form of adenosine triphosphate (ATP) in aerobic organisms. Hypoxia occurs when cell O_2 requirements exceed O_2 delivery from blood, a situation that takes place under physiological and pathological scenarios. In this sense, hypoxic situations are associated to high altitude climbing, many developmental processes, and specific regions of some organs, like the intestinal epithelium (Colgan & Taylor, 2010; Grocott et al., 2009; Semenza, 2012). Even transient or local hypoxemia may result in irreversible damage to cells and tissues, as exemplified by devastating consequences of stroke, myocardial infarction or chronic lung disease. Hence, living organisms exhibit acute and chronic adaptations to minimize the consequences of O_2 insufficiency.

In response to acute hypoxia, various mechanisms sense O_2 decrease and elaborate responses to recover O_2 levels to the normal range. The carotid bodies recognize acute hypoxemic conditions and activate respiratory (hyperventilation) and cardiovascular (cardiac output increase) responses to recover O_2 levels (Lopez-Barneo et al., 2001). Other fast-responding mechanisms involve neuroepithelial bodies and smooth muscle cells from the pulmonary artery. Smooth muscle cells contract the lumen of the vessels of hypoxic regions in the lung to redistribute blood perfusion to oxygenated areas, while dilate peripheral arteries dilate to favor O_2 delivery into tissues (Franco-Obregón & López-Barneo, 1996; Weir & Archer, 1995). In the bronchiolar epithelium, neuroepithelial bodies can send information on hypoxic stimuli to the central nervous system (CNS) (Liu et al., 2014).

Unlike the fast acute hypoxia response systems, the adaptive mechanisms to trigger chronic hypoxia responses take from hours to days. Chronic hypoxia involves hypoxia-inducible factors (HIF)s stabilization, transcription factors that orchestrate complex responses in all metazoan species to enhance O_2 supply to cells and adapt cell physiology to low O_2 tensions (Kaelin & Ratcliffe, 2008).

2.2.2. HIF pathway and its regulation

HIF proteins are heterodimeric transcription factors composed of a constitutive transcribed HIF1β subunit, also known as ARNT, and an α subunit (HIFα) that is unstable in normoxic conditions. Upon α/β dimerization and association to p300 and CBP co-activator proteins, HIF induces the transcription of lots of different genes after binding to DNA regions called hypoxia-response elements (HRE)s. One of the main consequences of HIF transcriptional activation is the shift from a respiratory to a glycolytic metabolism in order to guarantee energy supply in hypoxic conditions. However, many other physiological responses are induced like angiogenesis or erythrocytosis (Kaelin & Ratcliffe, 2008; Schofield & Ratcliffe, 2004; Semenza, 2012). Although three HIFα subunits have been described, HIF1α and HIF2α are the most extensively studied. While HIF1α is ubiquitously expressed, HIF2α presence is more restricted to certain cell types and tissues and *in vivo* studies have attributed specific physiological functions for HIF2α (Patel & Simon, 2008).

Two major post-translational mechanisms are implicated in the regulation of HIFα by affecting both HIFα protein stability and transcriptional activity (**Figure 2**).

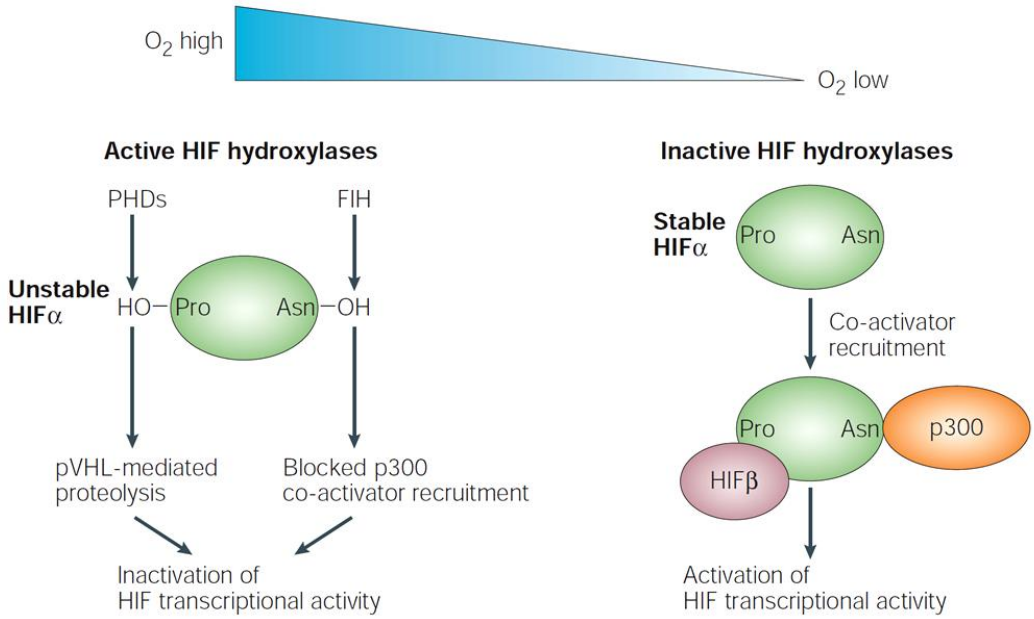

Figure 2. Regulation of Hypoxia-inducible factor (HIF) protein stability and transcriptional activity by oxygen (O2) (Schofield & Ratcliffe, 2004).

In the presence of O_2, prolyl-hydroxylases (PHDs) hydroxylate HIFα, marking it for proteosomal degradation *via* von Hippel-Lindau (VHL) ubiquitination. Moreover, factor inhibiting HIF (FIH) hydroxylates HIF preventing its transcriptional activity. Conversely, in low O_2 conditions, HIF activates transcription of its target genes since hydroxylases are inactive. Pro, proline; Asn, asparagine.

Different members of the prolyl 4-hydroxylase domain (PHD) family, encoded by *Egln* genes, are the most important regulatory elements of HIFα. In normoxia, these proteins hydroxylate one or two highly conserved proline residues of HIFα, what generates a binding site for the von Hippel-Lindau tumor suppressor protein (VHL), a component of a ubiquitin ligase complex. Consequently, hydroxylated HIFα becomes polyubiquitinated and therefore, targeted for proteasomal degradation. PHD1, PHD2, and PHD3 are the most studied members of PHD families. All of them catalyze O_2-dependent hydroxylation of HIFα by using 2-oxoglutarate as a co-substrate, splitting carbon dioxide (CO_2) and succinate after the enzymatic prolyl-hydroxylation. Hence, they become inactive in hypoxia due to the reduction in O_2 levels. The different PHD members are ubiquitously expressed, although certain tissue-dependent expression and different intracellular localizations are reported (Kaelin, 2005; Metzen et al., 2003). PHD functions are

not fully redundant. As an example, PHD2 constitutes the main HIF1α steady-state low levels controller in normoxia (Berra et al., 2003). Importantly, *Egln1* and *Egln3* genes, respectively encoding for PHD2 and PHD3, are target genes of HIFα, so a negative feedback loop exists between HIFα stabilization and PHD2 and PHD3 induction (del Peso et al., 2003; Ginouves et al., 2008). The second major check-point preventing HIFα transcriptional induction under normoxia is exerted by the factor inhibiting HIF (FIH). This enzyme hydroxylates a specific asparaginyl residue within HIFα that prevents its binding with p300 and CBP transcriptional co-activators. Hence, its hydroxylase activity is also prevented by lack of O_2 in hypoxia (Schofield & Ratcliffe, 2004).

2.2.3. HIF pathway and inflammatory innate immune response

A close bi-directional relationship exists between hypoxia and inflammation. On the one hand, a growing body of evidence demonstrates that hypoxia can trigger inflammation. That is the case of high altitude conditions, which lead to increased inflammatory cytokines load in the bloodstream and can provoke pulmonary and cerebral edema. Moreover, ischemia produced during organ transplantation results in organ inflammation and increases draft rejection. Also, enlarged adipocytes attract macrophages as they lack appropriate O_2 supply. On the other hand, inflamed lesions tend to turn hypoxic often due to an increased metabolic demand and a reduction in metabolites supply due to vasculopathy, as is the case of acute lung injury, intestinal inflammation or pathogen infections (Eltzschig & Carmeliet, 2011). Importantly, hypoxia during inflammation is nowadays considered a remarkable regulator of the immune response, since many immune cells migrate from oxygenated areas to hypoxic inflamed regions to exert their function (Cramer et al., 2003). Indeed, it has even been proposed that HIF1α involvement in immune response constitutes a control system that ensures enhanced inflammatory activities only in hypoxic required locations (Zinkernagel et al., 2007).

Two central transcription factors are intimately related in the cross-talk between hypoxia and inflammation, HIFα and the nuclear factor-kappaB (NF-κB). IKK complex activation signaling involves the expression of anti-apoptotic genes *via*

NF-κB. It is believed that hypoxia can activate IKK complex, with a mechanism involving PHDs and FIH, to exert a pro-survival effect on immune cells under hypoxic conditions (Cummins et al., 2006; Eltzschig & Carmeliet, 2011). At the same time, hypoxia also enhances NF-κB-mediated cytokine production and cell adhesion. HIF1α transcriptional activity also promotes NF-κB amplification by inducing *toll-like receptor* (*Tlr*) *2* and *Tlr6* mRNA, upstream activators of NF-κB signaling (Kuhlicke et al., 2007). Accordingly, NF-κB signaling increases *Hif1a* mRNA levels, both upon non-hypoxic stimulation and in basal conditions, what demonstrates the synergistic cooperation between HIF and NF-κB pathways (Rius et al., 2008; Taylor, 2008; Uden et al., 2008). Some pro-inflammatory factors like the cytokines tumor necrosis factor α (TNFα) or interleukin-1β (IL-1β) can induce HIF1α accumulation through NF-κB-dependent mechanisms in normoxia without altering *Hif1a* mRNA expression levels (Jung et al., 2003; Zhou et al., 2003). Also, reactive O_2 species (ROS) promote HIF1α accumulation by different mechanisms. Thus, considering the intricate molecular relationships between hypoxia and inflammatory response, and taking into account that consequences of inflammatory and hypoxic responses are highly cell-type dependent, further investigations will be needed to fully clarify this cross-talk (Palazon et al., 2014; Taylor, 2008).

Many physiological responses of innate immunity, the first barrier of defense to confront infections, are extremely affected by hypoxia (Harris et al., 2014). The most preponderant cells in innate immunity are neutrophils, monocytes, and macrophages. Neutrophils and monocytes are bone marrow-derived phagocytes that constantly patrol the bloodstream looking for any inflammation, damage or infection clues. In contrast, macrophages are tissue-resident phagocytes of embryonic origin with self-renewal capacity that respond to local tissue stimuli (Guilliams et al., 2014). All these phagocytes migrate to hypoxic foci of inflammation, damage, and infection within tissues following a chemotactic gradient and rapidly adapting to decreasing local O_2 tensions. This adaptation entails a profound metabolic reprogramming towards an anaerobic ATP generation *via* glycolysis mediated by HIF1α (G L Semenza et al., 1994; Zinkernagel et al., 2007). Importantly, not only HIF pathway plays a role in energy production, but also regulates many other aspects of immune response and increasing

evidence suggests that energy metabolism and immune responses are intertwined events (Riboldi et al., 2013).

Our knowledge on the processes regulated by HIF pathway in innate immunity has substantially increased with the implementation of conditional specific myeloid knock-out mice. Importantly, myeloid-specific deletion of *Hif1a* with lysMCre does not alter the number of circulatory neutrophils or monocytes (Cramer et al., 2003). However, other profound alterations are observed in these cells upon HIFα/PHD deficiency or accumulation models.

Remarkable insights have been performed in neutrophils function regarding HIF pathway by using conditional knock-out specific models. Notable data are provided by Walsmley et al., who described that hypoxia has a pro-survival effect mediated by PHD3, involving NF-κB activity and delaying inflammatory resolution (Walmsley et al., 2005, 2011). However, for a comprehensive purpose regarding this thesis, we will focus on innate immune response to hypoxia in macrophages and monocyte-derived macrophages (MDM).

2.2.4. HIF pathway and macrophages

Tissue-resident macrophages and monocytes are attracted by chemotactic agents emerging from inflamed areas like infectious foci, ischemic areas, chronically inflamed regions, wound healings, solid tumors, etc., in which O_2 tension is substantially lower than in the bloodstream and surrounding local areas. Once these cells encounter the hypoxic foci, they stop migration due to hypoxia signaling and acquire different functional phenotypes; indeed, monocytes differentiate into MDM (Strehl et al., 2014). As previously mentioned, one of the most important adaptations is a profound metabolic shift towards a glycolysis-based ATP production, with further consequences for immune response. In fact, a more glycolytic phenotype is associated with a stronger pro-inflammatory macrophage activation while a decreased glycolytic rate correlates with less pro-inflammatory macrophages (Haschemi et al., 2012).

HIF1α deficiency results in decreased motility, aggregation and invasion of infected areas. Moreover, killing capacity of this macrophages after phagocytosis is also reduced (Cramer et al., 2003). Conversely, *Vhl*-conditional deletion in

macrophages and MDM enhances antibactericidal activities by increasing nitric oxide (NO), an antimicrobial compound, and TNF-α production (Peyssonnaux et al., 2005). In this sense, it has been described that HIFα stabilization in MDM and monocytes also occur in solid tumors, highly hypoxic cell aggregates. Tumor cells accumulate HIF1α and as a result, produce macrophage and monocyte chemoattractants like VEGF, endothelins or semaphorins, which promote their migration towards these tumors (Casazza et al., 2013; Grimshaw et al., 2002; Leek et al., 2000; Palazon et al., 2014). Once recruited in the tumor, the hypoxic environment turns them into HI1α-mediated angiogenesis promoters, what has detrimental outcomes like tumor growth (Riboldi et al., 2013).

Different genetic loss-of-function studies have recently revealed that specific PHDs exert non-redundant *in vivo* functions in macrophages (Kiss et al., 2012). PHD3 constitutes an important regulator of the immune response in macrophages, although controversial findings have been proposed regarding this protein in macrophage physiology. In response to abdominal sepsis, PHD3-deficient macrophages differentiate into potent pro-inflammatory cells and elaborate an overwhelming response mediated by HIF1α and NF-κB, with detrimental outcomes (Kiss et al., 2012). However, a different study associated pro-inflammatory macrophage phenotype with PHD3 accumulation in tissues undergoing inflammatory responses and tumors (Escribese et al., 2012). Thus, further studies would be needed to unveil the contribution of PHD3 to macrophage activation in different scenarios and macrophage populations.

2.3. Microglia

2.3.1. Origin and functions

Microglia are the tissue-resident macrophages of the CNS. These cells originate from erythromyeloid progenitors in the yolk sac that migrate and populate the CNS parenchyma prior to its vasculogenesis, where they are maintained by self-renewal under steady-state conditions, autoimmune disorders and degenerative conditions (Ginhoux et al., 2010; Nayak et al., 2014).

They were first described by Rio-Hortega in 1919 as very plastic cells in morphological terms, something that we now know is closely related to their enormous functional versatility (Rio-Hortega, 1919). In basal conditions, they present a relatively small soma with their nucleus surrounded by a narrow cytoplasmic halo that projects a number of fine ramified processes. Microglia in this "surveying" state are permanently monitoring their local environment, contracting and extending their branches, as demonstrated with *in vivo* imaging technologies (Nimmerjahn et al., 2005). These phagocytes take part in a number of processes aimed at conserving CNS homeostasis. Their varied homeostatic functions include neurotrophism, synaptic pruning, neuronal apoptosis during brain development, and cleanup of debris (Nayak et al., 2014).

Transformation of microglial morphology occurs upon detection of homeostasis disturbance. Morphological changes usually include a larger cell body with retracted processes and involve further phenotypic and functional modifications. The alteration of functional microglial status is considered as microglial activation, which occurs in many different conditions like parenchymal injury, infection, neurodegenerative disorders, etc. In these conditions, microglia exhibit a vast array of functional responses to confront any potential insult (**Figure 3**) (Lucin & Wyss-Coray, 2009). Importantly, however, detrimental and beneficial outcomes are attributed to microglial activation in different conditions, what reveals the potential therapeutic targeting of these cells (Nayak et al., 2014; Ransohoff & Perry, 2009). For the objectives postulated in this thesis below, we will focus on microglial responses to AD.

2.3.2. Microglia in AD

As previously described, microglial activation is a prominent feature of AD. Upon amyloid deposition, microglia migrate towards amyloid plaques and surround them, extending projections that interact with amyloid plaques (Itagaki et al., 1989; Serrano-Pozo et al., 2011; Serrano-Pozo et al., 2013). These processes entail deep transcriptional readjustments that are highly influenced by microglia proximity to amyloid plaques and even give rise to particular microglial subtypes (Keren-Shaul et al., 2017).

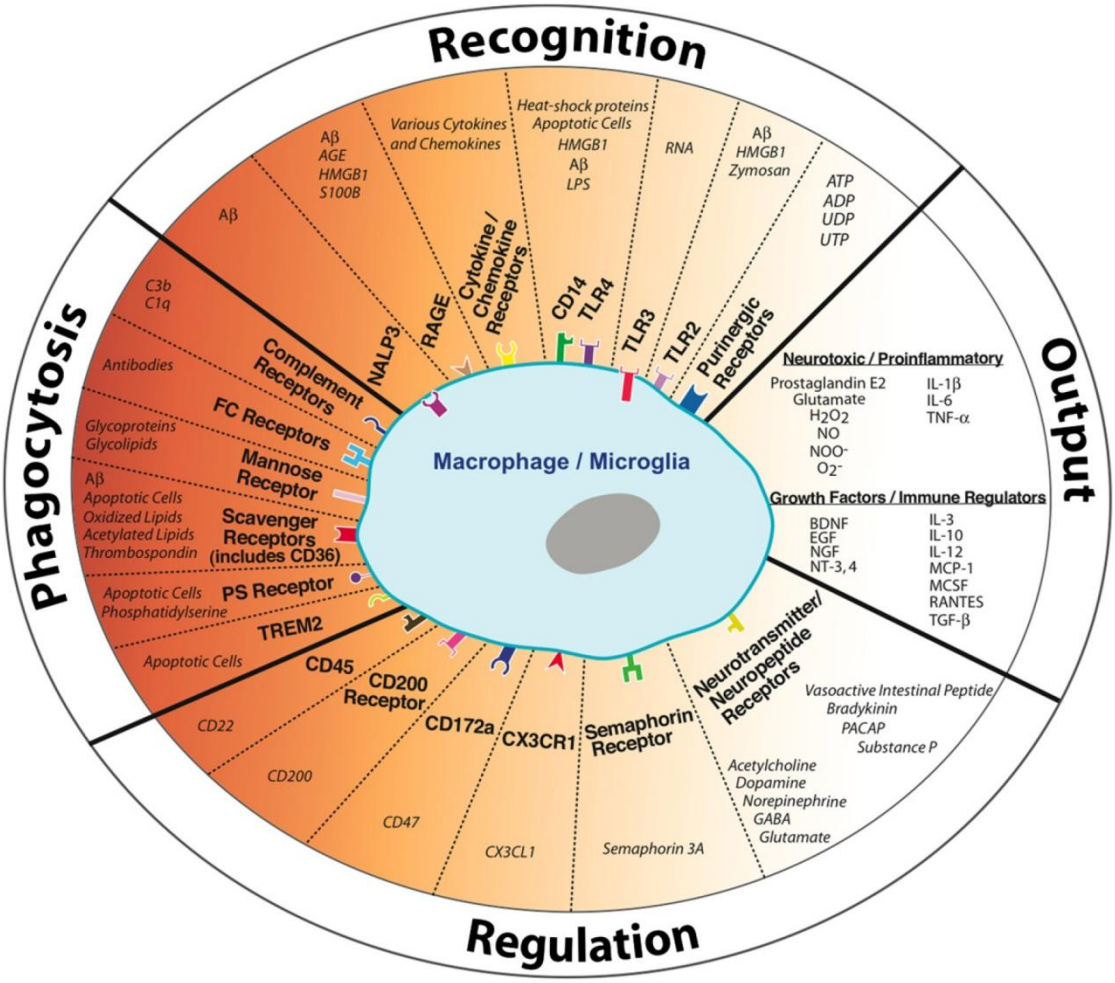

Figure 3. Microglia/Macrophage regulation within the central nervous system (CNS) (Lucin & Wyss-Coray, 2009).

Microglia/macrophages are activated following the stimulation of a number or recognition and phagocytic receptors. The outcome of this activation is regulated by signals also integrated by microglia/macrophages, originated from neurons and other cell types. As a result, different responses are promoted like the release of pro-inflammatory or growth factors. ADP/ATP, adenosine di/triphosphate; AGE, advanced glycation end product; BDNF, brain-derived neurotrophic factor; EGF, epidermal growth factor; GABA, gamma-aminobutyric acid; H_2O_2, hydrogen peroxide; HMGB1, high-mobility group box 1; IL-1β, interleukin 1 β; LPS, lipopolysaccharide; MCP-1, monocyte chemotactic protein-1; MCSF, macrophage colony-stimulating factor; NGF, nerve growth factor; NO, nitric oxide; NOO^-, peroxynitrite; NT-3,4, neurotrophin- 3,4; O_2^-, superoxide; PACAP, pituitary adenylate cyclase-activating peptide; PS, phosphatidylserine; RAGE, receptor for advanced glycation end products; RANTES, regulated upon activation, normal T cell expressed and secreted; TGF-β, transforming growth factor-β; TLR, toll-like receptor; TNFα, tumor necrosis factor-α; TREM2, triggering receptor expressed by myeloid cells-2; UDP/UTP, uridine di/triphosphate.

Analysis of genetic risk factors correlating with sAD has placed microglia in the spotlight of intense research. GWAS with patient samples have revealed that polymorphisms in genes with prominent or exclusive functions in microglia are related to AD. These polymorphisms are implicated in varied functional modules like lipid transport, endolysosomal functioning, and microglial migration and phagocytosis, among others (Pimenova et al., 2018). However, the outcome of these functional modules in AD provokes intense controversy because lots of literature attributes beneficial, inconsequential or even detrimental effects to these modules. It has been described that migration and microglial surrounding activity of amyloid plaques isolates neurons physically from direct contact with the Aβ contained in the plaques, preventing neuronal toxicity (Condello et al., 2015; Yuan et al., 2016). Moreover, microglial uptake of Aβ is involved in Aβ clearance, which associates with a better outcome for AD (Lee & Landreth, 2010). However, exacerbated microglial inflammatory responses can lead to the production of toxic factors harmful to neurons and promote uncontrolled synapse engulfment (Hansen et al., 2018). Therefore, microglia must exert a relevant role in AD and their activation and functional phenotype must be tightly controlled.

2.3.3. Microglia in hypoxia and AD

Given the comorbidity between hypoxia and AD, the importance of microglia response in AD, and the prominent role of hypoxia in the modulation of innate immunity, our laboratory postulated to define the transcriptional changes underlying microglia response to hypoxia. We exposed microglial primary cultures to 1 % or 21 % O_2 for 6 h and analyzed microglial expression profile by microarrays. Then, we defined the Hypoxia-induced Microglia Signature (HMS), containing the up-regulated genes in hypoxia ($p < 0.01$ and logFC >0.5) (**Figure 4, A**). In order to test the relevance of hypoxic microglial response in the microglia from AD mouse models, we performed Gene Set Enrichment Analyses (GSEA) with microarray data publicly available of isolated adult microglia from old *App-Psen1* mice, an AD mouse model, isolated by Fluorescence-Activated Cell Sorting (FACS) (Orre et al., 2014). A prominent overrepresentation of HMS was found in the microglia of this AD mouse model, suggesting a highly hypoxic expression pattern in these microglia (**Figure 4, B**). In order to test *in vivo* HMS dependence on HIF1α,

microglial specific conditional deletion of *Hif1a* gene upon tamoxifen treatment was performed in 12-month-old *Cx3cr1-Cre::ERT2; Hif1a* $^{Flox/Flox}$; *App-Psen1* mice. Transcriptional analysis by reverse transcription real-time polymerase chain reaction (qRT-PCR) confirmed a drastic reduction in the levels of *Hif1a* mRNA and a corresponding reduction in representative HMS-related genes, including a partial but statistically significant reduction of *Egln3* mRNA levels (**Figure 5**) (Unpublished data).

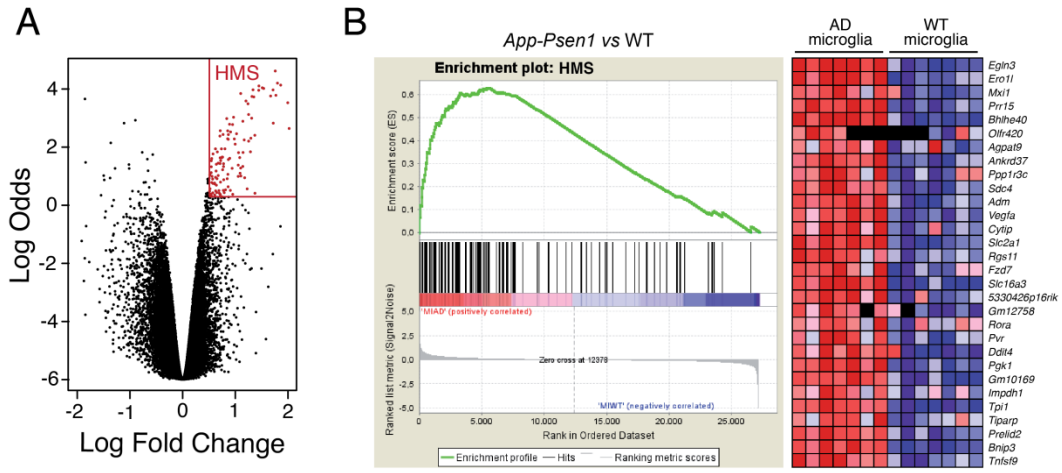

Figure 4. Hypoxia-induced Microglia Signature (HMS) is over-represented in *App-Psen1* mice (unpublished data).

Microglial primary cultures of CD-1 mice were submitted to hypoxia (1 % O_2) or normoxia (21 % O_2) for 6 h and mRNA expression profile was analyzed by microarray. (A) Volcano plot showing Hypoxia-induced Microglia Signature (HMS)-contained genes (p < 0.01, LogFC > 0.5). (B) HMS enrichment in the global gene expression changes observed in adult microglia from 15 to 18-month-old *App-Psen1* (AD) *versus wild-type* (WT) mice (Orre et al., 2014) using Gene Set Enrichment Analysis (GSEA) (left panel). Centre panel shows the heat map of the top 30 ranking leading edge genes included in the HMS. Red symbolizes up-regulation and blue, down-regulation.

Importantly, the most induced gene coincident in both microglia exposed to hypoxia (**Figure 4, B, list of genes**) and the microglia from *App-Psen1* mice is *Egln3* (Orre et al., 2014). This suggests a potentially relevant function for PHD3 in AD microglia.

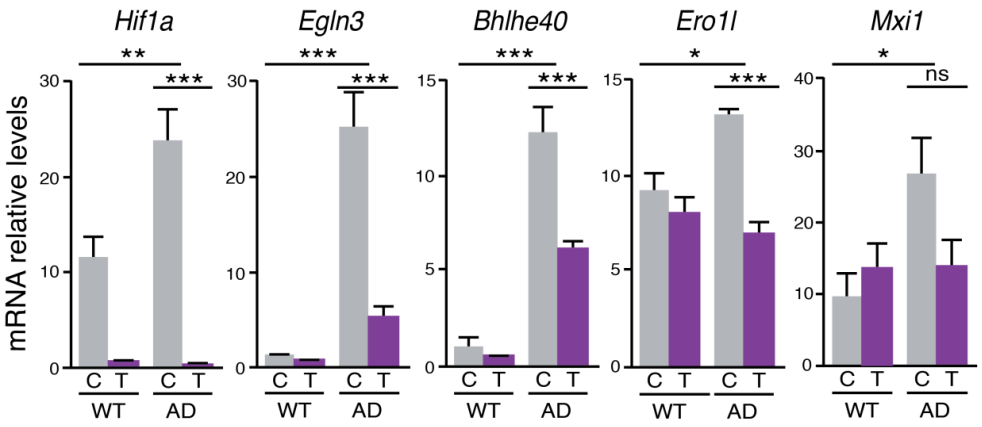

Figure 5. Hypoxia-induced Microglia Signature (HMS) expression *in vivo* is dependent on Hypoxia-inducible factor-1 α (HIF-1α) in *App-Psen1* mice (unpublished data).

Adult microglia were isolated using fluorescence-activated cell sorting (FACS) from 12-month-old *Cx3cr1-Cre::ERT2; Hif1a* $^{Flox/Flox}$; *App-Psen1* mice treated with vehicle (C) or tamoxifen (T; 30 d; magenta) (left panel). *Hif1a* mRNA levels (left) from *wild-type* (WT) *Cx3cr1-Cre::ERT2; Hif1a* $^{Flox/Flox}$; *App-Psen1* mice were quantified by reverse transcription real-time polymerase chain reaction (qRT-PCR) (n = 4 – 5 mice; ** $p < 0.01$; *** $p < 0.001$; Mann Whitney's test). *Egln3*, *Ero1l*, *Mxi1* and *Bhlhe40* mRNA levels were estimated in microglia isolated from 12-month-old *Cx3cr1-Cre::ERT2; Hif1a* $^{Flox/Flox}$; *App-Psen1* mice treated with vehicle (C; grey) or tamoxifen (T; 30 d; magenta) using qRT-PCR. *Hmbs* was used as housekeeping control (n = 4 – 5 mice; * $p < 0.05$; *** $p < 0.001$; Mann Whitney's test for *Egln3* and *Bhlhe40*; Student's *t*-test for *Ero1l* and *Mxi1*).

3. Objectives

1. Investigating the *in vivo* effects of acute and chronic sustained hypoxia on AβPP production and processing and on Aβ degradation.
2. Characterizing the role of PHD3 in AD, with especial focus on microglia responses.

4. Results

In order to facilitate a comprehensive and conceptual organization, the results section is presented according to the objectives.

4.1. Objective 1: Hypoxia on AβPP processing

4.1.1. Validation of hypoxic treatments

As stated in the introduction, previous studies had explained the comorbidity between hypoxia and AD based on hypoxia-mediated up-regulation of AβPP protein levels, Aβ-producing enzymes, and/or down-regulation of Aβ-degrading enzymes, which implies a potentiation of the amyloidogenic processing of AβPP protein. As a result, Aβ accumulation is promoted, giving rise to a neurodegenerative cascade that leads to synaptic dysfunction, formation of NFTs and neuronal death (Hardy et al., 2002; Shankar & Walsh, 2009). These studies had used different strategies including hypoxia and reoxygenation cycles, in vitro models or asphyxiation methods, among others (**Table 1**) (Chen et al., 2003; Guglielmotto et al., 2009; Li et al., 2009; Sun et al., 2006; Zhang et al., 2013). In order to elucidate *in vivo* pure hypoxia-mediated modifications on AβPP protein synthesis, processing or Aβ accumulation, we utilized hermetic chambers where O_2, CO_2, and humidity levels were strictly controlled along the entire exposition. On the other hand, we used acute sustained hypoxia (ASH) and chronic sustained hypoxia (CSH) protocols to allow a more reliably mimicking of some hypoxic conditions epidemiologically linked to AD, like stroke or COPD.

For this purpose, mice were exposed to 9 % O_2 uninterruptedly, through automated control by the hypoxia chamber, for different periods of time. ASH treatment corresponded to incubation of mice for 4 or 16 h (**Figure 6, A**). On the other hand, CSH was achieved by exposing mice to 21 or 30 d to this same O_2 tension (**Figure 6, A**). Our approach induced pure hypoxemia, reducing O_2 saturation and $Pa O_2$, without provoking hypercapnia or acidosis (D'Anglemont de

Tassigny et al., 2015), which are associated to further consequences like increased pulmonary hypertension and edema (Howell et al., 2004).

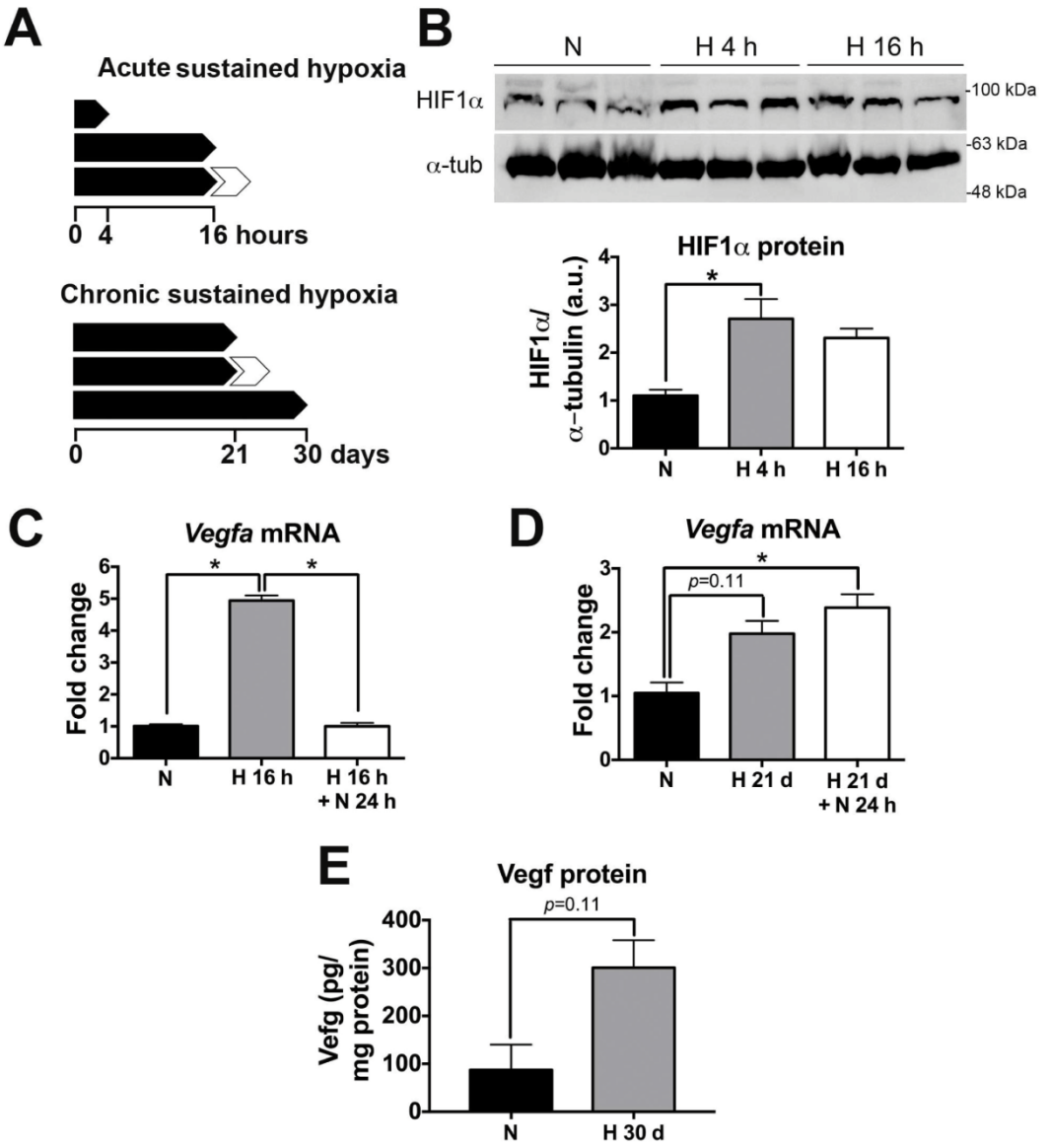

Figure 6. Hypoxia protocols and validation of hypoxic response.

(A) Schematic of acute (up, ASH) and chronic (down, ACH) sustained hypoxia protocols used in this study. White arrowheads represent reoxygenation (21 % oxygen (O_2)) for 24 h. (B) Up, western blot (WB) for hypoxia-inducible factor-1α (HIF1α) in brain extracts from 2–3 month-old *wild-type* mice subjected to normoxia (N) (21 % O_2, 16 h) or ASH (H) (9 % O_2) for either 4 h or 16 h. Down, quantification of HIF1α WB (N, black bar; ASH for 4 h, grey bar; ASH for 16 h, white bar). * $p < 0.05$; Kruskal-Wallis ANOVA with Dunn's multiple comparison test, $n = 3$ per group. (C) Vascular endothelial growth factor (*Vegfa)* mRNA levels measured by reverse transcription real-time polymerase chain reaction (qRT-PCR) in 2–3 month-old *wild-type* mice in N (21 % O_2, black bar) for 16 h, after ASH (H, 9 % O_2, 16 h, grey bar) and ASH followed by N (H+N, reoxygenation, white bar) for 24 h. *18S* mRNA was used as

housekeeping control. * $p < 0.05$; Kruskal-Wallis ANOVA with Dunn's multiple comparison test, $n = 4$ per group. (D) *Vegfa* mRNA levels measured by qRT-PCR in 2–3 month-old *wild-type* mice in N (21 % O_2, black bar) for 21 d, after CSH (H, 9 % O_2, 21 d, grey bar) and CSH followed by N (H+N, reoxygenation, white bar) for 24 h. *18S* mRNA was used as housekeeping control. * $p < 0.05$; Kruskal-Wallis ANOVA with Dunn's multiple comparison test, $n = 4$ per group. (E) VEGF protein levels were measured by ELISA in 2–3 month-old *wild-type* mice subjected to either CSH (H, 9 % O_2, 30 d,) or N (21 % O_2, 30 d) within the same chamber. Mann-Whitney *U* test, $n = 4$ per group. (B-E) Bars ± error bars represent mean ± s.e.m. α-tub, α-tubulin

In order to validate the triggering of hypoxia responses under the ASH protocol, we obtained hemibrain extracts of *wild-type* C57/BI6J mice after ASH treatment and analyzed HIF1α protein levels by western blot (WB) and vascular endothelial growth factor gene (*Vegfa*) induction by qRT-PCR, since it is a well-described HIF1α target gene whose expression is up-regulated by hypoxia (Forsythe et al., 1996; Shima et al., 1995). HIF1α content was significantly increased after 4 h of ASH and a non-significant increment, probably due to negative feedback loop exerted by PHDs (Ginouves et al., 2008), was observed after 16 h, regarding control littermate mice exposed to 21 % O_2 in the same chamber for the same period of time (**Figure 6, B**). ASH treatment for 16 h also induced a 5-fold induction of *Vegfa* mRNA levels that was completely reverted after 24 h of reoxygenation (21 % O_2), in comparison with control littermates exposed to 21 % O_2 (**Figure 6, C**). The effects of CSH were also evaluated using a similar approach in hemibrain extracts from *wild-type* C57/BI6J mice. After 21 d of hypoxia, *Vegfa* mRNA amount showed a trend to increase that became statistically significant due to the slight increment after 24 h in normoxia, highlighting that 24 h of 21 % O_2 is insufficient to recover *Vegfa* mRNA expression levels to basal normoxic conditions (**Figure 6, D**). VEGF protein amount was non-significantly increased after 30 d in hypoxic conditions with respect to normoxic treatment, something that we measured by ELISA (**Figure 6, E**). Altogether, these results indicate that a hypoxic program is activated in *wild-type* mice, elicited by our ASH and CSH protocols.

4.1.2. ASH does not affect the mRNA levels of Aβ-related genes in *wild-type* mice

Aβ accumulation occurs upon imbalance between production and clearance systems (Tarasoff-Conway et al., 2015). AβPP accumulation and subsequent

processing towards a more amyloidogenic pathway or reduced transcription rates of genes encoding for Aβ-degrading enzymes can break this balance, favoring Aβ accumulation. In order to test a possible role of ASH in the regulation of *App* gene, genes involved in α-cleavage (*Adam9*, *Adam10*, and *Adam17/Tace*), β-cleavage (*Bace1*), and ɣ-cleavage (*Psen1, Psen2, Ncstn, Pen2, Aph1a,* and *Aph1b-c*) and genes encoding for Aβ-degrading enzymes (*Bace2, Ide,* and *Mme*) referred to as Aβ-related genes, we exposed *wild-type* C57/BI6J mice to 16 h of maintained hypoxia (9 % O_2) followed or not by reoxygenation (24 h, 21 % O_2) and analyzed the expression of the Aβ-related genes in hemibrain extracts by qRT-PCR regarding normoxia conditions in the same chambers. We used the subsequent renormoxia treatment in order to reveal any changes that could be attributed to reoxygenation rather than to pure hypoxemia *per se*.

App gene transcriptional activity was not altered in this context regarding normoxic conditions either under 16 h of ASH or after 24 h of reoxygenation, ruling out the possibility that an increased transcription of AβPP-encoding gene could eventually lead to an augmented Aβ accumulation (**Figure 7, A**). Then, we analyzed the expression of genes encoding for enzymes with α-secretase activity, which promote a non-amyloidogenic processing of AβPP protein by cleavage within Aβ itself. No differences between ASH and normoxia, before and after reoxygenation, were observed in the expression of *Adam9*, *Adam10* or *Adam17/Tace* genes (**Figure 7, B-D**). On the other hand, many studies provide convincing evidence that place BACE1 protein as the main enzyme mediating β-secretase cleavage, the rate-limiting factor in Aβ production from AβPP protein (Cai et al., 2001; Vassar et al., 1999; Yan et al., 1999). Hence, we measured mRNA levels of *Bace1* gene and found no differences in hypoxia or after reoxygenation regarding normoxia (**Figure 7, E**). As up-regulation of genes encoding for ɣ-secretase complex components has correlated with increased Aβ levels (Li et al., 2009; Liu et al., 2016; Smith et al., 2004), we analyzed the expression of genes encoding for the main components of the ɣ-secretase complex. Except for a significant mild induction of *Psen1* gene registered in reoxygenation after hypoxia *versus* normoxia, our results exhibited the same mRNA levels for *Psen1, Psen2*, *Ncstn*, *Pen2*, *Aph1a*, and *Aph1b-c* genes (**Figure 7, F-K**) in ASH, before and after reoxygenation, and normoxia. Finally, we discarded changes in the transcription of

the genes *Bace2*, *Ide*, and *Mme* in response to our ASH protocol (**Figure 7, L-N**). These results demonstrate that ASH for 16 h is not impacting on the transcription of genes encoding for the Aβ-related proteins, implicated in Aβ accumulation from AβPP processing and degradation.

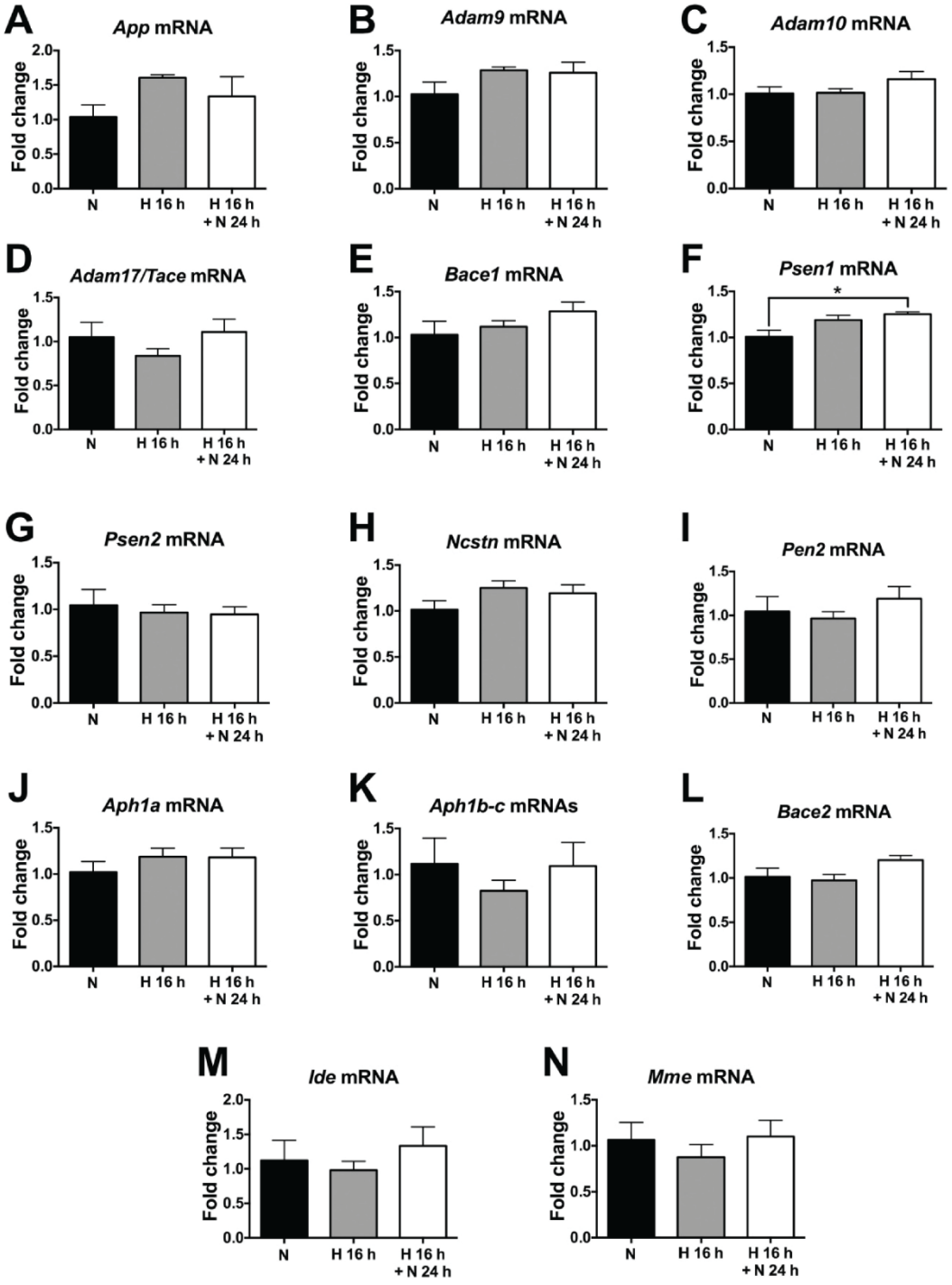

Figure 7. Aβ-related genes mRNA levels are not modified by acute sustained hypoxia (ASH) in *wild-type* mice.

Relative mRNA levels of genes encoding for amyloid-β precursor protein (AβPP) (A), the α-secretases from A disintegrin and metalloprotease (ADAM) family ADAM9 (B),

ADAM10 (C) and ADAM17/TACE (D), β-secretase BACE1 (E), all the components of ɣ-secretase complex presenilin (PS)1 (F), PS2 (G), nicastrin (H), PS enhancer (Pen)2 (I), anterior pharynx defective (APH)1a (J) and APH1b-c (K), and the Aβ-degrading enzymes BACE2 (L), insulin-degrading enzyme (IDE) (M) and neprilysin (N) were estimated by reverse transcription real-time polymerase chain reaction (qRT-PCR) in brains from 2-3 month-old *wild-type* mice subjected to normoxia (N, 21 % oxygen (O_2), black bars) for 16 h or ASH (H, 9 % O_2, 16 h, grey bars), followed or not by N (H+N, reoxygenation, white bars) for 24 h, within the same chamber. *18S* was used as housekeeping control. * $p < 0.05$, Kruskal-Wallis ANOVA with Dunn's multiple comparison test, $n = 4$ per group. (A-N) Bars ± error bars represent mean ± s.e.m.

4.1.3. CSH does not modify the mRNA levels of Aβ-related genes in *wild-type* mice

Given that ASH did not alter the transcriptional response of Aβ-related genes in *wild-type* mice, we tested whether a longer hypoxia exposition could affect the mRNA levels of Aβ-related genes. For this purpose, we used a CSH approach that consisted on submitting *wild-type* C57/BI6J mice to hypoxia (9 % O_2) for 21 d, followed or not by reoxygenation (21 % O_2, 24 h). We also exposed *wild-type* C57/BI6J mice to normoxic conditions (21 % O_2) for the same period of time and within the same hypoxia chambers in order to arrange an appropriate control group. We extracted mRNA content from the mouse brains within the chambers and analyzed mRNA levels of Aβ-related enzymes by qRT-PCR. Very similarly to transcriptional responses exhibited after ASH, non-statistically significant differences in the expression pattern or mRNA stability of any of the analyzed genes were detected, either under hypoxia or after reoxygenation in comparison with normoxia (**Figure 8**), except for *App* gene, whose induction was identified after reoxygenation (**Figure 8, A**). These results show that our previously validated CSH protocol for 21 d is not affecting the transcriptional activity or mRNA stability of genes encoding for the main proteins implicated in Aβ generation and degradation in *wild-type* mice.

Altogether, ASH and CSH results suggest that no transcriptional shift from a preponderant non-amyloidogenic AβPP processing to an elevated amyloidogenic AβPP processing is promoted by hypoxia in *wild-type* mice.

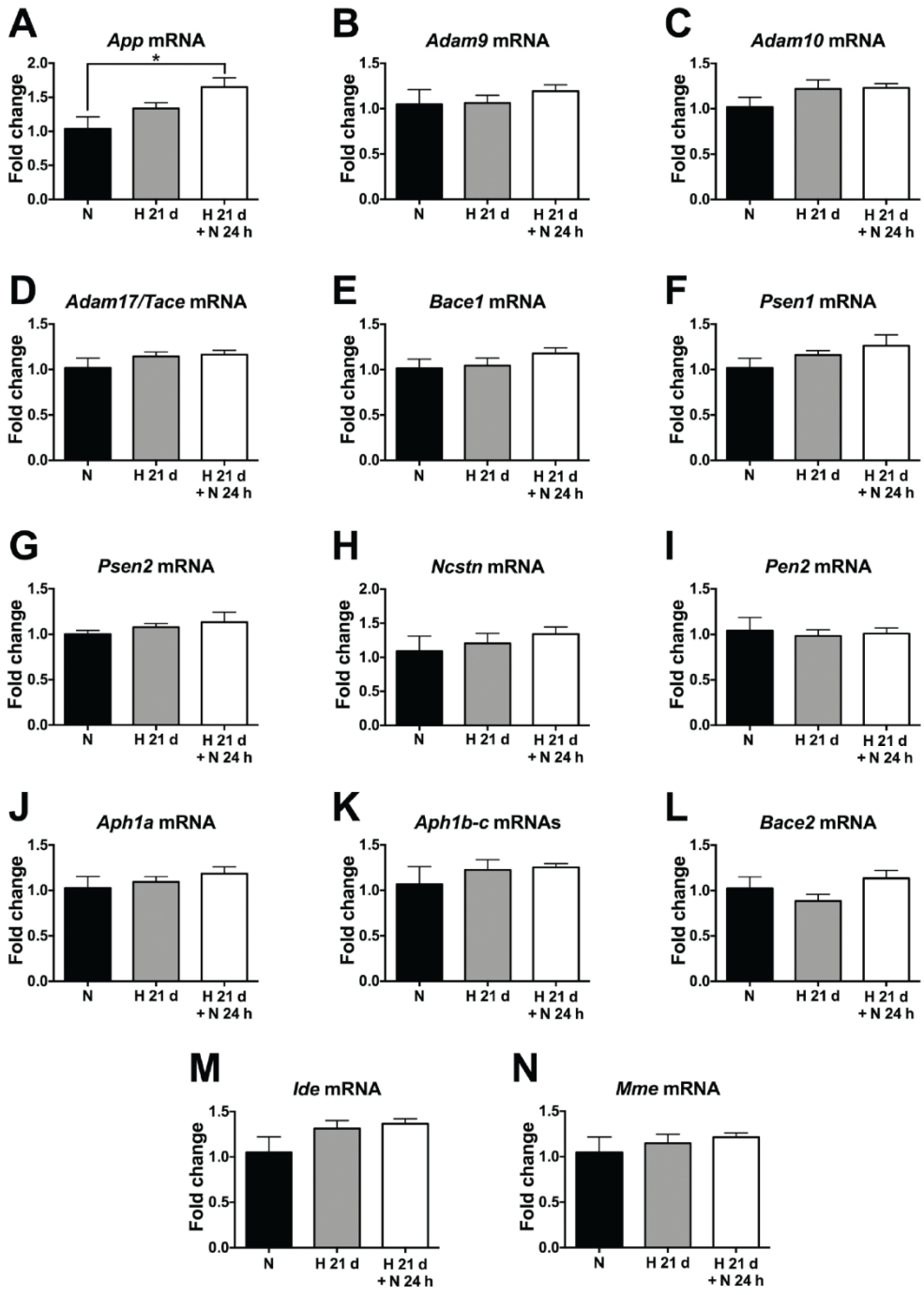

Figure 8. Aβ-related genes mRNA levels are not modified by chronic sustained hypoxia (CSH) in *wild-type* mice.

Relative mRNA levels of genes encoding for amyloid-β precursor protein (AβPP) (A), the α-secretases from a disintegrin and metalloprotease (ADAM) family ADAM9 (B), ADAM10 (C) and ADAM17/TACE (D), β-secretase BACE1 (E), all the components of ɣ-secretase complex presenilin (PS)1 (F), PS2 (G), nicastrin (H), PS enhancer (Pen)2 (I), anterior pharynx defective (APH)1a (J) and APH1b-c (K), and the Aβ-degrading enzymes BACE2 (L), insulin-degrading enzyme (IDE) (M) and neprilysin (N) were estimated by reverse transcription real-time polymerase chain reaction (qRT-PCR) in brains from 2-3 month-old *wild-type* mice subjected to normoxia (N, 21 % oxygen (O_2), black bars) for 21 d or CSH (H, 9 % O_2, 21 d, grey bars), followed or not by N

(H+N, reoxygenation, white bars) for 24 h, within the same chamber. *18S* was used as housekeeping control. * $p < 0.05$, Kruskal-Wallis ANOVA with Dunn's multiple comparison test, $n = 4$ for normoxia group and $n = 5$ for the two hypoxia groups. (A-N) Bars ± error bars represent mean ± s.e.m.

4.1.4. AβPP processing is not changed by either ASH or CSH

Although we did not observe any alteration in the mRNA levels of Aβ-related genes, it was still possible that ASH or CSH could affect protein levels of AβPP processing by-products and relevant enzymes. We analyzed the amount of the rate-limiting enzyme in Aβ generation BACE1 and AβPP protein levels in hemibrain extracts of *wild-type* C57/BI6J mice exposed to ASH (for 4 h or 16 h) or CSH (for 30 days). BACE1 protein had been described to increase in response to acute insults like ischemia and energy deprivation (O'Connor et al., 2008; Tesco et al., 2007), something also reported by several *in vivo* and *in vitro* studies (Guglielmotto et al., 2009; Liu et al., 2016; Moussavi et al., 2012; Sun et al., 2006; Zhang et al., 2007). BACE1 amount remained unchanged after 4 h or 30 d of hypoxia (9 % O_2) *versus* normoxia (21 % O_2) by Western blot (WB) (**Figure 9, A**). However, unlike previous studies, it not only did not accumulate but significantly decreased after 16 h hypoxic treatment (**Figure 9, A**). On the other hand, AβPP protein levels measured by WB were not modified after 4 h, 16 h or 30 d of hypoxic treatment (**Figure 9, B**).

Although these results do not suggest a pro-amyloidogenic function either for ASH or CSH, we tried to measure Aβ peptides by ELISA in order to discard other potential factors that could be contributing to its accumulation. Unfortunately, Aβ peptides levels in *wild-type* mice were under the minimum threshold for detection with ELISA, so we decided to analyze the ratio between C99 and C83 by WB since an increased ratio indicates a pro-amyloidogenic AβPP processing. In the comparison of ASH or CSH with normoxia, no differences were exhibited in C99/C83 ratio (**Figure 9, C**). As a control, we estimated the C99/C83 ratio in *App-Psen1* mice (**Figure 9, C**). These data strongly support an inconsequential effect of ASH or CSH in Aβ accumulation regarding AβPP production, processing, and degradation in *wild-type* mice.

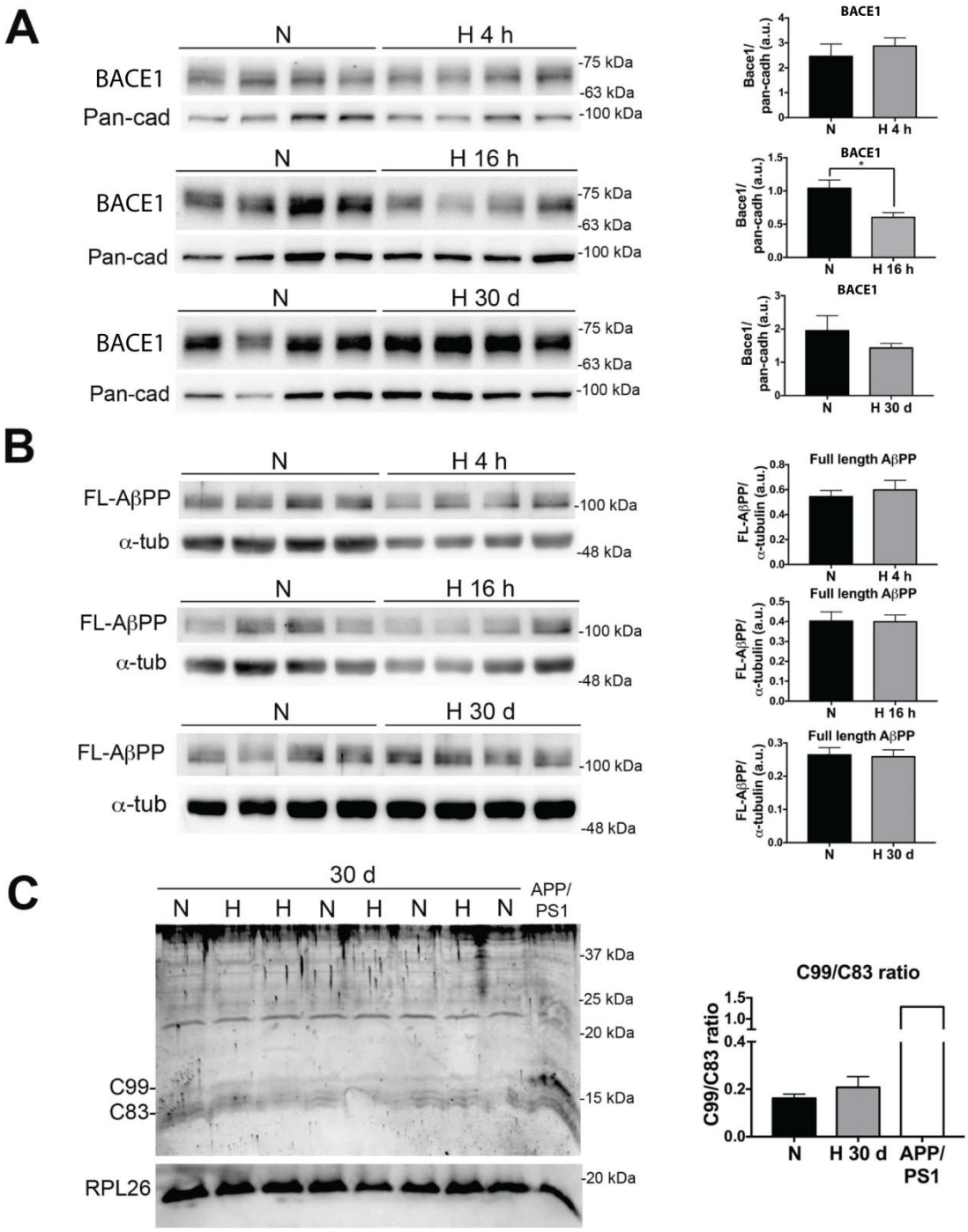

Figure 9. Neither acute sustained hypoxia (ASH) nor chronic sustained hypoxia (CSH) alter amyloid-β precursor protein (AβPP) processing.

(A) BACE1 protein levels were measured by western blot (WB) in the brains of 2–3 month-old *wild-type* mice subjected to ASH (H 4 h or 16 h, 9 % oxygen (O_2)), CSH (H 30 d, 9 % O_2), or normoxia (N 4 h, 16 h or 30 d, 21 % O_2) for the corresponding period of time within the same chamber. Right bar graphs depict the quantification of WBs using pan-cadherin (Pan-cad) as loading control (normoxia, N, black bars; hypoxia, H, grey bars). * $p < 0.05$, Mann-Whitney *U* test, $n = 4$ per group. (B) Levels of full-length AβPP (FL-AβPP) were measured by WB in the brains of 2–3 month-old

wild-type mice subjected to ASH (H 4 h or 16 h, 9 % O_2), CSH (H 30 d, 9 % O_2), or normoxia (N 4h, 16 h or 30 d, 21 % O_2) for the corresponding period of time within the same chamber. Right bar graphs depict the quantification of WBs using α-tubulin (α-tub) as loading control (normoxia, N, black bars; hypoxia, H, grey bars). * $p < 0.05$, Mann-Whitney *U* test, $n = 4$ per group. (C) The α C-terminal fragment (C99) and β C-terminal fragment (C83) fragments of AβPP were measured by WB and the C99/C83 ratio was calculated in the brains of 2–3 month-old *wild-type* mice subjected to CSH (H 30 d, 9 % O_2), or normoxia (N 4h, 16 h or 30 d, 21 % O_2) for the corresponding period of time within the same chamber. The rightmost lane of the Tris-tricine gel was loaded with a protein extract from an *App-Psen1* (APP/PS1) transgenic mouse as positive control. The membrane was reprobed with an anti-Ribosomal Protein L26 (RPL26) antibody to demonstrate equal protein load in all gel lanes. Right bar graphs depict the quantification of WBs using α-tubulin (α-tub) as loading control (normoxia, N, black bars; hypoxia, H, grey bars). * $p < 0.05$, Mann-Whitney *U* test, $n = 4$ per group. (A-C) Bars ± error bars represent mean ± s.e.m.

4.1.5. Aβ accumulation, AβPP production, and soluble AβPPα amount are not affected by CSH in *App/Psen1* mice

We have previously presented evidence on that neither ASH nor CSH impact on both transcription and protein levels of Aβ-related genes and rate-limiting enzymes, as well as on the amount of AβPP processing by-products. However, it is unknown if CSH could modify Aβ content by altering AβPP synthesis or processing in the presence of amyloid plaques, potentially resembling the AD situation. To conduct this study, we submitted *App-Psen1* mice, AD mouse models that exhibit a prominent Aβ accumulation, of 8 months old, representing a low Aβ burden situation, and 14 months old, as a high Aβ burden paradigm, to hypoxia (9 % O_2) and normoxia (21 % O_2) in the same chambers for 21 days.

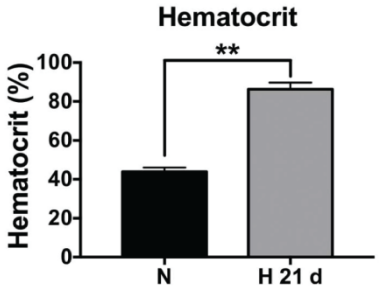

Figure 10. Chronic sustained hypoxia (CSH) increases hematocrit in *App-Psen1* mice.
Hematocrit of 14-month-old *App-Psen1* mice subjected to CSH (H, 21 days, 9 % O_2, black bar) or normoxia (N, 21 days, 21 % O_2, grey bar), within the same chamber was measured. ** $p < 0.01$; Mann-Whitney *U* test, $n = 4$ per group. Bars ± error bars represent mean ± s.e.m.

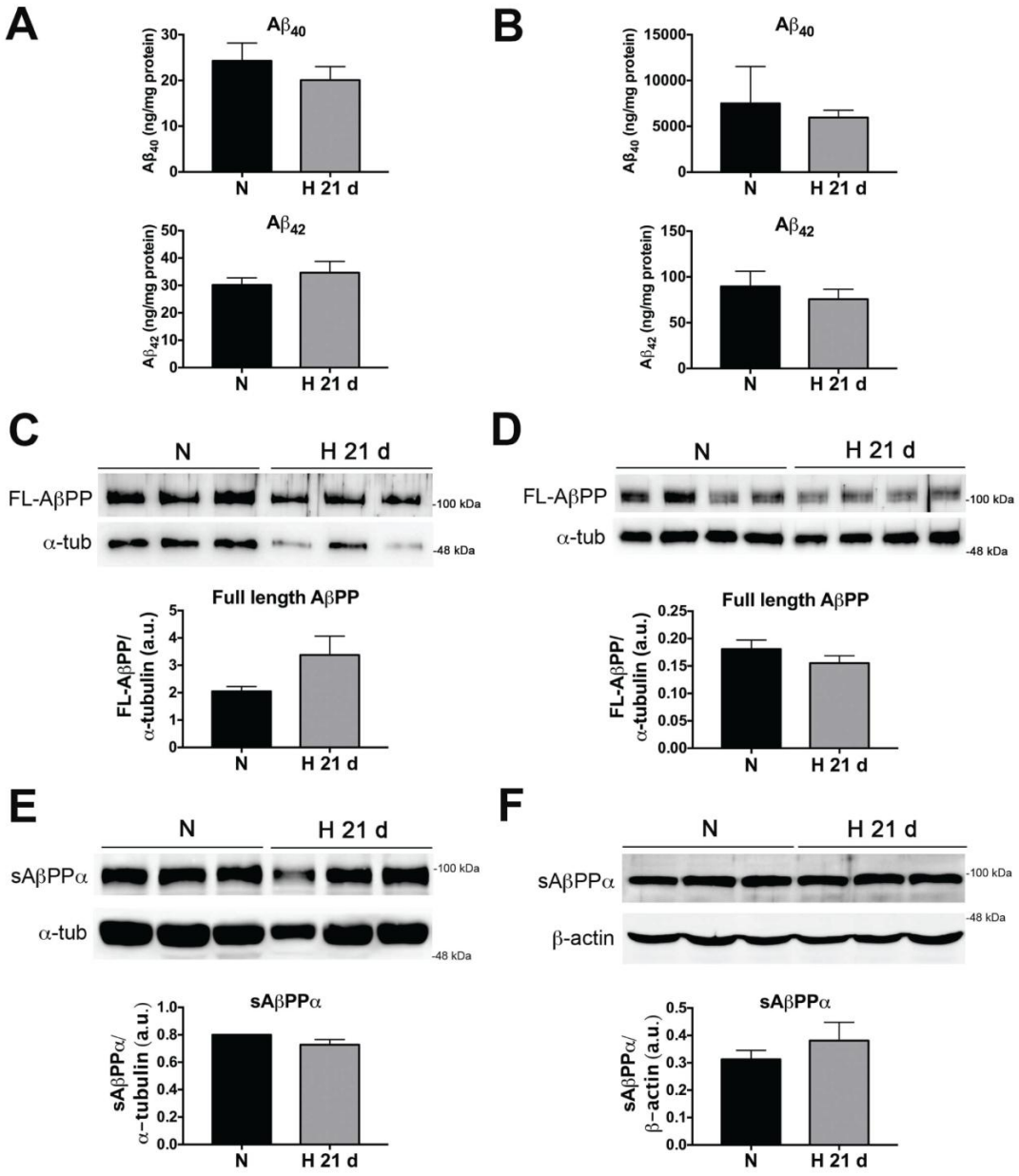

Figure 11. Chronic sustained hypoxia (CSH) does not modify the levels of amyloid-β (Aβ)$_{1\text{-}40}$, Aβ$_{1\text{-}42}$, full-length amyloid-β precursor protein (FL-AβPP) or soluble AβPP α (sAβPPα).

(A-B) Aβ$_{1\text{-}40}$ (up) and Aβ$_{1\text{-}42}$ (down) levels were measured by ELISA in 8-month-old (A) and 14-month-old (B) *App-Psen1* mice exposed to normoxia (N, 21 d, 21 % oxygen (O_2), black bars) or CSH (H, 21 d, 9 % O_2, grey bars), within the same chamber. * $p < 0.05$; Mann-Whitney *U* test, $n = 3\text{-}4$ per group. (C-D) FL-AβPP protein levels were measured by western blot (WB, up) in the brains of 8-month-old (C) and 14-month-old (D) *App-Psen1* mice exposed to normoxia (N, 21 d, 21 % O_2) or CSH (H, 21 d, 9 % O_2), within the same chamber. Bar graphs (down) depict the quantification of WBs using α-tubulin (α-tub) as loading control (normoxia, N, black bars; hypoxia, H, grey bars). * $p < 0.05$; Mann-Whitney *U* test, $n = 3$ per group. (E-F) sAβPPα protein levels were measured by WB (up) in the brains of 8-month-old (E)

and 14-month-old (F) *App-Psen1* mice exposed to normoxia (N, 21 d, 21 % O_2) or CSH (H, 21 d, 9 % O_2), within the same chamber. Bar graphs (down) depict the quantification of WBs using α-tub (E) or β-actin (F) as loading controls (normoxia, N, black bars; hypoxia, H, grey bars). * $p < 0.05$; Mann-Whitney *U* test, $n = 3$ per group. (A-F) Bars ± error bars represent mean ± s.e.m.

Since hematocrit has been described to increase under hypoxic conditions as a physiological response to maintain the O_2 levels in the blood (Schuster et al., 1989; Semenza et al., 1991), we measured the hematocrit in the animals used in order to confirm a hypoxic response. Average hematocrit levels for *wild-type* mice in normobaric normoxia range from 42.0±1.2 % (D'Anglemont de Tassigny et al., 2015; Schreier et al., 2014) to about 75 % at 9 % O_2 (data not shown). We found very similar hematocrit values, both in normoxia and after CSH, in *App-Psen1* mice to previously described *wild-type* values, confirming a hypoxic response triggered by CSH in *App-Psen1* mice (**Figure 10**).

ELISA quantification of cortical $A\beta_{1-40}$ and $A\beta_{1-42}$ levels showed similar amounts of these Aβ peptides in CSH regarding normoxia, both in 8-month-old and 14-month-old *App-Psen1* mice (**Figure 11, A-B**). Accordingly, we did not obtain significant changes in AβPP protein levels in CSH *versus* normoxia at any of the ages, analyzed by WB (**Figure 11, C-D**). Moreover, sAβPPα levels also remained stable after CSH treatment in both young and aged *App-Psen1* mice (**Figure 11, E-F**), suggesting the inexistence of any shift in AβPP processing.

4.2. Objective 2: PHD3 and AD microglia

4.2.1. *Egln3* mRNA is expressed in microglia surrounding plaques

Egln3 mRNA levels were quantified in many different cell populations by single-cell RNA sequencing in the mouse somatosensory cortex and CA-1 hippocampal areas. This approach revealed modest *Egln3* mRNA levels in some interneuronal populations and virtually absent *Egln3* expression in microglia (Zeisel et al., 2015). However, *Egln3* expression is strongly increased in FACS-isolated microglia from AD mouse models, according to microarray data (Orre et al., 2014). We performed i*n situ* hybridization experiments to confirm *Egln3* expression in microglia from

App-Psen1 mice cortical areas and to explore the distribution of *Egln3*-overexpressing microglia. We found non-microglial cells expressing *Egln3* mRNA that could correspond to interneuronal cells, as previously described (Zeisel et al., 2015). Remarkably, *Egln3*-expressing microglia was almost exclusively restricted to amyloid plaques vicinity (**Figure 12**), suggesting no potential effects for *Elgn3* ablation in microglia far from amyloid plaques, since they did not virtually express *Elgn3*.

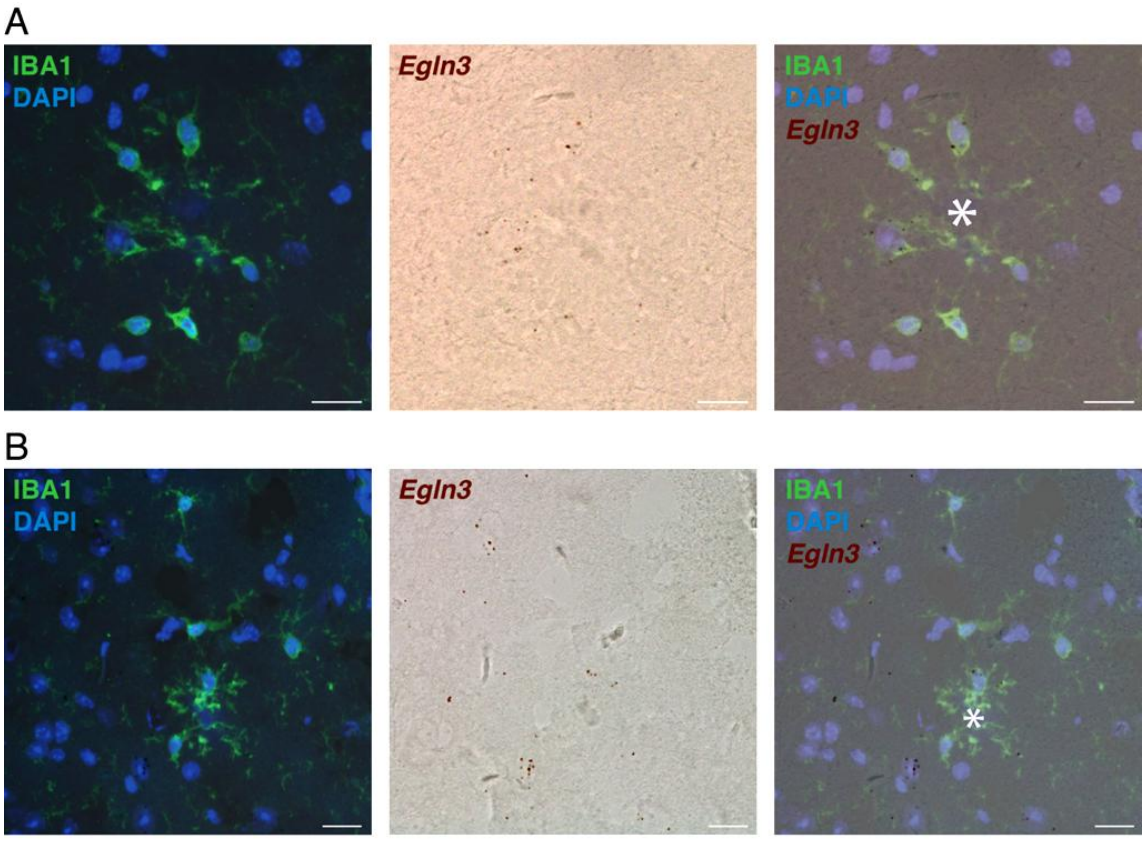

Figure 12. *Egln3* mRNA expression in microglia is restricted to amyloid plaques periphery

(A-B) Representative cortical coronal sections from 8 month-old *App-Psen1* mice after *in situ* hybridization with *Egln3* (brown) probe, immunostaining with anti-IBA1 (green) antibody and staining with DAPI (blue). Left panel shows fluorescent IBA1 and DAPI markers, central panel shows bright field *Egln3* probe, and right panel shows colocalization of left and central panels. Asterisks indicate the position of amyloid plaques in the right panels. Scale bars are 20 µm. (A) High magnification image of microglia surrounding an amyloid plaque. (B) Low magnification image of microglia surrounding and far from amyloid plaque.

These results suggest that *Egln3* mRNA expression in microglia is specifically induced in amyloid plaques vicinity.

4.2.2. PHD3 does not regulate Aβ-induced microglial proliferation but limits CD45 protein levels

As described in the introduction, microglia are highly versatile cells that can adopt many different phenotypes in response to environmental cues (Hanisch & Kettenmann, 2007). In AD, microglia acquire an activated state that induces a series of dynamic changes, including an increased proliferation, morphological variations, and modification of the cell surface phenotype (Itagaki et al., 1989; Kamphuis et al., 2012; Olmos-Alonso et al., 2016; Serrano-Pozo et al., 2011; Streit et al., 2014). Importantly, *Egln3* knock-out mice develop with minor sympatho-adrenal alterations (Bishop et al., 2008). In this sense, we did not observe any apparent morphological or behavioral alterations or significant differences in mice weight throughout the entire study.

As a first approach to explore a possible role of PHD3 in AD microglia, we measured the proportion of CD11b/CD45 microglia by flow cytometry (Orre, et al., 2014) in three experimental groups of mice: control, including *wild-type* and *Egln3* $^{-/-}$ *m*ice, since there were no differences in any of the evaluated parameters by flow cytometry, *App-Psen1* and *Egln3* $^{-/-}$*; App-Psen1* mice. We selected the microglial population based on the gating strategy included in material and methods section. CD11b/CD45 positive microglial population is contained in the depicted gates (**Figure 13, A-C**).

The proportion of microglia was significantly higher in Aβ-accumulating mice regarding the control group. However, it was very similar between *App-Psen1* and *Egln3* $^{-/-}$*; App-Psen1* mice (**Figure 13, D**). To confirm whether microglia number was conserved between *App-Psen1* and *Egln3* $^{-/-}$*; App-Psen1* mice, we used stereological methods to count microglia cells in cortical sections per area stained with anti-ionized calcium-binding adapter molecule 1 (IBA1) antibody, an extensively used microglial marker, colocalizing with the DNA dye DAPI to unequivocally visualize individual cells. We did not observe differences in microglia density between these two genotypes (**Figure 14**), corroborating the result obtained by flow cytometry. This result suggests that *Egln3* deletion is not altering microglia proliferation capacity in AD.

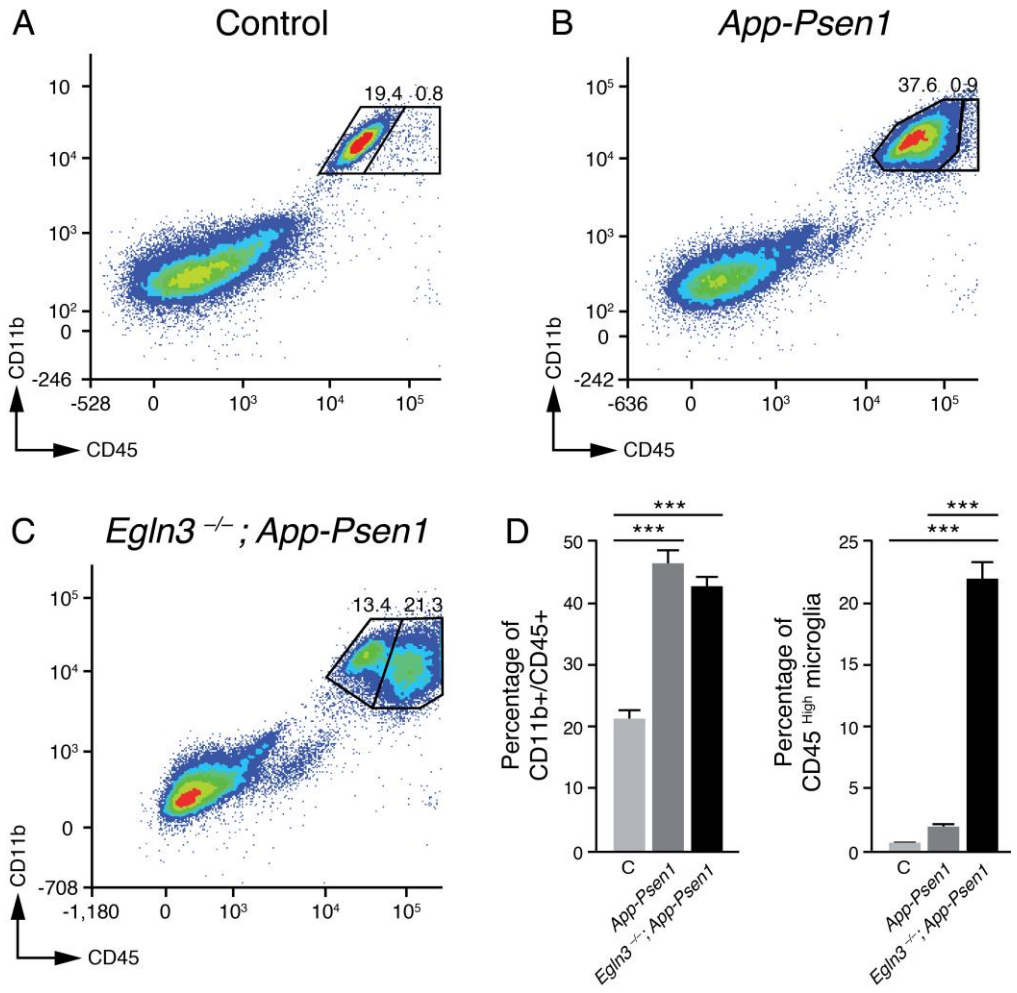

Figure 13. Microglia proliferation is not affected by prolyl-hydroxylase 3 (PHD3) absence, but their CD45 protein levels are increased.

(A-C) Flow cytometry density plots showing e*x vivo*-isolated adult microglia from 12-month-old control (*wild-type* and *Egln3* $^{-/-}$ mice) (A), *App-Psen1* (B) and *Egln3* $^{-/-}$; *App-Psen1* (C) mice. Microglia are included in the depicted gates and are characterized by surface expression of CD45 and CD11b. Representative percentages of the incipient or evident microglial subpopulations according to CD45 protein levels are shown. (D) Quantification of total microglial (left) or CD45^{high} microglial subpopulation (right) proportion from all single isolated cells registered in density plots A-C. Control (C), light grey bars; *App-Psen1*, dark grey bars, and *Egln3* $^{-/-}$; *App-Psen1,* black bars. *** $p < 0.001$, ANOVA with Tukey's post-test, $n = 9$ for control group and $n = 5$ for the rest of the groups. Bars ± error bars represent mean ± s.e.m.

Interestingly, although no differences were shown in microglial proportion, enriched levels of CD45 surface marker were detected in *Egln3* $^{-/-}$*; App-Psen1* in

comparison with *App-Psen1* microglia, giving rise to a second identifiable microglial population (**Figure 13, D**).

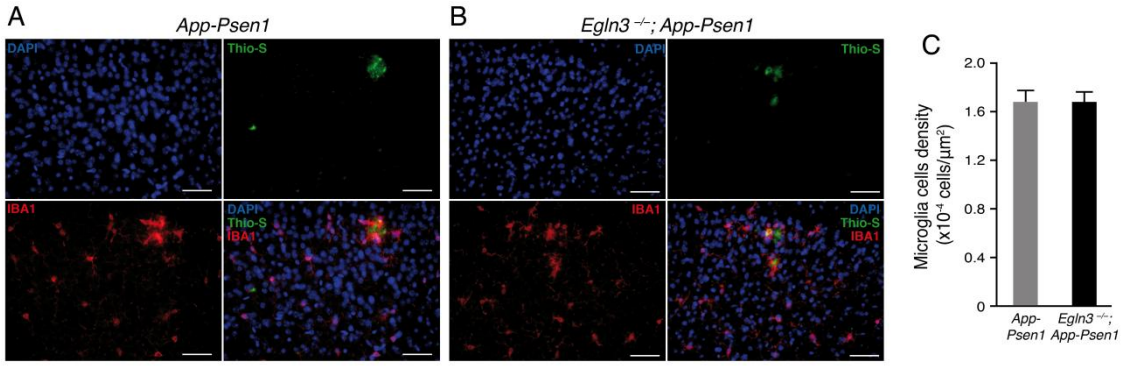

Figure 14. Stereological cell counting confirms unmodified microglia numbers in Alzheimer's disease (AD) upon prolyl-hydroxylase 3 (PHD3) ablation.

(A-B) Representative cortical coronal sections from 6 month-old *App-Psen1* (A) and *Egln3* $^{-/-}$; *App-Psen1* (B) mice immunostained with the microglial marker anti-IBA1 (red) antibody and stained with the amyloid plaques dye Thioflavine-S (Thio-S, green). DAPI (blue) was used to label nuclei. Scale bars, 50 µm. (C) Number of microglia cells per µm^2 of cortical area number of *App-Psen1* (grey bar) and *Egln3* $^{-/-}$; *App-Psen1* (black bar) mice (n = 18 hemicortices from 6 *App-Psen1*, n = 12 hemicortices from 4 *Egln3* $^{-/-}$; *App-Psen1* mice; * $p < 0.05$; Mann Whitney's test). Bars ± error bars represent mean ± s.e.m.

These results demonstrate that PHD3 is not involved in microglial proliferation in AD mouse models but its absence results in a phenotypic modification evidenced by increased surface expression of the CD45 protein.

4.2.3. PHD3 restricts Aβ phagocytosis and its absence reduces total Aβ content

CD45 is a tyrosine phosphatase found in lymphoid and myeloid cells whose overexpression in microglia is associated with activated states (Charbonneau et al., 1988; Crotti & Ransohoff, 2016). Some reports have attributed enhanced phagocytic capacity to microglia expressing elevated levels of CD45 protein (Rangaraju et al., 2018; Zhu et al., 2011). Given that isolated microglia cells from *Egln3*$^{-/-}$*; App-Psen1* mice exhibited increased CD45 expression levels, we tested whether the phagocytic capability of *Egln3*$^{-/-}$*; App-Psen1* microglia was altered *in vivo*. To address this question, we based on a previously described protocol (Heneka et al., 2013). In brief, we injected mice with methoxy-XO4, a fluorescent

compound with high-affinity binding to Aβ that is incorporated in microglia upon stained Aβ uptake. Three hours after the injection, we quantified the proportion of microglia incorporating methoxy-XO4 by flow cytometry and found a trend to augment in the case of *Egln3*$^{-/-}$*; App-Psen1* microglia (**Figure 15**).

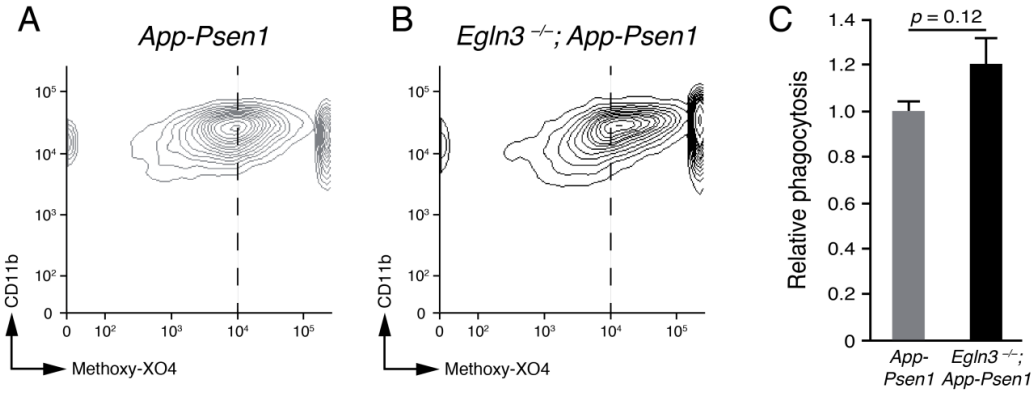

Figure 15. A modest increase in amyloid-β (Aβ) phagocytosis is elicited by prolyl-hydroxylase 3 (PHD3) deficiency in microglia.

(A-B) Flow cytometry contour plots showing Aβ phagocytosis by microglia isolated from adult 12-month-old *App-Psen1* (A) and *Egln3* $^{-/-}$; *App-Psen1* (B) mice 3 h after intraperitoneal injection of methoxy-XO4. (C) Relative measurements regarding *App-Psen1* phagocytosis (*App-Psen1,* grey bar; *Egln3* $^{-/-}$; *App-Psen1,* black bar). * $p < 0.05$; Student's *t*-test; $n = 3$ mice. Bars ± error bars represent mean ± s.e.m.

Aβ peptides can be removed from the brain by various overlapping and interacting clearance systems including cellular uptake and enzymatic degradation, transport across the blood–brain and blood–cerebrospinal fluid barriers, interstitial fluid bulk flow, and cerebrospinal fluid absorption into the circulatory and lymphatic systems (Tarasoff-Conway et al., 2015). In particular, increased phagocytosis of Aβ has been linked to reductions in overall brain Aβ content (Chung et al., 1999; Colton, 2009; Combs, 2009; Condello et al., 2017). We postulated that the aforementioned trend to increase the phagocytic capacity of microglia from *Egln3*$^{-/-}$*; App-Psen1* could imply a reduction in cortical Aβ content. To tackle this question, we obtained cortical homogenates from *App-Psen1* and *Egln3* $^{-/-}$*; App-Psen1* mice in guanidine-containing buffer in order to extract total Aβ content from our samples and performed ELISA for human $Aβ_{1-40}$ and $Aβ_{1-42}$ peptides, the two main toxic Aβ species (Burdick et al., 1992), in collaboration with Dr. Navarro, from Dr. Vitorica's laboratory. Our results showed a trend to reduce total $Aβ_{1-40}$ content coupled by a significant decrease in the levels of $Aβ_{1-42}$ (**Figure 16, A**).

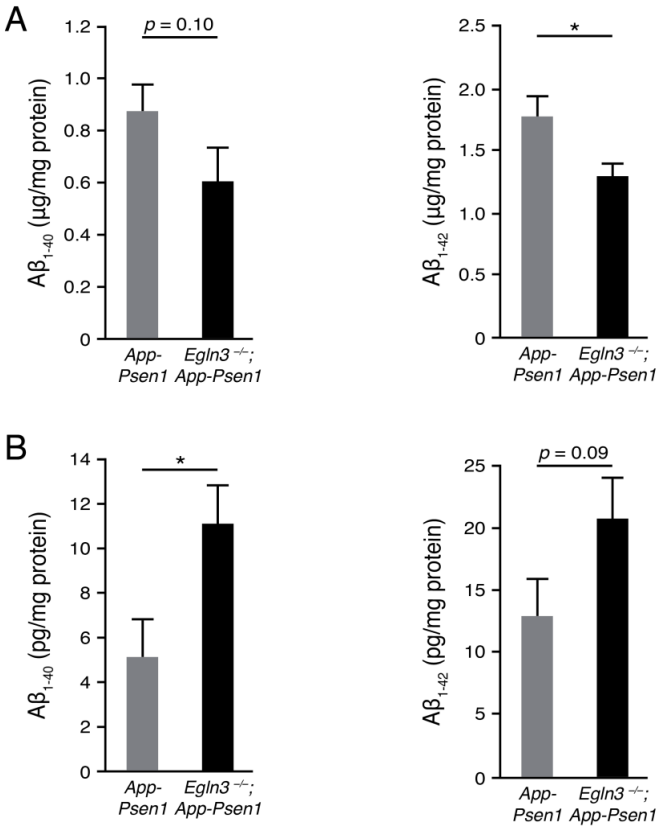

Figure 16. Lack of prolyl-hydroxylase 3 (PHD3) produces a reduction in total amyloid-β (Aβ) peptide levels but an increase in soluble Aβ peptides fraction.

(A-B) $A\beta_{1\text{-}40}$ and $A\beta_{1\text{-}42}$ measurement by ELISA of hemicortical extracts from 6-month-old *App-Psen1* (grey bars) and *Egln3* $^{-/-}$; *App-Psen1* (black bars) mice. (A) Total $A\beta_{1\text{-}40}$ and $A\beta_{1\text{-}42}$ content. * $p < 0.05$; Student's *t*-test; $n = 5$ *App-Psen1* mice and $n = 4$ *Egln3* $^{-/-}$; *App-Psen1* mice. (B) Soluble $A\beta_{1\text{-}40}$ and $A\beta_{1\text{-}42}$ content. * $p < 0.05$; Student's *t*-test; $n = 4$ mice per group. Bars ± error bars represent mean ± s.e.m.

A growing body of evidence points to greater neurotoxic effects of soluble conformations of Aβ peptides (Haass & Selkoe, 2007; Walsh & Selkoe, 2007) so we wondered if soluble Aβ content in *Egln3*$^{-/-}$*; App-Psen1* mice was modified. To address this question, we used the previously described ELISA essay, but employing isolated soluble fractions from cortical extracts. Although they account for a very short proportion of total Aβ content, we obtained a significant increase of $A\beta_{1\text{-}40}$ amount concomitantly with a trend to increase $A\beta_{1\text{-}42}$ in *Egln3*$^{-/-}$*; App-Psen1* regarding *App-Psen1* mice (**Figure 16, B**).

Thus, PHD3 deficiency promotes a modest increase in microglial Aβ phagocytosis, correlating with diminished total $A\beta_{1\text{-}42}$ content but increased soluble $A\beta_{1\text{-}40}$ fraction.

4.2.4. PHD3 deficiency induces changes in Aβ deposition

The different Aβ isoforms exhibit diverse solubility and aggregation properties (Chung et al., 1999). We wondered whether the detected decrease in total $A\beta_{1-40}$ and $A\beta_{1-42}$ correlated with changes in the area occupied by Aβ plaques, in their numbers or in their structure. To this aim, we stained cortical sections with an anti-Aβ antibody and Thio-S, which stains β-sheet amyloid structures (**Figure 17**), and analyzed the percentage of the cortex covered by dense-core amyloid plaques. Non-significant differences were observed in this parameter in *Egln3*$^{-/-}$*; App-Psen1 versus App-Psen1* mice with none of the employed markers, although we observed a trend to an increment (**Figure 18, A**). Next, we extended our examination to other parameters like density of amyloid plaques, in terms of number of plaques per area, and average size of plaques, both in the case of Thio-S stained sections. Our results showed a significantly raised density of amyloid plaques in *Egln3*$^{-/-}$*; App-Psen1* (**Figure 18, B**) that was coincident with a significantly lower average size of Aβ plaques (**Figure 18, C**). Closer evaluation of plaques size revealed that this reduced average size was due to a bigger amount of relatively small plaques (less than 194 μm^2) in *Egln3*$^{-/-}$*; App-Psen1* mice, without altering the number of bigger plaques (**Figure 18, D**).

Yuan et al. described in 2016 that amyloid plaques can appear in several compaction degrees. Filamentous plaques emerge from β-sheet folding of diffuse plaques and they can acquire a compact conformation upon compaction potentially mediated by microglia, given the close interaction between fibrillar Aβ (fAβ) structures and microglial processes (Yuan et al., 2016). In order to ascertain which kind of amyloid plaques deposition was responsible for the increased number of amyloid plaques in *Egln3* $^{-/-}$*; App-Psen1*, we quantified with stereological methodologies the amount of filamentous and compact amyloid plaques per cortical area unit upon Thio-S staining. We obtained a remarkable increase in the number of compact plaques per cortical area in *Egln3*$^{-/-}$*; App-Psen1* with respect to *App-Psen1* mice and no differences in filamentous ones (**Figure 18, E**).

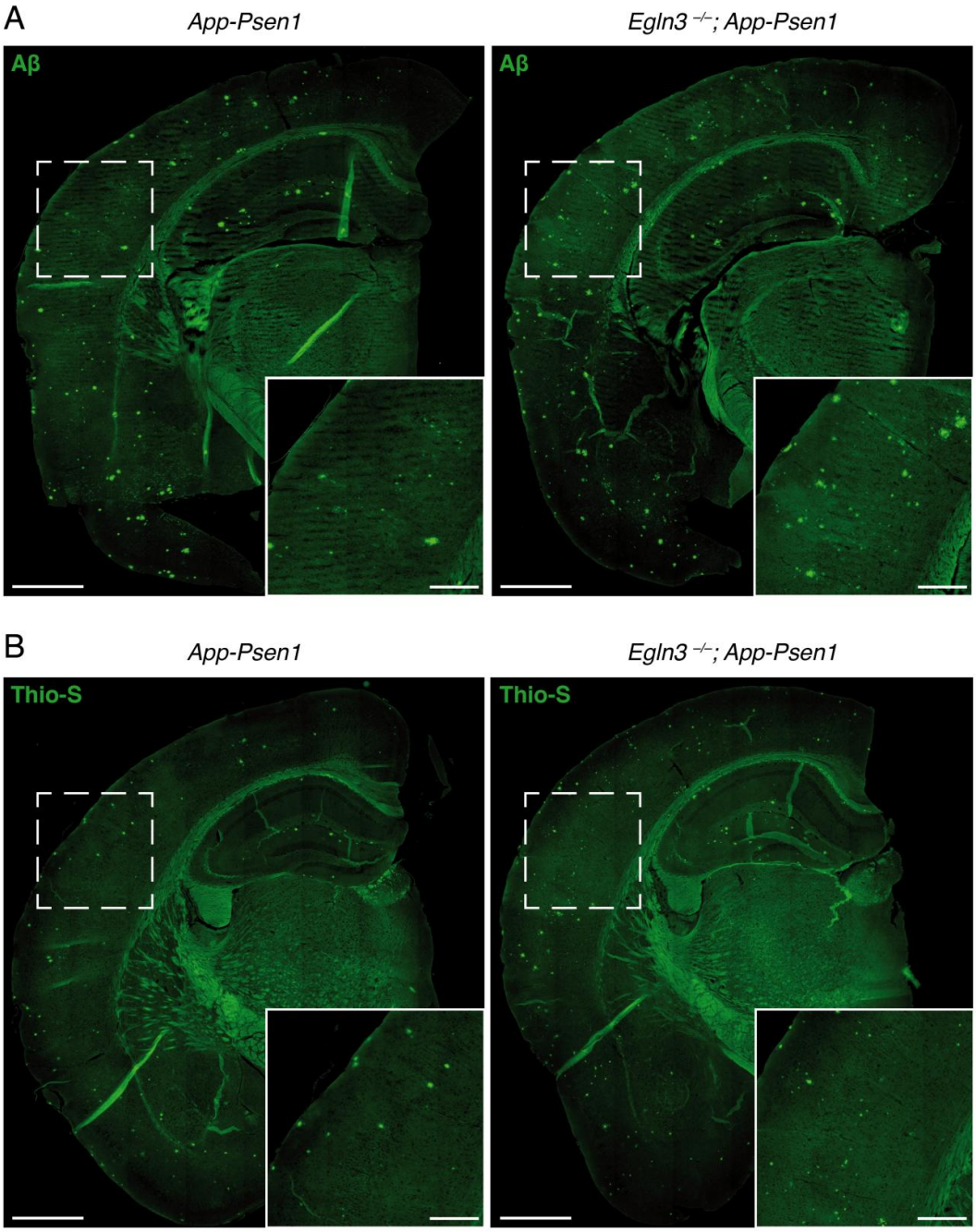

Figure 17. Changes in amyloid-β (Aβ) deposition are observed upon prolyl-hydroxylase 3 (PHD3) absence.

(A-B) Representative superimages of cortical coronal sections from 6 month-old App-Psen1 (left) and Egln3 –/–; App-Psen1 (right) mice immunostained with anti-Aβ (A) antibody and stained with the amyloid plaques dye Thioflavine-S (Thio-S, B). Insets represent higher magnification of areas included in dashed gates. Scale bars are 500 μm for the superimages and 250 μm for the insets.

The anti-Aβ antibody or Thio-S staining are not sensitive enough to accurately quantify fAβ structures. Hence, in order to extend our analysis on Aβ plaques structure and burden, we immunochemically stained hemibrain slices of *App-*

Psen1 and *Egln3* $^{-/-}$*; App-Psen1* mice using anti-OC antibody, which recognizes amyloid fibrillar conformations and fAβ oligomers. We found an extensive OC signal colocalizing with dense-core nuclei of the plaques but also in pure fibrillar structures, mostly surrounding compact plaque's nuclei or, to a lesser extent, as dense-core-devoid Aβ deposits. Since we were particularly focused in the analysis of the fAβ region, we generated segmented binary masks applying an upper and a lower threshold that excluded dense-core-belonging signal (**Figure 19**).

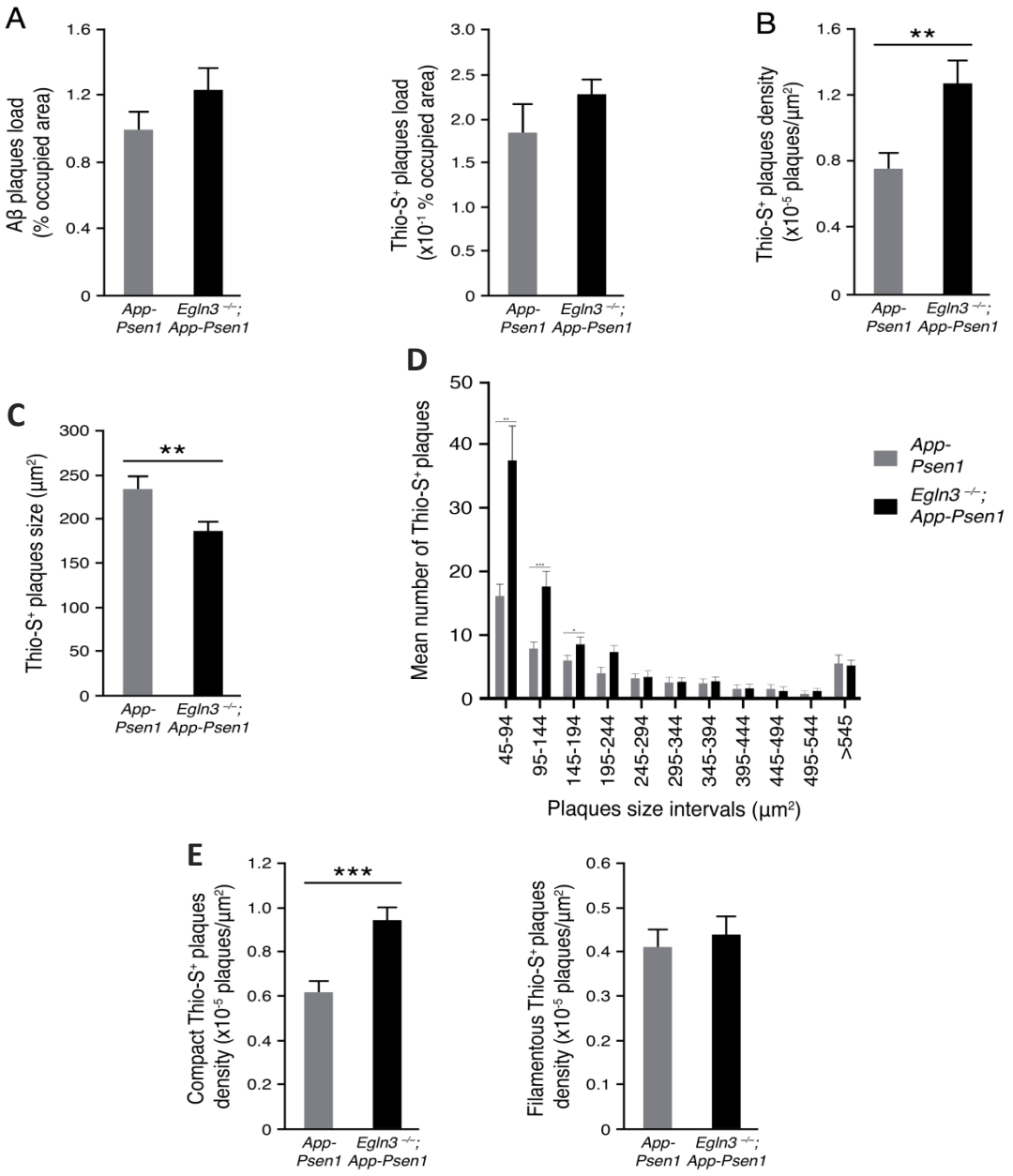

Figure 18. Prolyl-hydroxylase 3 (PHD3) deficiency in Alzheimer's disease (AD) mice shows increased number of small cortical compact amyloid plaques.

(A) Quantification of the percentage of cortical area occupied by amyloid plaques in immunostained with anti-amyloid-β (Aβ) antibody (left) or Thioflavine-S (Thio-S)

staining from superimages described in Fig. 17, A and B, respectively. *App-Psen1* mice, grey bars; *Egln3* $^{-/-}$; *App-Psen1* mice, black bars. * $p < 0.05$; Student's *t*-test; n = 18 hemicortices from 6 mice per genotype for anti-Aβ immunostaining and n = 9 hemicortices from 3 mice per genotype for Thio-S staining. (B-C) Amyloid plaques number per area unit (B) and average size (C) from superimages described in Fig. 17, B. *App-Psen1* mice, grey bars; *Egln3* $^{-/-}$; *App-Psen1* mice, black bars. ** $p < 0.01$; Student's *t*-test; n = 9 hemicortices from 3 mice per genotype. (D) Average number of amyloid plaques in each size interval from superimages described in Fig. 17, B. *App-Psen1* mice, grey bars; *Egln3* $^{-/-}$; *App-Psen1* mice, black bars. * $p < 0.05$; ** $p < 0.01$; *** $p < 0.001$; Student's *t*-test; n = 9 hemicortices from 3 mice per genotype. (E) Number of compact (left) and filamentous (right) amyloid plaques per area unit stereologically quantified in complete hemicortices of *App-Psen1* mice (grey bars) and *Egln3* $^{-/-}$; *App-Psen1* mice (black bars). *** $p < 0.001$; Student's *t*-test; n = 18 hemicortices from 6 mice per genotype. Bars ± error bars represent mean ± s.e.m.

Quantification of percentage of cortical area covered by fAβ, excluding dense-core OC immunohistochemical staining, reflected a significant augmentation of fAβ covered area in the case of *Egln3*$^{-/-}$*; App-Psen1* regarding *App-Psen1* mice (**Figure 20**).

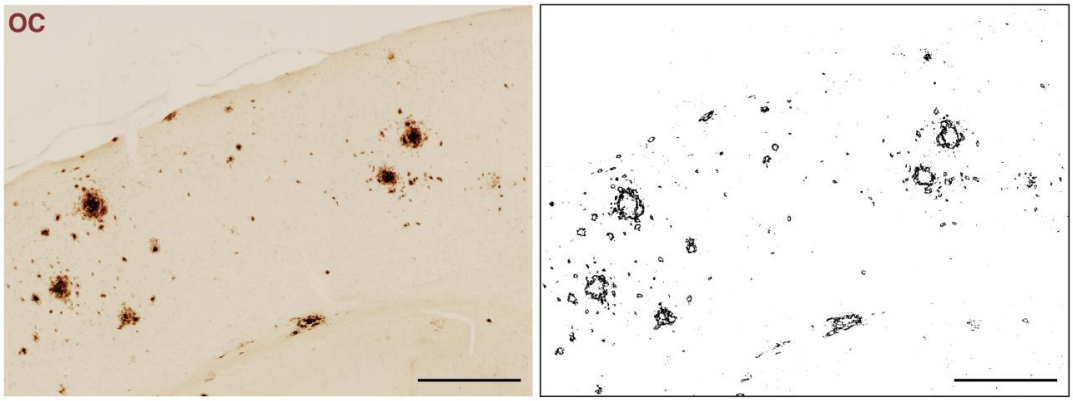

Figure 20. Segmentated binary masks by using Fiji software to detect fibrillar amyloid-β (fAβ) not colocalizing with the dense-core of compact amyloid plaques.

Representative area of a superimage of hemicortical coronal sections from a 6 month-old *App-Psen1* mouse stained with anti-OC antibody (left). Right panel shows the segmented binary mask resulting from left panel after processing with Fiji software by setting lower and upper appropriate thresholds to quantify fAβ. Scale bars are 250 μm.

To sum up, our data indicate that PHD3 deficiency in the *App-Psen1* AD mouse model results in an elevated number of small compact amyloid plaques and fAβ occupied area without altering the number of filamentous plaques or total occupied area by dense-core amyloid plaques.

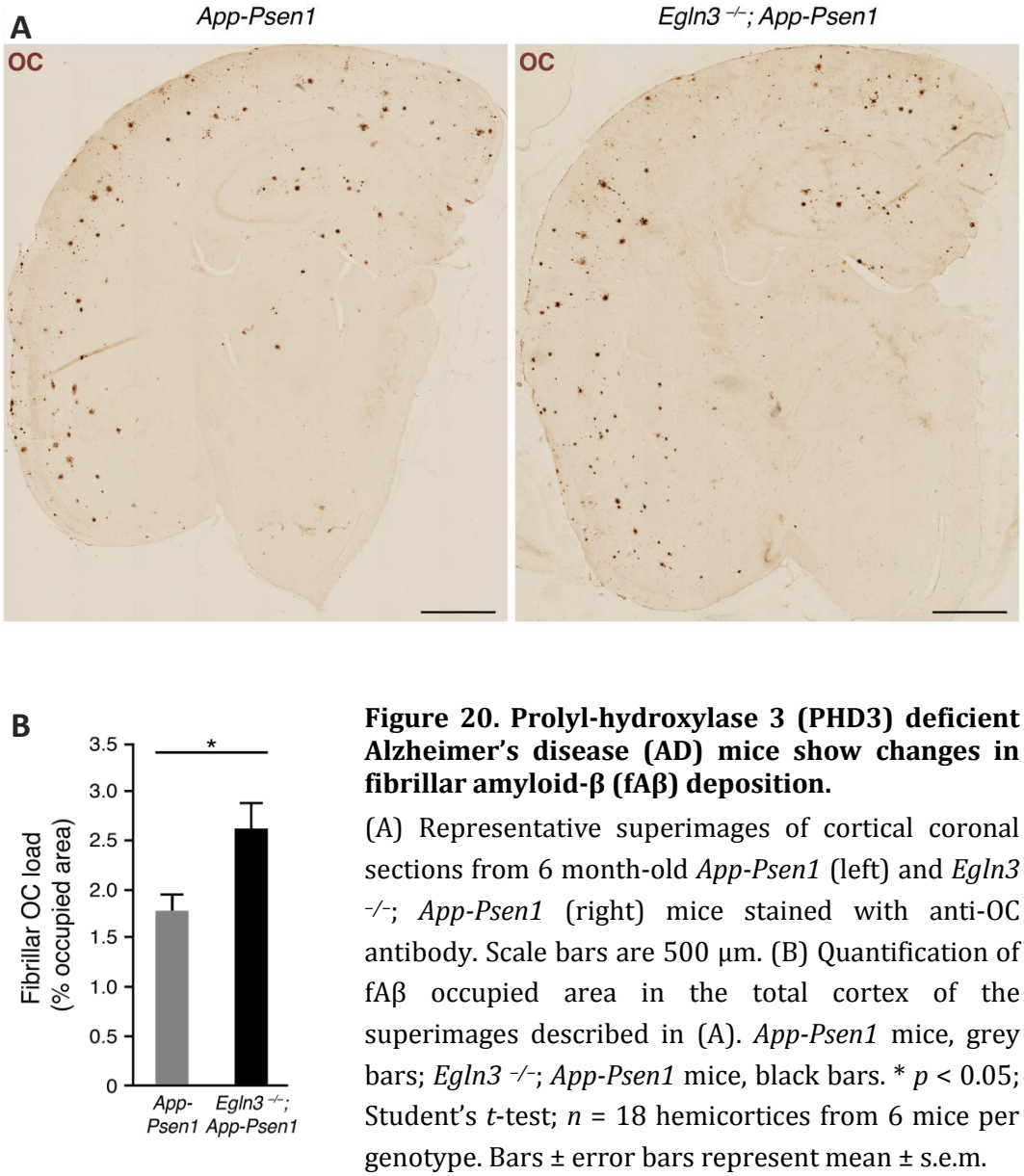

Figure 20. Prolyl-hydroxylase 3 (PHD3) deficient Alzheimer's disease (AD) mice show changes in fibrillar amyloid-β (fAβ) deposition.

(A) Representative superimages of cortical coronal sections from 6 month-old *App-Psen1* (left) and *Egln3* $^{-/-}$; *App-Psen1* (right) mice stained with anti-OC antibody. Scale bars are 500 μm. (B) Quantification of fAβ occupied area in the total cortex of the superimages described in (A). *App-Psen1* mice, grey bars; *Egln3* $^{-/-}$; *App-Psen1* mice, black bars. * $p < 0.05$; Student's *t*-test; $n = 18$ hemicortices from 6 mice per genotype. Bars ± error bars represent mean ± s.e.m.

4.2.5. A decreased neurotoxicity is exhibited upon *Egln3* deletion

It has been described that fAβ configurations exert a more neurotoxic effect than compact formations (Condello et al., 2015; Yuan et al., 2016). Given that *Egln3* $^{-/-}$; *App-Psen1* mice presented higher fAβ coverage, we measured neuronal

dystrophies around Aβ plaques using a phosphorylated-Tau protein antibody (**Figure 21**). We selected random compact plaques of the same size (**Figure 21, B**) from the cortex of *Egln3* $^{-/-}$*; App-Psen1* and *App-Psen1* mice stained with anti-phosphorylated-Tau antibody and Thio-S and estimated P-Tau occupied area around the plaques. Unexpectedly, we observed a significantly reduced proportion of P-Tau around plaques (**Figure 21, C**) in *Egln3* $^{-/-}$*; App-Psen1* mice.

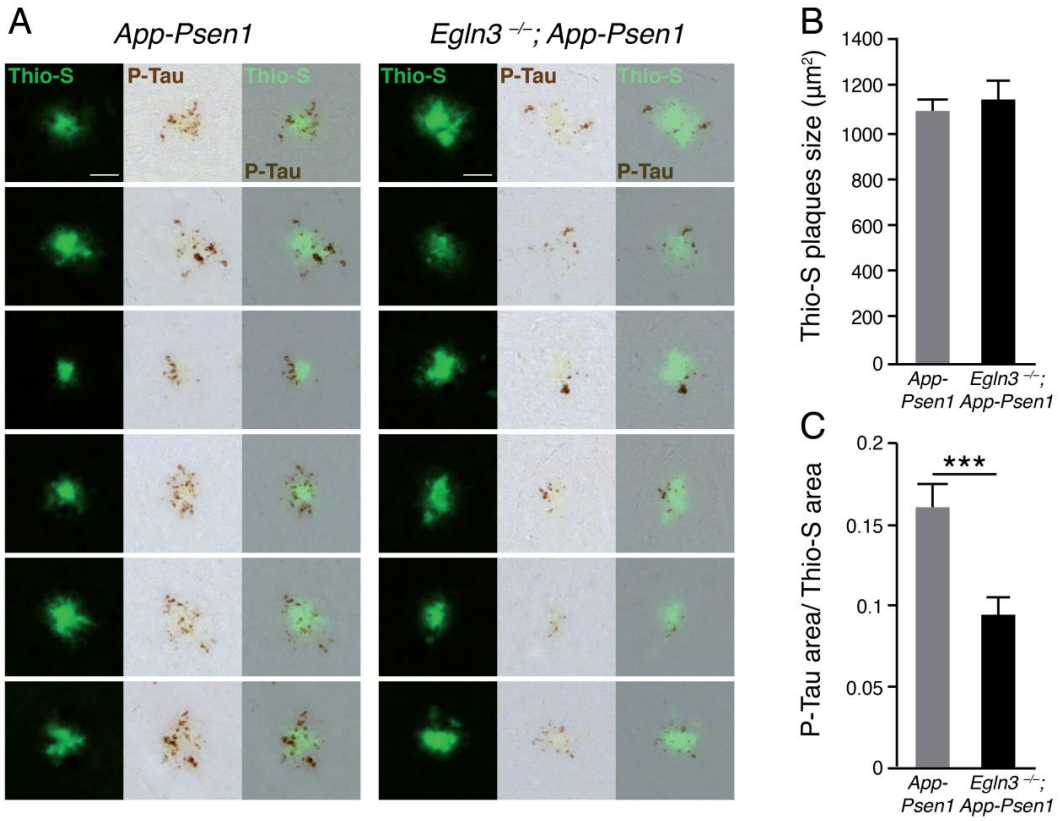

Figure 21. Neuronal dystrophies surrounding compact amyloid plaques are reduced upon prolyl-hydroxylase 3 (PHD3) ablation in AD mice.

(A) Representative images of cortical random compact amyloid-β (Aβ) plaques from 6 month-old *App-Psen1* (left) and *Egln3* $^{-/-}$; *App-Psen1* (right) mice stained with Thioflavine-S (Thio-S, green) (left column in each panel) and associated neuronal damage immunostained with anti-phosphorylated-Tau (P-Tau, brown) antibody (central column in each panel). Right column in each panel shows colocalization of Thio-S and P-Tau markers. Scale bars are 50 µm (B) Aβ plaques size from images described in A. *App-Psen1* mice, grey bars; *Egln3* $^{-/-}$; *App-Psen1* mice, black bars. *p < 0.05; Student's *t*-test; n = 30 hemicortices from 5 mice per genotype (24 plaques per mouse). (C) Ratio P-Tau /amyloid plaque occupied area from images described in A. *App-Psen1* mice, grey bars; *Egln3* $^{-/-}$; *App-Psen1* mice, black bars. *** p < 0.001; Student's *t*-test; n = 30 hemicortices from 5 mice per genotype (24 plaques per mouse). Bars ± error bars represent mean ± s.e.m.

We wondered if this result could be explained by a decrease in the fAβ halo specifically surrounding the *Egln3* $^{-/-}$*; App-Psen1* compact plaques. To address this question, we immunostained cortical sections of *Egln3* $^{-/-}$*; App-Psen1* and *App-Psen1* with Thio-S and anti-OC antibody to quantify total OC signal covered area, OC occupancy exclusively by fAβ halo, and Thio-S dense-core size in plaques meeting the same criteria used for neuronal dystrophies quantification (**Figure 22**). Non-significant differences were observed in all the analyzed parameters (total fAβ, Thio-S dense core or fibrillar halo area), including the ratio between fibrillar halo/dense-core covered areas per plaque (**Figure 23**).

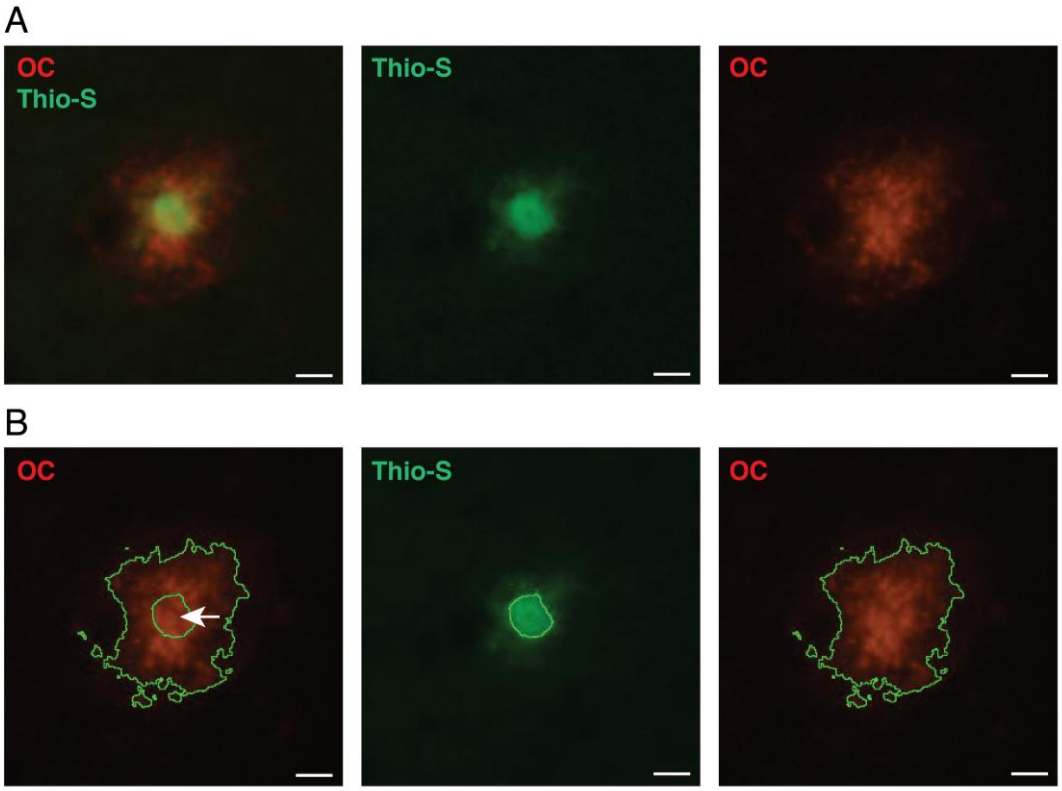

Figure 22. Considered dense core and fibrillar amyloid-β (fAβ) halo in compact amyloid plaques.

(A) Representative picture of a compact amyloid plaque from the cortex of a 6-month-old *App-Psen1* mouse stained with Thioflavine-S (Thio-S, green), and immunostained with anti-OC antibody (red). Left panel shows colocalization of both markers, centre panel shows Thio-S staining and right panel shows OC staining. Scale bars are 10 μm. (B) Contour shapes delimiting the whole OC marker quantified area (right), the dense core (centre) or the fAβ halo excluding the dense core (white arrow, left) in the amyloid plaque from A after processing with Fiji software. Scale bars are 10 μm.

These results are consistent with a neuroprotective effect around amyloid plaques in the absence of PHD3 that is not due to modifications of the fAβ plaques-surrounding halo.

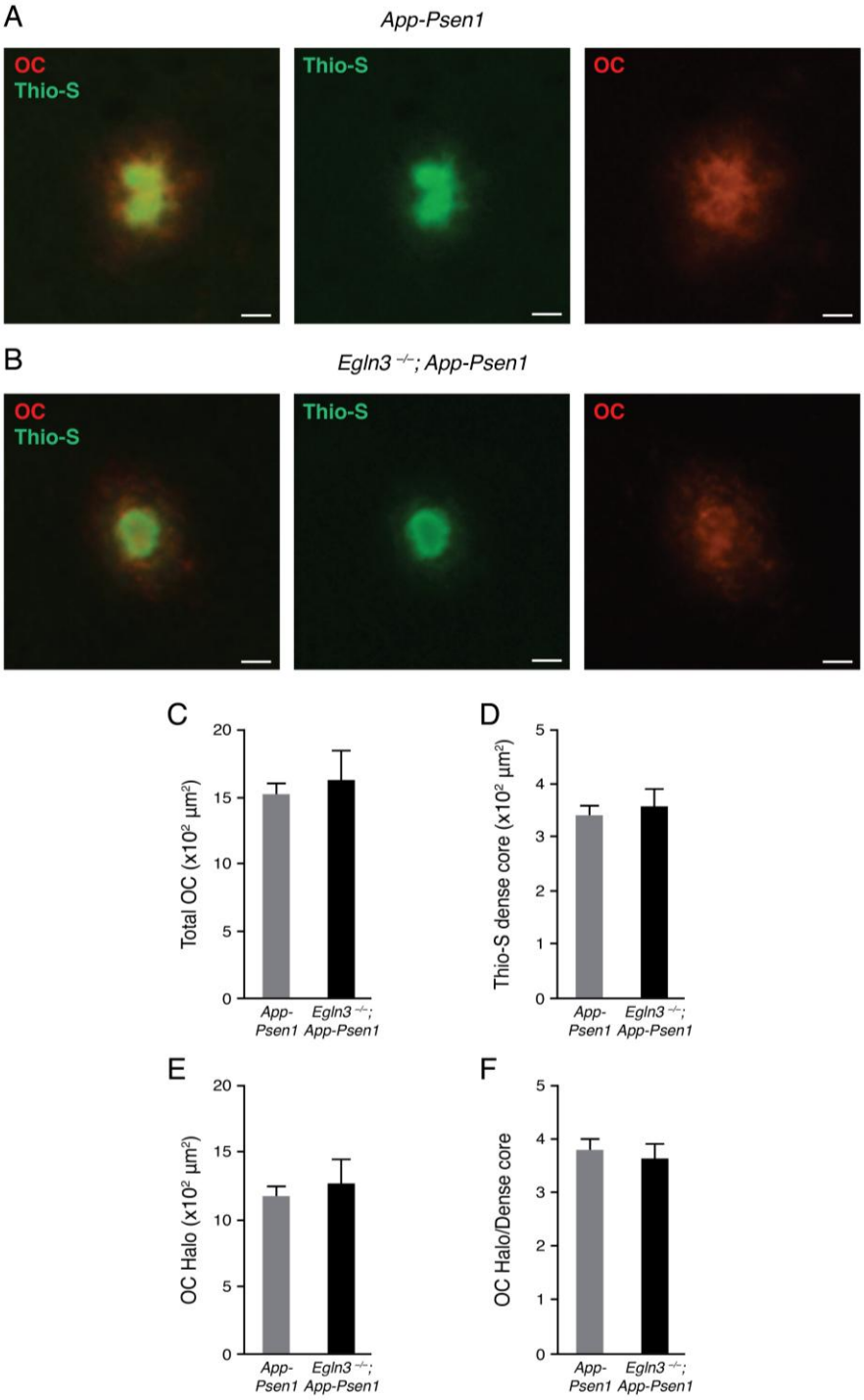

Figure 23. Compact amyloid plaques do not exhibit structural changes in their fibrillar amyloid-β (fAβ) halo in prolyl-hydroxylase 3 (PHD3) deficient AD mice.

(A-B) Representative cortical compact amyloid plaques from 6 month-old *App-Psen1* (A) and *Egln3* $^{-/-}$; *App-Psen1* (B) mice stained with Thioflavine-S (Thio-S, green) and immunostained with anti-OC antibody (red). Right panel shows OC immunostaining,

centre panel shows Thio-S staining and left panel shows colocalization of both markers. Scale bars are 10 μm. (C) Quantified area occupied by total OC marker in cortical compact amyloid plaques from images described in A-B. *App-Psen1* mice, grey bar; *Egln3* $^{-/-}$; *App-Psen1* mice, black bar. * $p < 0.05$; Student's *t*-test; $n = 18$ hemicortices from 6 mice per genotype (15 plaques per mouse). (D) Quantified dense core occupied by Thio-S marker in cortical compact amyloid plaques from the same plaques in C. *App-Psen1* mice, grey bar; *Egln3* $^{-/-}$; *App-Psen1* mice, black bar. * $p < 0.05$; Student's *t*-test; $n = 18$ hemicortices from 6 mice per genotype (15 plaques per mouse). (E) Quantified area occupied by OC halo surrounding Thio-S dense core in cortical compact amyloid plaques from the same plaques in C. *App-Psen1* mice, grey bar; *Egln3* $^{-/-}$; *App-Psen1* mice, black bar. * $p < 0.05$; Student's *t*-test; $n = 18$ hemicortices from 6 mice per genotype (15 plaques per mouse). (F) Ratio OC halo/dense core occupied areas from the same plaques in C. *App-Psen1* mice, grey bar; *Egln3* $^{-/-}$; *App-Psen1* mice, black bar. * $p < 0.05$; Student's *t*-test; $n = 18$ hemicortices from 6 mice per genotype (15 plaques per mouse). Bars ± error bars represent mean ± s.e.m.

4.2.6. Microglia association to Aβ plaques is triggered in the absence of PHD3

Microglia can exert a physical barrier function by isolating neurons from Aβ toxicity (Condello et al., 2015). Indeed, in *Trem2* haplodeficient AD-like mice, which exhibit a significant decrease in plaque coverage by microglia, neuronal dystrophies surrounding amyloid plaques are more prominent (Yuan et al., 2016). In order to evaluate a potentially enhanced microglial barrier in *Egln3* $^{-/-}$*; App-Psen1* mice, we immunostained cortical slices with IBA1 and DAPI markers to identify individual microglial cells, in combination with Thio-S staining, and we acquired images at different Z axis points of compact Aβ plaques of the same size (**Figure 24**). Next, we calculated a microglia proximity index (MPI) that represents the proportion of microglia directly contacting the amyloid plaque within a 40 μm halo from plaque's border. This approach revealed a significant increase in the MPI of *Egln3* $^{-/-}$*; App-Psen1* with respect to *App-Psen1* mice (**Figure 24, C**). This increased MPI did not correlate with differences in microglia number around Aβ plaques (**Figure 24, D**). Thus, microglia in *Egln3* $^{-/-}$*; App-Psen1* mice exhibit a closer physical interaction with Aβ plaques that could presumably increase microglia shielding from plaque's neurotoxicity, suggesting a neuroprotective role of microglia in *Egln3* $^{-/-}$*; App-Psen1* mice.

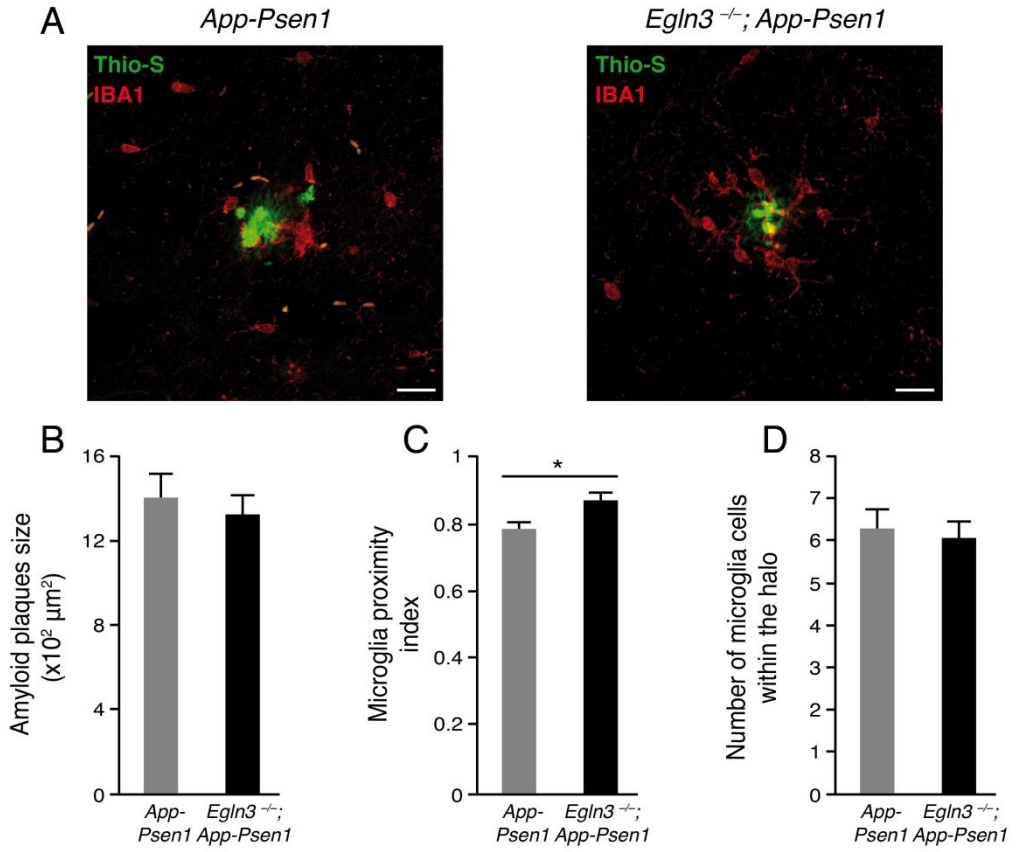

Figure 24. Microglia association to amyloid-β (Aβ) plaques is triggered in the absence of prolyl-hydroxylase 3 (PHD3) in Alzheimer's disease (AD) mouse models.

(A) Representative cortical coronal confocal images of compact amyloid plaques stained with Thioflavine-S (Thio-S, green) and microglia immunostained with anti-IBA1 (red) antibody from 6 month-old *App-Psen1* (left) and *Egln3* $^{-/-}$; *App-Psen1* (right) mice. Scale bars are 20 µm. (B) Size quantification of compact amyloid plaques immunostained with anti-Aβ antibody from 6 month-old *App-Psen1* (grey bar) and *Egln3* $^{-/-}$; *App-Psen1* (black bar) mice. * $p < 0.05$; Student's *t*-test; $n = 9$ hemicortices from 3 mice per genotype (15 plaques per mouse). (C) Microglia proximity index: number of microglia cells, immunostained with anti-IBA1 antibody and with the nuclear dye DAPI, in contact with Aβ plaques per total microglia within a 40 µm halo around the plaque in 6 month-old *App-Psen1* (grey bar) and *Egln3* $^{-/-}$; *App-Psen1* (black bar) mice. * $p < 0.05$; Mann Whitney's test; $n = 9$ hemicortices from 3 mice per genotype (15 plaques per mouse). (D) Number of microglial cells, immunostained with anti-IBA1 antibody and with the nuclear dye DAPI, within a 40 µm halo around amyloid plaques from 6 month-old *App-Psen1* (grey bar) and *Egln3* $^{-/-}$; *App-Psen1* (black bar) mice. * $p < 0.05$; Student's *t*-test; $n = 9$ hemicortices from 3 mice per genotype (15 plaques per mouse). Bars ± error bars represent mean ± s.e.m.

To further support an increased barrier function, we immunostained whole cortical slices with IBA1 antibody and analyzed them with Fiji software (Schindelin

et al., 2012) by using a combination of settings aimed at recognizing microglial cell clusters. We observed a significant increase in clustered microglial burden in *Egln3* $^{-/-}$*; App-Psen1 versus App-Psen1* mice, suggesting increased microglial coverage around amyloid plaques (**Figure 25**).

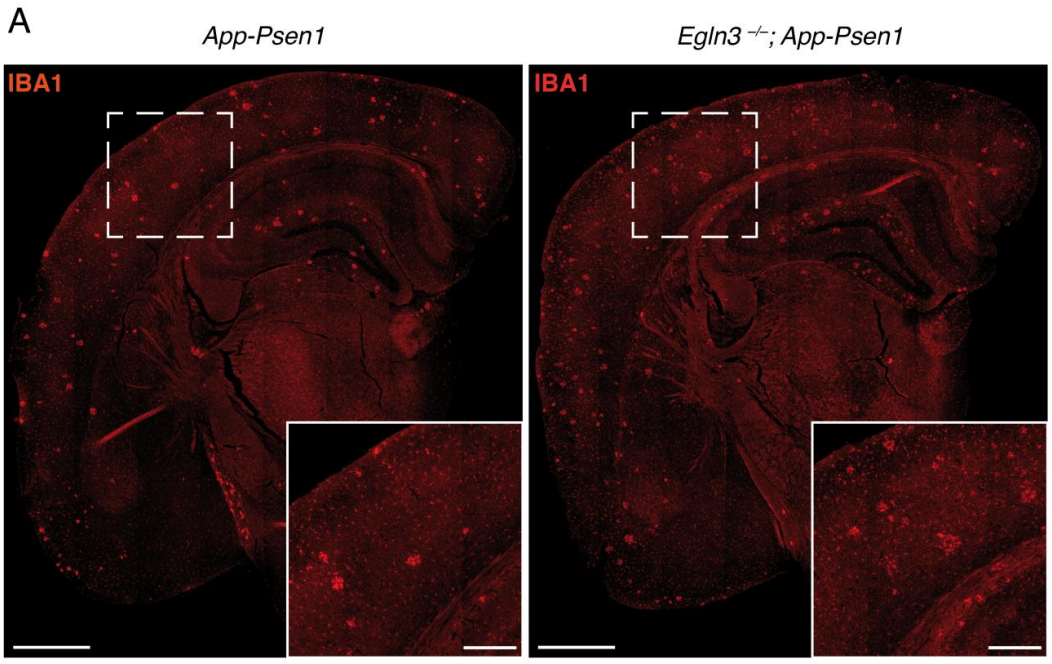

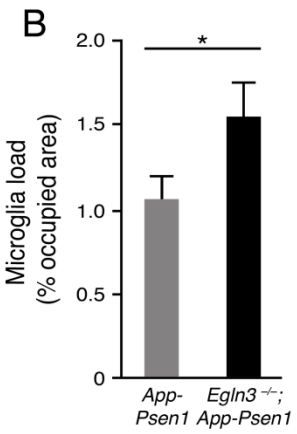

Figure 25. Prolyl-hydroxylase 3 (PHD3) ablation in Alzheimer's disease (AD) mice correlates with an increased cortical coverage of clustered microglia.

(A) Representative superimages of cortical coronal sections from 6 month-old *App-Psen1* (left) and *Egln3* $^{-/-}$; *App-Psen1* (right) mice immunostained with anti-IBA1 antibody. Insets represent higher magnification of areas included in dashed gates. Scale bars are 500 µm for the superimages and 250 µm for the insets. (B) Quantification of the percentage of cortical area occupied by clustered microglia from images described in A. *App-Psen1* mice, grey bar; *Egln3* $^{-/-}$; *App-Psen1* mice, black bar. * $p < 0.05$; Student's *t*-test; $n = 18$ hemicortices from 6 mice per genotype. Bars ± error bars represent mean ± s.e.m.

To discard a potential contribution of non-clustered microglial cells to the calculated burden, we analyzed different morphological aspects of microglia far from Aβ plaques. Upon immunostaining with IBA1 antibody, we explored the level of ramification of microglial projections by counting the number of primary branches, which emerge directly from the soma, and the number of intersections with a circumference of fixed size **(Figure 26, A, green)**. We observed no

differences in *App-Psen1 versus Egln3 $^{-/-}$; App-Psen1* mice, either in the number of primary branches or in the number of intersections (**Figure 26, C-D**).

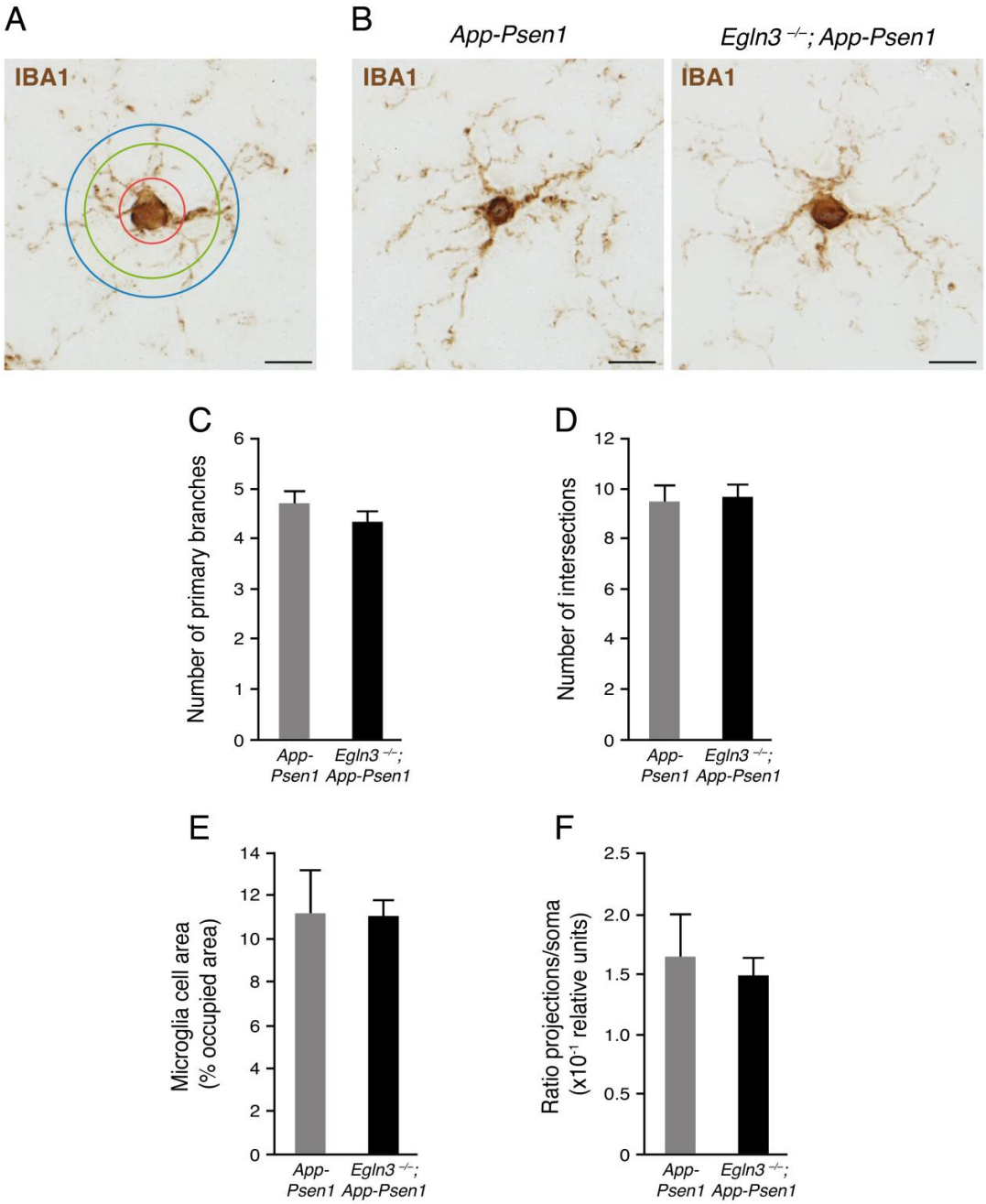

Figure 26. Microglia morphology is not altered in prolyl-hydroxylase 3 (PHD3) deficient microglia far from amyloid plaques.

(A-C) Representative microglia of cortical coronal sections from 6 month-old *App-Psen1* (B, left) and *Egln3 $^{-/-}$*; *App-Psen1* (B, right) mice immunostained with anti-IBA1 antibody. Scale bars are 10 µm. (A) Green circumference was used to quantify the number of intersections with microglial projections. Red circumference was used to measure the occupied area by soma within this circumference. Blue circumference was used to analyze microglia occupied area within this circumference and area occupied by microglial projections, excluding the area

delimited by red circumference. (C) Number of primary branches emerging directly from microglial soma quantified in images described in B. *App-Psen1* mice, grey bar; *Egln3* $^{-/-}$; *App-Psen1* mice, black bar. * $p < 0.05$; Student's *t*-test; $n = 9$ hemicortices from 3 mice per genotype (9 cells per mouse). (D) Number of intersections in images described in B with green circumference in A. *App-Psen1* mice, grey bar; *Egln3* $^{-/-}$; *App-Psen1* mice, black bar. * $p < 0.05$; Student's *t*-test; $n = 9$ hemicortices from 3 mice per genotype (9 cells per mouse). (E) Microglia occupied area in images described in B with blue circumference in A. *App-Psen1* mice, grey bar; *Egln3* $^{-/-}$; *App-Psen1* mice, black bar. * $p < 0.05$; Student's *t*-test; $n = 18$ hemicortices from 6 mice per genotype (9 cells per mouse). (F) Ratio projections/soma occupied area in the images described in B with red and blue circumferences described in A. *App-Psen1* mice, grey bar; *Egln3* $^{-/-}$; *App-Psen1* mice, black bar. * $p < 0.05$; Student's *t*-test; $n = 18$ hemicortices from 6 mice per genotype (9 cells per mouse). Bars ± error bars represent mean ± s.e.m.

Given the heterogeneity of microglial morphology, we complemented the morphological study with an unbiased approach based on the percentage of area covered by individual microglial cells in a specifically selected circumference (**Figure 26, A, blue**). Our results showed the same occupancy of individual microglial cells within the blue circumference for *App-Psen1* and *Egln3* $^{-/-}$*; App-Psen1* mice (**Figure 26, E**). Although the occupied area of individual cells was unmodified in this comparison, it was still possible to have variances in the ratio of projections and soma. To explore this possibility, we quantified the area covered by projections and soma of individual cells by using a similar unbiased strategy. We created a smaller fixed area which was placed in the center of the soma of every microglial cell to quantify the percentage of occupancy of the corresponding soma regarding this constant area (**Figure 26, A, red**). Afterwards, by using the same previously described area to measure whole cell coverage (**Figure 26, A, blue**), we quantified the proportion of area occupied by IBA1 marker excluding the signal contained in the red circumference (**Figure 26, A, red**). We decided not to just subtract soma area to the precedent calculated total area because, with this bit by bit approach, we could adopt more appropriate threshold settings for each compartment in order to improve the quality of data. With this separate quantification, we calculated the ratio between projection and soma areas and we did not observe significant differences in the calculated ratio in *App-Psen1 versus Egln3* $^{-/-}$*; App-Psen1* microglia (**Figure 26, F**).

Altogether, these results strongly support an enhanced microglial encapsulation of compact amyloid plaques upon PHD3 deficiency with neuroprotective effects.

4.2.7. PHD3 depletion rescues motor and memory abnormalities emerging from AD

Reduction in the number of synapses has been reported in AD animal models upon Tau hyperphosphorylation (Pooler et al., 2014). In order to explore whether the detected differences in Tau hyperphosphorylation load between *App-Psen1* and *Egln3* $^{-/-}$*; App-Psen1* could result in differential synaptic affectation, we measured the hippocampal content of three different synaptic proteins by WB. We also included a control group composed by *wild-type* and *Egln3* $^{-/-}$ mice, since no differences were observed between them, in order to identify a potential defect exerted by Aβ accumulation.

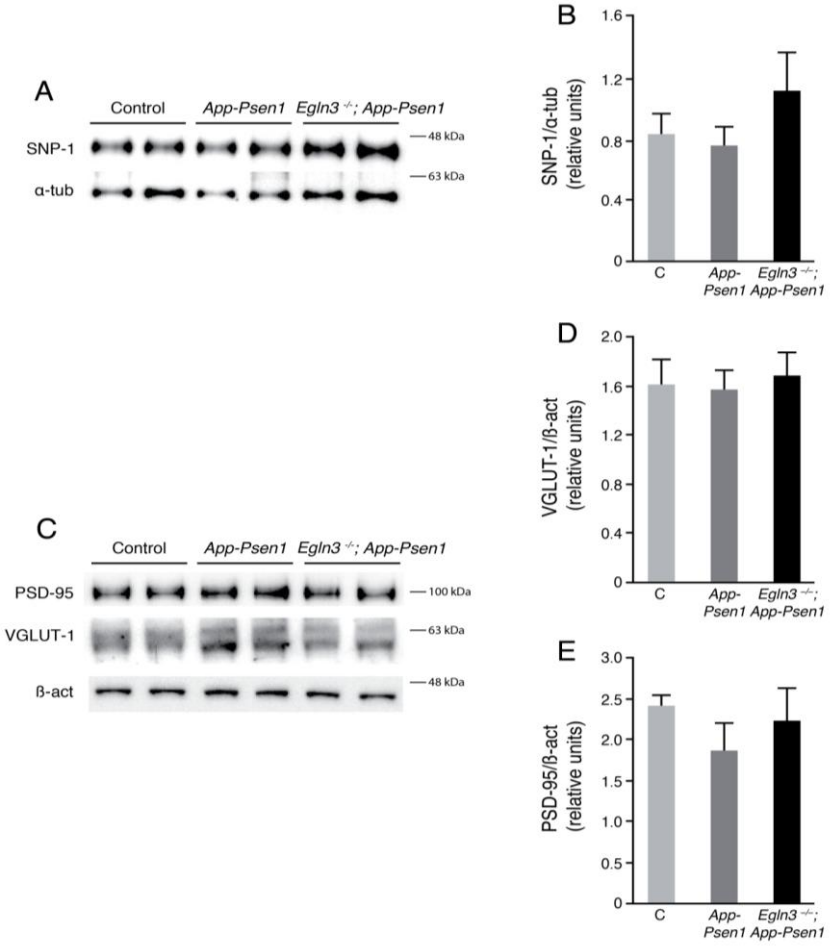

Figure 27. Synaptic proteins load is not altered in Alzheimer's disease (AD) mice upon prolyl-hydroxylase 3 (PHD3) absence.

(A-E) Western blot (WB) and quantifications from hippocampal extracts of 6 month-old control (wild-type and *Egln3* $^{-/-}$, light grey bars) *App-Psen1* (dark grey bars) and

Egln3 $^{-/-}$; *App-Psen1* (black bars) mice. (A) Representative WB for synaptophysin protein (SNP-1), with α-tubulin (α-tub) as loading control. (B) Quantification of the WB described in A. * $p < 0.05$; Kruskal-Wallis ANOVA with Dunn's multiple comparison test; $n = 11$ hemihippocapi from control mice, $n = 7$ hemihippocapi from *App-Psen1* mice, $n = 6$ hemihippocapi from *Egln3* $^{-/-}$; *App-Psen1* mice. (C) Representative WB for postsynaptic-density-95 (PSD-95) protein (upper row) and vesicular glutamate transporter (VGLUT-1) (lower row) with β-actin (β-act) as loading control. (D) Quantification of the WB for VGLUT-1 described in C. * $p < 0.05$; ANOVA with Tukey's post-test; $n = 11$ hemihippocapi from control mice, $n = 7$ hemihippocapi from *App-Psen1* mice, $n = 6$ hemihippocapi from *Egln3* $^{-/-}$; *App-Psen1* mice. (E) Quantification of the WB for PSD-95 described in C. * $p < 0.05$; Kruskal-Wallis ANOVA with Dunn's multiple comparison test; $n = 11$ hemihippocapi from control mice, $n = 7$ hemihippocapi from *App-Psen1* mice, $n = 6$ hemihippocapi from *Egln3* $^{-/-}$; *App-Psen1* mice. Bars ± error bars represent mean ± s.e.m.

Synaptophysin is a 38 kDa integral membrane glycoprotein that is restricted to the presynaptic compartment (Martin et al., 2014). Our results revealed no differences in synaptophysin-1 load among the aforementioned groups (**Figure 27, A-B**). Synaptic development, neural plasticity, and protein assembly in the postsynaptic compartment are mediated by postsynaptic-density-95 (PSD-95) protein, whose decrease has been found in different AD-related scenarios (Tu et al., 2014). PSD-95 levels showed non-significant alterations in any of the analyzed groups (**Figure 27, C, E**). Finally, vesicular glutamate transporter (VGLUT-1) levels were evaluated in the same samples since they are modified in AD (Kashani et al., 2008). No differences were observed in VGLUT-1 levels among the hippocampi of our mice groups (**Figure 27, C, D**).

Plaque-associated axonal dystrophies correlate with cognitive impairment (Dickson et al., 1999; Su et al., 1996). Therefore, although we did not detected differences in synaptic proteins load, we wondered if the observed reduction in plaque-associated peripheral dystrophies could possess further cognitive implications. To answer this question, we carried out behavioral assays regarding free locomotor activity in an open-field test and memory with a novel-object recognition test, in the aforementioned control, *App-Psen1* and *Egln3* $^{-/-}$*; App-Psen1* groups. In the open-field test, spontaneous activity was examined by recording track length for fifteen minutes in an open-field chamber. We obtained an elevated locomotor activity in *App-Psen1* regarding the control group, as already observed in previous studies using other AD mouse models (Heneka et al., 2013; Walker et

al., 2011). Remarkably, this increased locomotion was completely blunted in *Egln3*$^{-/-}$*; App-Psen1*, reverting this defect to the control group phenotype (**Figure 28, A**). Memory assessment was performed with a novel object recognition test, in which we obtained a short-term memory index calculated as the number of approaches of each mouse to a new object that replaced one of the two objects presented one hour before, divided by the total number of approaches to both objects. Our results showed a deficient hippocampal-dependent memory retention in *App-Psen1* mice regarding the control group that was fully rescued in *Egln3*$^{-/-}$*; App-Psen1* mice (**Figure 28, B**).

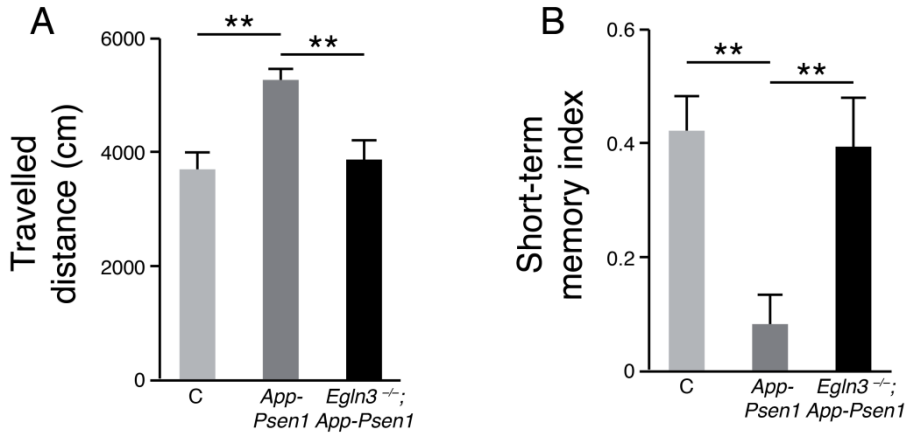

Figure 28. Prolyl-hydroxylase 3 (PHD3) absence rescues motor and short-term memory defects associated to Alzheimer's disease (AD).

(A) Spontaneous activity was measured in control (*wild-type* and *Egln3* $^{-/-}$, light grey bar), *App-Psen1* (dark grey bar), and *Egln3* $^{-/-}$; *App-Psen1* (black bar) mice. Mice were recorded for 15 min in an open field chamber (n = 16 control, n = 18 *App-Psen1*, and n = 14 *Egln3* $^{-/-}$; *App- Psen1* mice. ** $p < 0.01$; ANOVA with Tukey's post-test. (B) Short term memory index (1 h inter-session interval) was calculated in control (*wild-type* and *Egln3* $^{-/-}$), *App-Psen1* and *Egln3* $^{-/-}$; *App-Psen1* mice using the novel object recognition test (n = 14 control, n = 21 *App-Psen1*, and n = 14 *Egln3* $^{-/-}$; *App-Psen1* mice. ** $p < 0.01$; ANOVA with Newman-Keuls' post-test). (A-B) Bars ± error bars represent mean ± s.e.m.

These results account for a cognitive and motor behavior improvement mediated by PHD3 depletion in AD.

4.2.8. *Egln3* ablation does not trigger a microglial hypoxic response

In order to explore the potential mechanisms explaining the phenotypic differences detected in the microglia from *Egln3* $^{-/-}$*; App-Psen1* with regards to

microglia from *App-Psen1* mice, we isolated the CD11b/CD45 positive microglia from these two mouse models by FACS and performed microarray experiments and GSEA.

Processing and GSEA of data obtained from the microarray of isolated microglia were performed by Dr. Ortega-de San Luis. However, we include them in this manuscript since they provide important clues on functional mechanisms to explain our results.

Significant transcriptional changes in the comparison *Egln3 $^{-/-}$; App-Psen1 versus App-Psen1* microglia were considered when logFC (log2 scale) ≥ ±0.5 and *p*-value < 0.05. A table listing significant transcriptional changes is attached in "attached material" section (**Table 5**).

One of the expected effects of *Egln3* deletion could be HIF1α accumulation and subsequent activation of its target genes since PHD3 is involved in a negative feedback loop that promotes HIF1α stabilization *in vitro* (Ginouves et al., 2008). In this regard, WB analysis of the nuclear fraction of cortical homogenates from *App-Psen1* and *Egln3 $^{-/-}$; App-Psen1* mice showed no differences in HIF1α amount between *Egln3 $^{-/-}$; App-Psen1* and *App-Psen1* mice (**Figure 29**).

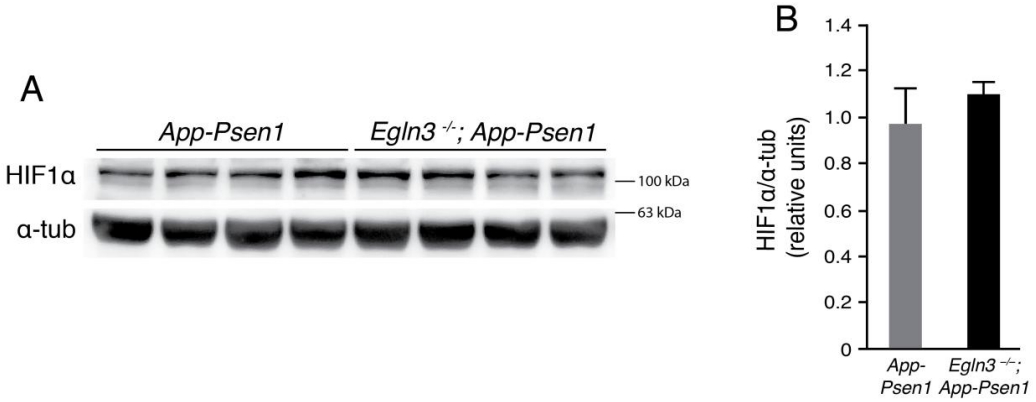

Figure 29. Hypoxia-inducible factor (HIF)1α protein levels are not modified by prolyl-hydroxylase 3 (PHD3) deficiency in Alzheimer's disease (AD) mice.

(A-B) Western blot (WB) and quantifications from cortical extracts of 6 month-old *App-Psen1* (dark grey bars) and *Egln3 $^{-/-}$; App-Psen1* (black bars) mice. (A) Representative WB for HIF1α protein, with α-tubulin (α-tub) as loading control. (B) Quantification of the WB described in A. * $p < 0.05$; Student's *t*-test; $n = 4$ hemicortices per genotype. Bars ± error bars represent mean ± s.e.m.

To further confirm that *Egln3* deficiency did not exacerbate a hypoxic response in AD microglia, a GSEA was carried out using "Biological Processes" category (which is integrated by 730 GS, including an endogenous "Response to Hypoxia" GS). As hypoxia-regulated responses are extremely cell specific (Ortiz-Barahona et al., 2010; Schödel et al., 2013), a custom GS representing the HMS, which had previously been defined in our laboratory, was added to the analysis.

Name	Size	ES	NES	NOM p-val	FDR q-val	FWER p-val	Rank at max	Leading edge
AROMATIC COMPOUND METABOLIC PROCESS	24	0.68	1.99	0.0	0.06	0.078	2420	tags=54%, list=18%, signal=66%
EPIDERMIS DEVELOPMENT	66	0.53	1.89	0.0	0.15	0.328	2713	tags=38%, list=21%, signal=47%
ECTODERM DEVELOPMENT	74	0.52	1.87	0.0	0.13	0.414	2713	tags=38%, list=21%, signal=47%
SKELETAL DEVELOPMENT	93	0.47	1.78	0.0013	0.27	0.782	3825	tags=52%, list=29%, signal=72%
FEEDING BEHAVIOR	21	0.62	1.74	0.0106	0.32	0.891	3818	tags=71%, list=29%, signal=100%
TISSUE DEVELOPMENT	125	0.44	1.73	0.0	0.31	0.92	3958	tags=47%, list=30%, signal=67%
REGULATION OF PH	13	0.69	1.73	0.0033	0.28	0.927	1714	tags=54%, list=13%, signal=62%
REGULATION OF HEART CONTRACTION	23	0.60	1.72	0.0046	0.27	0.943	736	tags=22%, list=6%, signal=23%
SPERMATID DIFFERENTIATION	11	0.70	1.70	0.0081	0.32	0.975	1378	tags=45%, list=10%, signal=51%
MONOVALENT INORGANIC CATION HOMEOSTASIS	14	0.66	1.68	0.0141	0.31	0.98	1714	tags=50%, list=13%, signal=57%
DEVELOPMENT OF PRIMARY SEXUAL CHARACTERISTICS	24	0.56	1.64	0.0151	0.42	0.998	4142	tags=67%, list=31%, signal=97%
SPERM MOTILITY	10	0.71	1.63	0.0196	0.40	0.998	1853	tags=70%, list=14%, signal=81%
SPERMATID DEVELOPMENT	10	0.70	1.62	0.0204	0.38	0.998	1378	tags=50%, list=10%, signal=56%
AMINO ACID DERIVATIVE METABOLIC PROCESS	21	0.58	1.62	0.0123	0.36	0.998	2420	tags=38%, list=18%, signal=47%
REGULATION OF CELLULAR PH	10	0.70	1.61	0.0147	0.39	0.998	1714	tags=60%, list=13%, signal=69%

Table 2. The hypoxia-induced microglia signature (HMS) gene set (GS) is not over-represented in prolyl-hydroxylase 3 (PHD3) deficient Alzheimer's disease (AD) microglia.

Top fifteen up-regulated GS in 12-month-old isolated microglia from *Egln3* $^{-/-}$; *App-Psen1 versus App-Psen1* mice revealed by Gene Set Enrichment Analysis (GSEA) using Biological Processes category and including HMS as an additional GS.

We observed that neither endogenous Biological Processes category Response to Hypoxia GS nor the HMS were overrepresented in *Egln3 $^{-/-}$; App-Psen1* microglia in comparison with *App-Psen1* microglia (**Table 2**). Altogether, these results suggest that PHD3 absence is not aggravating a hypoxic microglial expression profile in a β-amyloidosis context.

4.2.9. Microglia activates anti-microbial responses in a PHD3-dependent manner

In order to explore the pathways regulated by PHD3 in AD microglia, GSEA was performed based on "KEGG pathway database" category contained GS (171 GS). Top ten up-regulated and down-regulated GS are listed in **Tables 3** and **4**, respectively. Up-regulated GS in the microglia from *Egln3 $^{-/-}$; App-Psen1* compared to *App-Psen1* mainly reflected a profound adjustment of the metabolic status of the cells (**Table 3**), evidencing further physiological implications.

Name	Size	ES	NES	NOM p-val	FDR q-val	FWER p-val	Rank at max	Leading edge
KEGG TYROSINE METABOLISM	34	0.55	1.72	0.0045	0.43	0.416	3130	tags=53%, list=24%, signal=69%
KEGG METABOLISM OF XENOBIOTICS BY CYTOCHROME P450	36	0.52	1.68	0.0088	0.31	0.545	4543	tags=67%, list=35%, signal=102%
KEGG DRUG METABOLISM CYTOCHROME P450	39	0.50	1.64	0.0133	0.30	0.688	4543	tags=62%, list=35%, signal=94%
KEGG GLYCOSAMINOGLYCAN DEGRADATION	20	0.58	1.62	0.0092	0.27	0.753	1058	tags=35%, list=8%, signal=38%
KEGG PHENYLALANINE METABOLISM	16	0.59	1.59	0.0292	0.29	0.841	1846	tags=44%, list=14%, signal=51%
KEGG LYSOSOME	112	0.40	1.55	0.0041	0.34	0.925	1159	tags=18%, list=9%, signal=19%
KEGG RETINOL METABOLISM	28	0.51	1.53	0.0360	0.35	0.946	4245	tags=61%, list=32%, signal=89%
KEGG PPAR SIGNALING PATHWAY	60	0.43	1.53	0.0197	0.31	0.947	1416	tags=18%, list=11%, signal=20%
KEGG TRYPTOPHAN METABOLISM	37	0.47	1.49	0.0375	0.35	0.979	2959	tags=41%, list=22%, signal=52%
KEGG GLYCOLYSIS GLUCONEOGENESIS	54	0.42	1.49	0.0187	0.32	0.979	4222	tags=52%, list=32%, signal=76%

Table 3. Top up-regulated Gene Sets (GS)s from KEGG pathway database in isolated microglia from *Egln3 $^{-/-}$; App-Psen1 versus App-Psen1* mice

Top ten up-regulated GS from KEGG pathway database in 12-month-old isolated microglia from *Egln3* $^{-/-}$; *App-Psen1 versus App-Psen1* mice revealed by Gene Set Enrichment Analysis (GSEA).

Interestingly, the most down-regulated GS from KEGG pathway database in *Egln3* $^{-/-}$*; App-Psen1* included Nod-like, Toll-like, and Rig-I-like receptor signalling pathways (**Table 4** and **Figure 30**).

Name	Size	ES	NES	NOM p-val	FDR q-val	FWER p-val	Rank at max	Leading edge
KEGG NOD-LIKE RECEPTOR SIGNALING PATHWAY	47	-0.62	-2.34	0.000	0.00	0.001	1881	tags=49%, list=14%, signal=57%
KEGG TOLL-LIKE RECEPTOR SIGNALING PATHWAY	95	-0.54	-2.31	0.000	0.00	0.001	1858	tags=46%, list=14%, signal=54%
KEGG RIG-I-LIKE RECEPTOR SIGNALING PATHWAY	59	-0.59	-2.28	0.000	0.00	0.005	1727	tags=37%, list=13%, signal=43%
KEGG CYTOSOLIC DNA SENSING PATHWAY	47	-0.59	-2.25	0.000	0.00	0.005	1463	tags=38%, list=11%, signal=43%
KEGG B CELL RECEPTOR SIGNALING PATHWAY	71	-0.54	-2.19	0.000	0.00	0.012	968	tags=32%, list=7%, signal=35%
KEGG UBIQUITIN MEDIATED PROTEOLYSIS	123	-0.41	1.83	0.000	0.08	0.288	2658	tags=41%, list=20%, signal=50%
KEGG NEUROTROPHIN SIGNALING PATHWAY	116	-0.41	1.82	0.000	0.07	0.300	1802	tags=29%, list=14%, signal=34%
KEGG ERBB SIGNALING PATHWAY	84	-0.43	1.81	0.000	0.07	0.320	1802	tags=32%, list=14%, signal=37%
KEGG NATURAL KILLER CELL MEDIATED CYTOTOXICITY	98	-0.43	1.80	0.000	0.06	0.336	2270	tags=40%, list=17%, signal=48%
KEGG GLIOMA	59	-0.46	1.80	0.003	0.06	0.356	1817	tags=34%, list=14%, signal=39%

Table 4. Top down-regulated Gene Sets (GS)s from KEGG pathway database in isolated microglia from *Egln3* $^{-/-}$; *App-Psen1 versus App-Psen1* mice

Top ten down-regulated GS from KEGG pathway database in 12-month-old isolated microglia from *Egln3* $^{-/-}$; *App-Psen1 versus App-Psen1* mice revealed by Gene Set Enrichment Analysis (GSEA).

NOD signalling pathway is induced in innate immune cells in response to certain bacterial and viral infections (Philpott et al., 2014). On the other hand, the diversity of TLRs present in mammalian organisms serves as a mechanism to detect a number of invading pathogens, eliciting responses against bacterial and viral infections (Nicotra et al., 2012; Okun et al., 2011). However, RIG-I-like receptors essentially sense replicating viruses in the cytoplasm and can trigger antiviral activities dependent on Interferon (IFN) signalling (Kato et al., 2011). In addition,

many down-regulated genes contained in the most repressed GS related to type I interferon (IFN-I), a critical mediator of antiviral responses (Lin & Young, 2014).

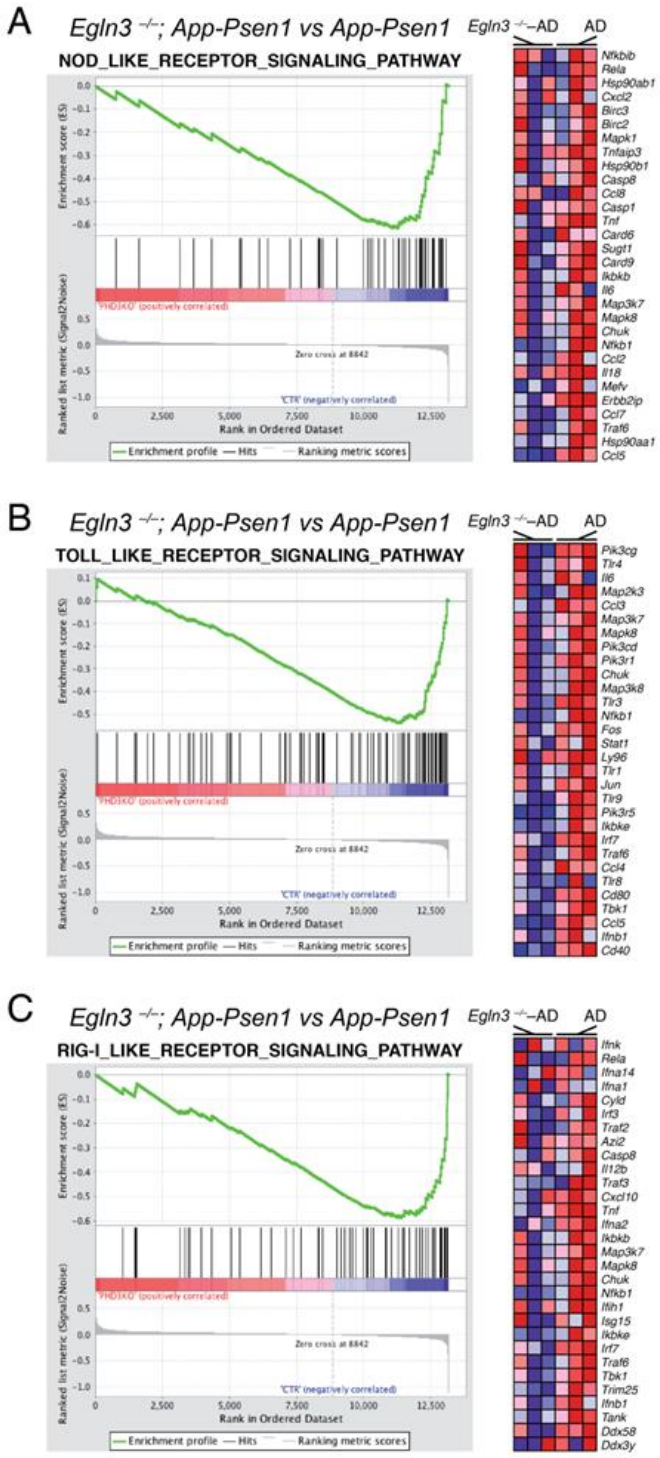

Figure 30. Prolyl-hydroxylase 3 (PHD3)-deficient microglia represses antimicrobial responses in Alzheimer's disease (AD).

(A-C) Global expression comparison between isolated microglia of 12-month-old *Egln3* $^{-/-}$; *App-Psen1 versus App-Psen1* mice by Gene Set Enrichment Analysis (GSEA). Left plots show enrichment of antimicrobial Gene Sets (GS)s, right panels show the

heat map of the top 30 ranking leading edge genes included in each GS, with red symbolizing up-regulation and blue, down-regulation. (A) GSEA showing NOD-like receptor signalling pathway enrichment. (B) GSEA showing Toll-like receptor signalling pathway enrichment. (C) GSEA showing RIG-I-like receptor signalling pathway enrichment.

This result suggests that PHD3 deficiency in AD context is limiting a microglial defense response against invading pathogens, with special emphasis in antiviral protection.

4.2.10. PHD3-deficient microglia represses an IFN-β response elicited in AD

To statistically evaluate the potential relevance of the IFN-I pathway in PHD3 deficient microglia, an IFN-β-induced signature (IβS) from macrophages was generated from a previous report (Litvak et al., 2012). GSEA revealed a strong induction of the IβS in microglial transcriptional profiles of two different AD mouse models (**Figure 31, A**) obtained from previous reports (Orre et al., 2014; Wang et al., 2015). The same approach was used to test the IβS enrichment in the isolated microglia from *Egln3* $^{-/-}$*; App-Psen1* microglia and a prominent repression of this GS was observed (**Figure 31, B**). In order to confirm this strong repression, the mRNA levels of some representative genes contained in the IFN-β signature were analyzed by qRT-PCR (**Figure 31, C**). This group of genes included *Rsad2*, *Trim30*, *Ifit2*, *Oasl1*, and *Irf7*, an orchestrator gene in the establishment of the antiviral response. Importantly, a significant reduction in the mRNA levels of *Rsad2*, *Trim30*, and *Irf7* genes was observed, concomitantly with a trend to reduce mRNA levels of *Oasl1* and *Ifit2* genes.

These findings suggest that microglia activate a potent antiviral module in AD *via* PHD3 activation.

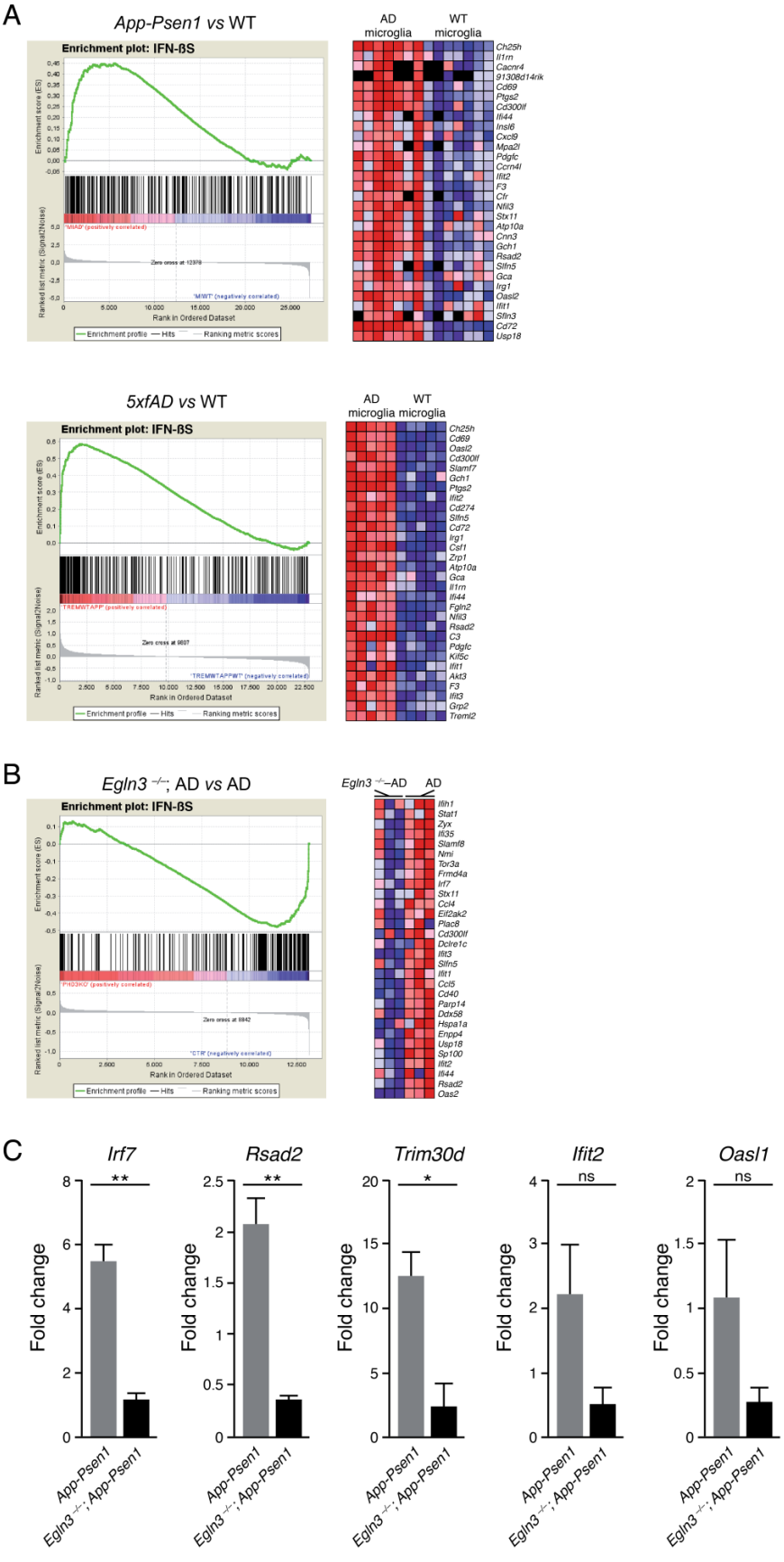

Figure 31. Alzheimer's disease (AD) microglia elicit an Interferon-β response mediated by prolyl-hydroxylase 3 (PHD3)

(A-C) Global expression comparison between isolated microglia from different groups of mice by Gene Set Enrichment Analysis (GSEA). Left plots show enrichment of Interferon-β Signature (IβS) (Litvak et al., 2012), right panels show the heat map of the top 30 ranking leading edge genes included in the IβS, with red symbolizing up-regulation and blue, down-regulation. (A) GSEA showing IβS enrichment in the comparison of 15-18-month-old *App-Psen1 versus wild-type* microglia (Orre et al., 2014) (up) and 8.5-month-old *5xfAD versus wild-type* isolated microglia (Wang et al., 2015). (B) GSEA showing IβS enrichment in the comparison of 12-month-old *Egln3* $^{-/-}$; *App-Psen1 versus App-Psen1* isolated microglia. (C) Reverse transcription real-time polymerase chain reaction (qRT-PCR) of relevant antiviral genes contained in the IβS (*Irf7, Rsad2, Trim30d, Ifit2, Oasl1*). *App-Psen1* mice, grey bar; *Egln3* $^{-/-}$; *App-Psen1* mice, black bar. * $p < 0.05$, ** $p < 0.01$; Student's *t*-test; $n = 3$ pools of 2 mice per genotype. Bars ± error bars represent mean ± s.e.m.

4.2.11. Overlapping responses in AD microglia and PHD3-deficient AD microglia suggest a potentiation of beneficial transcriptional responses for AD

Apparently, the overall gene expression modifications in *Egln3* $^{-/-}$*; App-Psen1* in comparison to *App-Psen1* microglia seemed to potentiate the microglial transcriptional profile already present in *App-Psen1* microglia, since we found that a 67 % of genes up-regulated in *Egln3* $^{-/-}$*; App-Psen1* microglia were already up-regulated in *App-Psen1* microglia (Orre et al., 2014) (**Figure 32, A**).

For the purpose of confirming our hypothesis, qRT-PCR measurements of some representative genes that are overexpressed in microglia from AD mouse models (Orre et al., 2014) were performed and a significant increase was demonstrated in the expression levels of already up-regulated genes in AD microglia like *Mamdc2* and *Cxcl14*, accompanied by a trend to increase other already up-regulated genes like *Postn* and *Dkk2* (**Figure 32, B**)

Given that our previous results showed less neurotoxicity that correlated with both motor and cognitive functional improvement, we hypothesized that PHD3 absence could be promoting beneficial functional modules in terms of AD outcome. Loss-of-function *Trem2* gene polymorphisms, a gene whose expression in virtually confined to microglia within the CNS, are among the strongest risk factors associated to sAD (Condello et al., 2017). Interestingly, microarray data generated in this thesis showed a statistically significant increment in *Trem2* mRNA levels (logFC = 0.47; $p = 0.003$) that we were not able to reproduce with qRT-PCR,

probably due to technical issues. Alternatively, gain-of-function *Cd33* gene polymorphisms, a gene involved in phagocytosis restriction, are associated with sAD (Griciuc et al., 2013). We obtained a significant reduction in *Cd33* mRNA levels from *Egln3* $^{-/-}$*; App-Psen1* microglia in comparison with *App-Psen1* microglia (**Figure 33**).

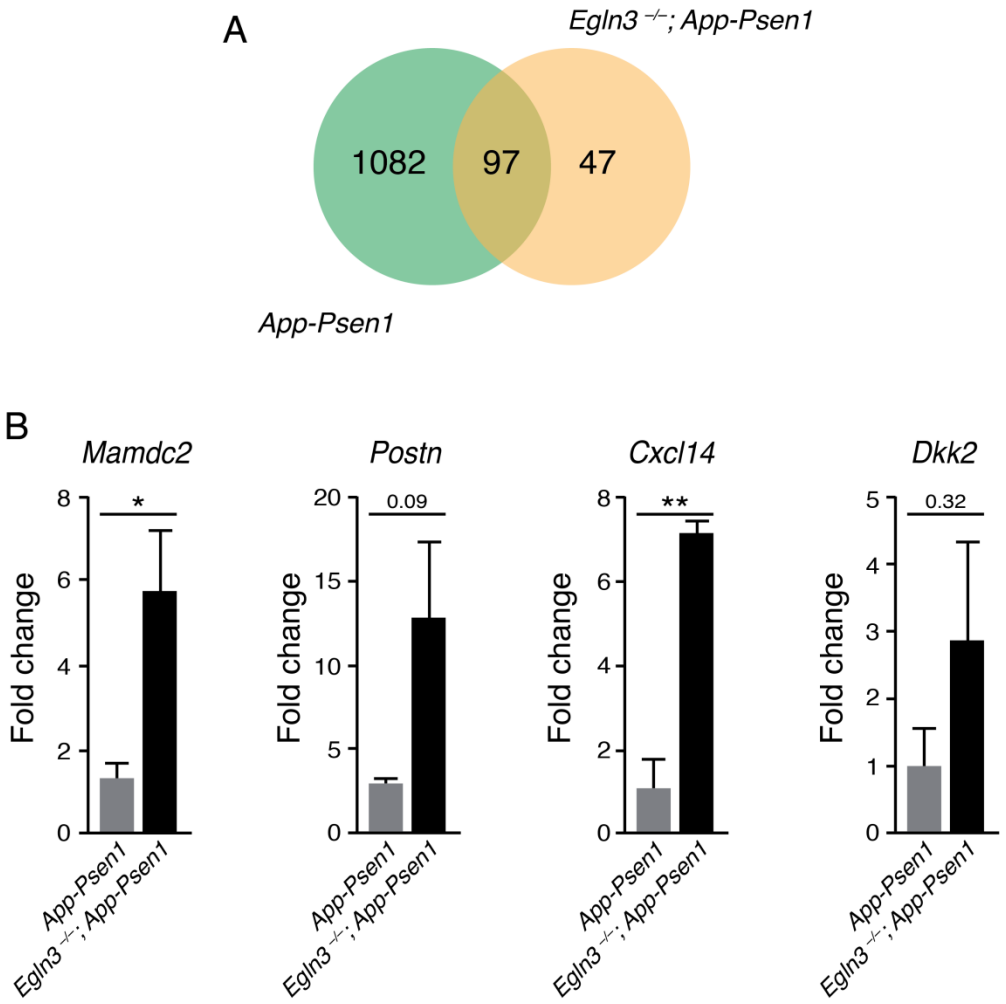

Figure 32. Prolyl-hydroxylase 3 (PHD3) absence in the microglia from Alzheimer's disease (AD) mouse models potentiates AD-related microglial responses.

(A) Venn diagram including up-regulated genes in the comparison between 15-18-month-old *App-Psen1 versus wild-type* isolated microglia (Orre et al., 2014) and up-regulated genes in the comparison between 12-month-old *Egln3* $^{-/-}$; *App-Psen1 versus App-Psen1* isolated microglia. (B) Reverse transcription real-time polymerase chain reaction (qRT-PCR) of some genes contained in the overlapping area in A (*Mamdc2, Postn, Cxcl14, Dkk2*). *App-Psen1* mice, grey bar; *Egln3* $^{-/-}$; *App-Psen1* mice, black bar. * $p < 0.05$, ** $p < 0.01$; Student's *t*-test; $n = 3$ pools of 2 mice per genotype. Bars ± error bars represent mean ± s.e.m.

These results suggest a potentiation of beneficial responses upon *Egln3* deletion in AD.

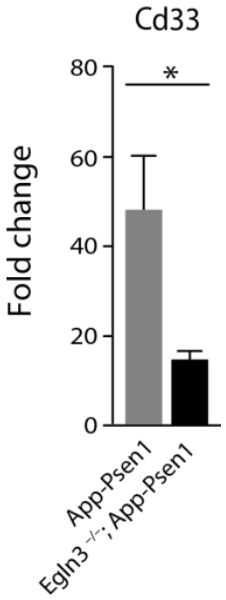

Figure 33. Microglial transcriptional changes associated to beneficial outcomes for Alzheimer's disease (AD) are observed in AD-related genetic risk factors upon prolyl-hydroxylase 3 (PHD3) deficiency.

Reverse transcription real-time polymerase chain reaction (qRT-PCR) of Cd33 gene, a genetic risk factors with loss-of-function polymorphisms associated to AD. App-Psen1 mice, grey bar; Egln3 –/–; App-Psen1 mice, black bar. * $p < 0.05$; Student's t-test; n = 3 pools of 2 mice per genotype. Bars ± error bars represent mean ± s.e.m.

5. Discussion

In order to facilitate a comprehensive and conceptual organization, the discussion is presented according to the objectives.

5.1. Objective 1: Hypoxia on AβPP processing

Our results show that neither ASH nor CSH promotes AβPP overproduction or an AβPP processing shift towards the amyloidogenic pathway, in *wild-type* C57/BI6J or *App-Psen1* mice. mRNA levels of the genes encoding for Aβ-degrading enzymes were also similar in our hypoxic paradigms *versus* normoxia. We validated our ASH approach by corroborating brain HIF1α stabilization and transcriptional induction of *Vegfa*. Our CSH protocol was also confirmed by the moderate transcriptional induction and protein accumulation of VEGF, concomitantly with an increased hematocrit load, revealing local and systemic adaptations to hypoxia. Young *wild-type* C57/BI6J mice did not show transcriptional changes in *App* gene, AβPP processing-related genes or genes encoding for Aβ-degrading enzymes either in ASH or in CSH. Neither AβPP production nor BACE1 protein levels increased in sustained hypoxic conditions in *wild-type* C57/BI6J mice. In fact, we detected a reduction in BACE1 protein levels after 16 h of ASH. Although Aβ peptides could not be quantified, an estimation of non-amyloidogenic processing of AβPP *versus* amyloidogenic AβPP proteolysis was obtained in CSH by calculating the ratio between C99 and C83 fragments and no differences were obtained. We extended our CSH approach to young and aged *App-Psen1* mice in order to test potential effects in an Aβ-accumulation scenario and no changes in AβPP or sAβPPα protein levels were detected in their brains. Importantly, we also measured by ELISA Aβ load in these mice and observed no differences either in $A\beta_{1-40}$ or $A\beta_{1-42}$ burden regarding normoxia.

Our findings are in sharp contrast with a number of previous studies in which hypoxia resulted in increased Aβ accumulation due to differences in mRNA levels and protein levels of AβPP or Aβ-related enzymes. Some studies proposed an

increment in AβPP production itself (Chen et al., 2003; Liu et al., 2016; Moussavi et al., 2012; Zhang et al., 2013) concomitantly, in some cases, with elevated transcription or protein levels of the most rate-limiting pro-amyloidogenic enzyme BACE1 (Guglielmotto et al., 2009; Liu et al., 2016; Moussavi et al., 2012; Sun et al., 2006; Zhang et al., 2007). Higher levels of the different components of ɣ-secretase complex are linked to increased Aβ production. In this sense, PS1 (Moussavi et al., 2012; Smith et al., 2004), PS2 (Moussavi et al., 2012), APH1a (Li et al., 2009; Liu et al., 2016; Wang et al., 2006), nicastrin (Liu et al., 2016) and PS enhancer 2 (Liu et al., 2016) are among the reported up-regulated components of ɣ-secretase complex in hypoxia. Inhibition or down-regulation of Aβ-degrading enzymes is an important contributor to Aβ accumulation (Fukami et al., 2002; Jha et al., 2015). Some studies have described a decrease in neprilysin enzyme, one of the most relevant Aβ-degrading enzymes, upon hypoxia treatment (Kerridge et al., 2015; Liu et al., 2016; Zhang et al., 2013).

Different hypothesis and mechanisms have emerged from these studies in order to explain the observed Aβ metabolism and phenotypic alterations in hypoxia. Most of these mechanisms are based on HIF1α stabilization under hypoxia. Moreover, HREs have been reported in promoter regions of some Aβ-related genes. Sun et al. found HIF1α binding to an HRE element upstream *Bace1* gene that activated *Bace1* expression in *in vivo* SH-SY5Y cells (Sun et al., 2006) and posterior studies have explained their augmentation in BACE1 on the basis of this HIF1α binding to *Bace1* upstream HRE (Guglielmotto et al., 2009; Zhang et al., 2007). Although we validated a HIF1α increment in our ASH protocol and *Vegfa* gene and VEGF protein up-regulation under CSH, we did not observe *Bace1* up-regulation, either at the mRNA or at the protein levels. Accordingly, other studies with AD mouse models and neuroblastoma SH-SY5Y cells also found equal levels of BACE1 protein in normoxia and hypoxia (Shiota et al., 2013) and some of them reported a decrease in ADAM10 and/or TACE proteins instead (Lee et al., 2006; Marshall et al., 2006; Webster et al., 2002, 2004), something that we did not detect in our study. A similar HRE has been found upstream of *Aph1a* gene, what would explain an increase in ɣ-secretase activity reported in hypoxia by some studies (Li et al., 2009; Wang et al., 2006), again arguing against our results. Furthermore, HIF binding regions have also been described in *Psen1* gene promoter (Bazan & Lukiw, 2002).

Importantly, HIF1α binding to HREs has been studied in cell lines in conditions where HIF is stabilized and no chromatin immunoprecipitation studies have so far demonstrated the binding of this transcription factor to Aβ-related HREs *in vitro* (Schödel et al., 2011) or *in vivo*, to our knowledge. Moreover, promoter availability might be different in diverse cell lines and so, HIF1α-induced genes vary accordingly in a cell-type and context-dependent manner (Benita et al., 2009). Alternatively, microarray data from different cell-types like MCF7 (Elvidge et al., 2006), HEK293T (Wang et al., 2005), neuronal (Felfly et al., 2011) and microglial cells (unpublished data from our lab) do not show alterations in the mRNA levels of any of Aβ-related genes. Therefore, these apparent contradictions among different studies might obey to the different experimental approaches performed.

Oxidative stress constitutes another extensively recurring mechanism to explain transcriptional and biochemical changes reported from previous studies in AβPP processing in hypoxia. Mitochondria have long been considered as a high-sensitive oxygen sensor. In response to decreased O_2 levels, mitochondria produce reactive oxygen species (ROS). Although ROS can produce molecular damage, these molecules are also associated with increased mitochondrial lifespan and to signaling cascades to promote different functional responses (Raamsdonk, 2015). In fact, it has been proposed that ROS can stabilize HIFα through inhibition of PHDs (Guzy & Schumacker, 2006), potentially leading to transcriptional activation of Aβ-related enzymes production by HIFα binding to putative upstream HREs. On the other hand, Smith et al. proposed an extra mechanism to promote ɣ-secretase activity and subsequent Aβ accumulation based on HIF1α binding to PS1 after HIF1α induced stabilization by ROS (Smith et al., 2004). However, posterior studies described an apparently HIF1α-independent positive feedback loop in which ROS activates JNK signaling that in turn induces *Bace1* and ɣ-secretase genes. Upon this induction, Aβ accumulates and provokes mitochondrial electron transport chain impairment, reinforcing ROS production (Moussavi et al., 2012; Tamagno et al., 2008). Although we did not test ROS accumulation, we did not observe alteration of the C99/C83 ratio in *wild-type* mice or $A\beta_{1\text{-}40}$ and $A\beta_{1\text{-}42}$ levels in *App-Psen1* mice submitted to CSH, strongly arguing against a hypoxia-generated ROS triggering of amyloidogenic AβPP processing or Aβ accumulation. Moreover, ROS generation in hypoxia are broadly discussed and it has been described that

hypoxia produces a short-term ROS burst (Hernansanz-Agustín et al., 2014), but hypoxia/reperfusion dynamics provokes an exacerbated ROS accumulation (Murphy & Steenbergen, 2008). Remarkably, GWAS studies have revealed that genetic modifications altering endolysosomal function, lipid metabolism or immune response are more likely to predispose to sAD but no ROS induction-related genes have emerged from these exhaustive studies, supporting a limited contribution for ROS formation in the comorbidity between hypoxia and sAD (Pimenova et al., 2018).

Apart from ROS and HIF1α accumulation-based hypothesis, other mechanisms have also been described. Among them, autophagy, caspase activation or epigenetics constitute some examples. Li et al. described an increased ɣ-secretase activity that accounted for Aβ accumulation in hypoxia due to the formation of autophagic vesicles containing ɣ-secretase complex. C99 fragments colocalized with autophagic vesicles, suggesting an altered protein trafficking that favors C99 and ɣ-secretase interaction in these vesicles, facilitating Aβ production (Li et al., 2009). It has been described that hypoxia during pregnancy has a profound impact on AD development and progression in the offspring, very likely exerted by epigenetic modifications during development (Zhang et al., 2013). In this sense, it has been reported that hypoxia down-regulates the expression of a methyltransferase called DNMT3b, resulting in up-regulation of amyloidogenic processes (Liu et al., 2016). Kerridge et al. claimed an AICD fragment implication in epigenetic processes, mediated by caspases, that decreases Aβ-degrading enzymes such as neprilysin and TTR, promoting Aβ accumulation (Kerridge et al., 2014, 2015). Since all of these mechanisms would be triggering Aβ accumulation, an effect that we did not observe with our approach, we did not explore any potential involvement of them in our paradigms. Important technical and methodological differences among studies may explain such different or even contradictory conclusions. First of all, as already mentioned, hypoxic response is highly cell-type dependent and therefore, very likely to be different between cell cultures and animal models (Harris et al., 2014; Tátrai et al., 2017). A number of studies claiming a hypoxia impact on Aβ metabolism have been performed in primary or cell lines cultures (Chen et al., 2003; Guglielmotto et al., 2009; Kerridge et al., 2015; Smith et al., 2004; Wang et al., 2006; Zhang et al., 2007), while our approach has

been integrally based on *in vivo wild-type* and AD mouse models. Nevertheless, remarkable differences are observed even when using the same model organism. For example, Lee et al. showed no significant changes in the expression or activity of BACE1 after ischemic challenge, while Sun et al. described an up-regulated BACE1 activity using the same AD transgenic mice model (Tg2576) (Lee et al., 2006; Sun et al., 2006). Consequently, other factors are implicated in this discrepancy and one of the most relevant ones is the control and proportion of hypoxic conditions.

HIF1α responses are extremely dose-dependent involving even opposing responses in the same cell-type upon different O_2 tensions. Pulmonary arterial smooth muscle cell, cancer cell, and cardiomyocyte proliferation is activated by hypoxia; however, if hypoxia exceeds a certain threshold, it leads to cell cycle arrest (Hubbi & Semenza, 2015). Therefore, a validated hypoxia treatment must be used to draw appropriate conclusions. Our ASH and CSH protocols were validated by examining both cellular (HIF1α and VEGF) and systemic (hematocrit) responses to hypoxia by using the same hypoxia chambers that we used for the subsequent experiments, in which O_2, CO_2, and humidity conditions are tightly controlled. Furthermore, our collaborators had previously confirmed no neuronal death induced by our hypoxia treatment (9 % O_2), being properly tolerated by mice. Moreover, they confirmed a pure induced hypoxemia in this hypoxia treatment, discarding off-target hypercapnia or acidosis that could affect our results (D'Anglemont de Tassigny et al., 2015). On the contrary, an array of oxygen tensions and equipment has been used in previous studies with not fine-control of hypoxia conditions in many cases. In studies using primary cell cultures or cell lines, some of them have used sealed chambers but not leak-proof (Chen et al., 2003); others performed $NiCl_2$ treatments in culture medium (Li et al., 2009; Wang et al., 2006), so possible side effects could be involved in their results. Previous studies involving animal models used semi-sealable chambers with diary reoxygenation for 16 h in some cases, so risk of O_2 perturbation is significant (Sun et al., 2006). In other cases, hypobaric chambers were used to simulate high altitude conditions (Liu et al., 2016; Zhang et al., 2013). However, this scenario can lead to hypercapnia, alkalosis, pulmonary hypertension and vasogenic edema, so side effects apart from pure hypoxemia may account for their finds (Hackett &

Roach, 2001; Wilson et al., 2009). Other methodologies involved enclosure of mice in sealed jars "until last breath gasping", a situation of absolutely not controlled O_2 or CO_2 levels and that cannot be confounded with chronic hypoxia (Gao et al., 2013; Li et al., 2009). Therefore, methodological approach and paradigm validation may not have been adequate in previous studies to study pure hypoxemia.

We designed a sustained hypoxia paradigm for two main reasons. The first one is that epidemiological studies link many different conditions that involve chronic hypoperfusion to sAD (Kalaria, 2000). Secondly, our hypoxia chambers allow as to precisely control sustained hypoxia conditions in animals, so we can attribute our results directly to the hypoxic treatment. Nevertheless, other studies reporting an increased Aβ accumulation and pathology in animal models after hypoxia have used chronic intermittent hypoxia paradigms. These approaches were based on hypoxia/renormoxia cycles consisting of from minutes to hours of hypoxia on a daily basis for up to 1 or 2 months, a scenario hardly translatable to human disease. With this approach, it is not possible to rule out the possibility that continuous hypoxia/reperfusion consequences rather than pure hypoxemia were provoking their described alterations (Gao et al., 2013; Li et al., 2009; Liu et al., 2016; Shiota et al., 2013; Sun et al., 2006; Zhang et al., 2013). In this sense, it has been reported that intermittent hypoxia is a more potent stimulus than sustained hypoxia to elicit HIF1α, *c-fos* gene, activator protein-1, NF-κB and cAMP-response-element-binding protein activation, with a number of implications for cell cultures and the full animal (Nanduri & Nanduri, 2007). Importantly, as previously said, hypoxia/reperfusion also leads to ROS accumulation (Murphy & Steenbergen, 2008). In fact, we obtained statistically significant increased levels of *App* and *Psen1* mRNA levels upon reoxygenation after ASH and CSH, although the magnitude of this changes turned them unlikely relevant for the pathology. However, we cannot discard further consequences of a greater number of hypoxia/reoxygenation cycles in our paradigm. In any case, mimicking conditions like OSA would require equipment with the capacity of dramatically changing FiO_2 following the patient's breathing dynamics (seconds), something that was not faithfully emulated by previous studies.

Finally, control conditions in previous studies using animal models are also doubtful. Chronic stress is linked to increments in Aβ levels (Jeong, 2006). On the contrary, environmental enrichment is known to reduce Aβ levels (Lazarov et al., 2005). In order to avoid any off-target results due to differential stress conditions, our control mice were exposed to normoxic conditions in the same hypoxia chamber for the same period of time.

5.2. Objective 2: PHD3 and AD microglia

We uncover a detrimental role for PHD3 activation in microglia in AD mouse models. In AD, upon PHD3 ablation, microglia numbers were unchanged but acquired a higher surface expression of CD45 protein. This CD45 enrichment was coincident with a moderate increase in *in vivo* Aβ phagocytosis that correlated with a decrease in total $A\beta_{1\text{-}42}$ peptide content. Concomitantly, neuronal dystrophies surrounding compact Aβ plaques were diminished, presumably due to the detected significant increased microglial direct interaction with Aβ plaques. Importantly, these findings resulted in rescue of motor and short-term memory alterations exhibited by AD mice. Microarray analysis of *Egln3*$^{-/-}$*; App-Psen1 versus App-Psen1* microglia revealed a selective repression of antimicrobial responses and a potentiation of the transcriptional pattern of AD microglia. Particularly, a sterile microglial IFN-β response activated in AD mouse models was strongly repressed by PHD3 absence.

Egln3 is poorly expressed by microglia according to single cell RNA-seq experiments in the *wild-type* CD-1 mouse primary somatosensory cortex (Zeisel et al., 2015). However, Aβ accumulation induces *Egln3* expression in microglia, something that we confirmed by *in situ*. Interestingly, *Egln3* mRNA transcription was almost exclusively restricted to microglia surrounding amyloid plaques, suggesting a triggering factor for *Egln3* transcription confined to plaques vicinity. In this sense, studies on atherosclerotic plaques, which are also deposits with associated macrophages, reported hypoxia and the concomitant HIF1α stabilization in surrounding cells (Marsch et al., 2013; Parathath et al., 2011; Silvola et al., 2011). Previous results in our lab demonstrated that a notable proportion of *Egln3* expression in AD microglia relies on HIF1α, that contributes to

the high HMS enrichment exhibited by microglia from aged AD mouse models (Orre et al., 2014), in which plaques burden is relatively high. On the other hand, since we have used a full *Egln3* knock-out mouse, the almost exclusive induction of *Egln3* in microglia is a supportive argument to attribute our findings to PHD3 absence in these cells. Nevertheless, a microglial-specific conditional knock-out mouse should be used in order to discard off-target effects due to deletion in other *Egln3*-expressing cells.

The virtually absent expression of *Egln3* gene in microglia not associated to amyloid plaques might explain the coincident results observed in *wild-type* and *Egln3* $^{-/-}$ microglia regarding the same proportion and expression surface markers CD11b and CD45. As extensively described in the literature, microglia proliferate in Aβ accumulation mouse models (Kamphuis et al., 2012; Olmos-Alonso et al., 2016), although microglia numbers do not seem to rise in AD patients (Serrano-Pozo, Gómez-Isla, et al., 2013). We quantified the proportion of cortical microglia from *App-Psen1* and *Egln3* $^{-/-}$*; App-Psen1* mice and found a similar significant increase in both genotypes with respects to the control group, suggesting that PHD3 absence is not limiting proliferative capacity of AD microglia. We further confirmed the same microglial cell number per cortical area by stereological cell counting with IBA1, a different microglial marker broadly used. Involvement of PHD3 in survival of innate immune cells shows cell-type specificity. PHD3 exerts a pro-survival effect in neutrophils that results in delayed inflammatory resolution (Walmsley et al., 2011). However, PHD3 induction acts as a pro-apoptotic signal for mouse serum-starved cultured macrophages (Swain et al., 2014). Our results suggest that, in an AD model, PHD3 induction does not activate a pro-apoptotic microglial phenotype, as we did not detect any changes in cell number associated with PHD3 deficiency. However, specific experimental approaches would be needed to demonstrate this hypothesis.

Peripheral monocytes infiltration within the brain can occur under certain circumstances in which blood-brain barrier is impaired, where they differentiate into MDM (Nayak et al., 2014) However, parabiosis experiments showed minimal contribution of infiltrating monocytes in AD brains, being microglia responsible for the increased macrophage cell number (Wang et al., 2016). MDM usually express

high CD45 levels in their surface (Campanella et al., 2002; Denker et al., 2007) and we found that *Egln3*$^{-/-}$*; App-Psen1* microglia displayed an increased CD45 surface expression marker regarding *App-Psen1* microglia. Although it has been described that under steady-state and degenerative conditions brain macrophage number increases upon microglial precursors proliferation (Nayak et al., 2014), it could be possible that PHD3 absence facilitated the entry of monocytes to the brain parenchyma. Therefore, high CD45-expressing events would belong to MDM instead of a phenotypically different resident microglia. We ruled out this possibility for two main reasons. First of all, we had the same microglial proportion and number in *App-Psen1* and *Egln3* $^{-/-}$*; App-Psen1*, according to flow cytometry and stereological experiments. Hence, an entry of monocytes from the bloodstream without altering total proportions would necessarily involve a proportional microglial death or proliferation arrest, something even more unlikely to happen if we consider the potential inhibition of apoptosis due to the lack of PHD3 in macrophages, as previously described (Swain et al., 2014). Secondly, the differentially expressed genes between microglia from *Egln3* $^{-/-}$*; App-Psen1* and *App-Psen1* mice did not reveal any increase in macrophage or decrease in microglia markers, something that should be expected if microglia were being replaced by MDM (Hickman et al., 2013).

We also analyzed *in vivo* Aβ phagocytic capacity of microglia in *Egln3* $^{-/-}$*; App-Psen1* and *App-Psen1* mice. We observed a modest increase in the proportion of phagocytic microglia in *Egln3* $^{-/-}$*; App-Psen1 versus App-Psen1* mice. Our results are consistent with previous studies relating CD45 increase with enhanced phagocytic skills in microglia. For instance, Zhu et al. used primary microglial cultures treated with agonistic CD45 antibodies and found an enhanced Aβ phagocytic activity. By contrast, loss of CD45 resulted in a pro-inflammatory phenotype with unexpected decreased Aβ phagocytic ability (Zhu et al., 2011). On the other hand, a different approach was used to study CD45 involvement in microglia phagocytosis. Rangaraju et al. isolated CD11b^{+} CD45^{low} separately from CD11b^{+} CD45^{high} microglia from 5xfAD mouse models, an aggressive Aβ accumulation transgenic mouse model, by FACS. Next, they assessed phagocytosis of fA$\beta_{1\text{-}42}$ of the acute *ex vivo* isolated microglia and described an increased phagocytic activity in CD45^{high} microglia (Rangaraju et al., 2018). The increased phagocytosis observed in *Egln3* $^{-}$

$^{-/-}$*; App-Psen1* microglia is in fair agreement with the detected decrease in *Cd33* mRNA levels that we confirmed in these microglia regarding *App-Psen1* microglia, since CD33 has been described as a blocker of phagocytosis for these cells (Griciuc et al., 2013). On the order hand, we hypothesize that the increased proximity of microglia to Aβ plaques detected in *Egln3* $^{-/-}$*; App-Psen1* mice could also favor Aβ phagocytosis because of their closer interaction with these Aβ reservoirs, as already suggested (Wang et al., 2015). Presumably, an increment in the number of individuals for phagocytosis experiments would provide enough statistical power to raise significant differences, given the strong trend observed.

An increased phagocytic capacity could potentially correspond to diminished Aβ levels, which associate with a good prognosis for AD (Rangaraju et al., 2018). We measured total $A\beta_{1\text{-}40}$ and $A\beta_{1\text{-}42}$ content in mouse cortices by ELISA and we obtained a modest decrease in $A\beta_{1\text{-}40}$ and a significant decrease in $A\beta_{1\text{-}42}$ in cortical extracts from *Egln3* $^{-/-}$*; App-Psen1 versus App-Psen1* mice. This decrease in total Aβ content might be due to the observed elevated phagocytic activity in *Egln3* $^{-/-}$*; App-Psen1.* However, other factors could also be playing a role in Aβ content decrease. For instance, experiments performed with cultured adult mouse astrocytes demonstrated an Aβ-degrading activity for these cells that could be mediated by extracellular degradation, since these cells produce Aβ-degrading enzymes, or intracellularly, given that astrocytes are capable of engulf Aβ and attempt to perform lysosomal degradation in AD patients (Birch, 2014; Funato et al., 1998; Wyss-Coray et al., 2003). Nevertheless, a direct impact of PHD3 absence in astrocytes is unexpected since *Egln3* is not induced in astrocytes in AD mouse models (Orre et al., 2014), although we cannot discard an indirect effect on astrocyte-mediated Aβ degradation by *Egln3* microglial deletion. Microglia are also a source of Aβ-degrading enzymes (Tarasoff-Conway et al., 2015). Although our microarray data did not show up-regulated expression of genes of some of the main Aβ-degrading enzymes like neprilysin or IDE enzyme in *Egln3* $^{-/-}$*; App-Psen1* microglia, we cannot discard other mechanisms influencing the activity, amount or localization of these enzymes in which PHD3 could be involved. Finally, clearance of Aβ across the blood-brain barrier constitutes one of the main Aβ drainage systems from the brain (Tarasoff-Conway et al., 2015) and we have not explored a

possible involvement of PHD3 deficiency in Aβ efflux from the brain, either by direct or indirect consequences of *Egln3* microglial.

Unexpectedly, we detected a statistically significant increase in soluble $A\beta_{1-40}$ and a trend to increase soluble $A\beta_{1-42}$ in *Egln3* $^{-/-}$*; App-Psen1* regarding *App-Psen1* mice. Both the diminished neuronal damage surrounding amyloid plaques that we detected and, above all, the rescue of the motor and memory-related symptoms are in sharp contrast with a growing body of evidence that attributes significant neurotoxic functions to soluble Aβ oligomers. In fact, cognitive deficit and synaptic loss have been shown to correlate more accurately with soluble Aβ oligomers than with amyloid plaques load (Finder & Glockshuber, 2007; Haass & Selkoe, 2007; Walsh & Selkoe, 2007). However, two important aspects deserve to be considered in order to interpret our result. Firstly, the magnitude of soluble Aβ increase is relatively small, so its pathogenic significance remains unclear. Secondly, the soluble Aβ concentrations measured in the samples were very close to the detection limits of the used technique, so reliability of this data is uncertain. In any case, it is important to remark that the soluble concentration of Aβ detected constitutes a derisory contribution to the reliable, in technical terms, detected decrease in total $A\beta_{1-42}$ concentration in *Egln3* $^{-/-}$*; App-Psen1* regarding *App-Psen1* mice, reportedly the most toxic Aβ peptide fragment (Mattson et al., 1992; Selkoe, 2001). Moreover, the soluble Aβ fraction is composed by different Aβ populations in several oligomerization stages, which exhibit different potential toxicity (Finder & Glockshuber, 2007). Thus, it could be possible that oligomerization states of Aβ in the soluble fraction of *Egln3* $^{-/-}$*; App-Psen1* mice are less neurotoxic than the oligomerization states in *App-Psen1* mice.

PHD3 deficiency resulted in modification of amyloid plaque parameters. *Egln3* $^{-/-}$*; App-Psen1* mice exhibited increased proportion of dense-core amyloid plaques due to an elevated number of small compact plaques. Concomitantly, a significant increase in fAβ plaques burden was observed in these mice. Although Aβ accumulation is accepted to constitute the initial event leading to the downstream effects that culminate in AD (Hardy & Higgins, 1992), a poor correlation is found between plaques burden and the disease progression (Serrano-Pozo et al., 2011). In fact, it has even been proposed that amyloid plaques could contribute to

inactivation and nucleation of more neurotoxic Aβ species, potentially reducing neuronal damage (Finder & Glockshuber, 2007). On the other hand, our burden measurements are not recapitulating the total Aβ content measurements. While we observed a significant decrease in $A\beta_{1-42}$ concentration and a strong trend to diminish $A\beta_{1-40}$ concentration in *Egln3* $^{-/-}$*; App-Psen1* regarding *App-Psen1* mice, we obtained an increased occupied burden by fAβ conformations and a trend to elevated dense-core amyloid burden. The natural explanation for these results would involve a less dense conformation in amyloid deposits of *Egln3* $^{-/-}$*; App-Psen1* mice. Even though a closer interaction between microglia and amyloid plaques is hypothetically promoting plaque compaction (Yuan et al., 2016), we did not see enhanced plaque compaction activity on the fAβ halo upon closer interaction of microglia with big compact amyloid plaques, in which neuronal dystrophies were quantified. Therefore, it could be possible that, considering the high aggregation properties of $A\beta_{1-40}$ and $A\beta_{1-42}$ peptides and their higher concentrations in *App-Psen1* mice, *App-Psen1* mice's amyloid plaques contain more Aβ load than *Egln3* $^{-/-}$*; App-Psen1* mice's plaques, something that we could not capture in our immunostaining quantifications since we did not quantify fluorescence intensity but occupied area. Whether the microglia promoted somehow the formation of the small amyloid plaques in *Egln3* $^{-/-}$*; App-Psen1* is unknown, but we speculate that the closer proximity of microglia with amyloid plaques could be related. In any case, a deeper study on the different properties of amyloid deposits from *App-Psen1* and *Egln3* $^{-/-}$*; App-Psen1* and their microglia compaction activity would be needed to fully explain our results.

We observed an increased microglia proximity to amyloid plaques in *Egln3* $^{-/-}$*; App-Psen1 versus App-Psen1* mice. A greater microglia proximity to amyloid plaques entails an improved microglia chemotactic and migratory capacity and some of our results are consistent with this hypothesis. Firstly, microglia from CD45 *Egln3* $^{-/-}$*; App-Psen1* mice displayed enriched CD45 protein and it has been described that *CD45* knock-out MDM exhibit disrupted adhesion and motility (St-Pierre & Ostergaard, 2013). Hypothetically, CD45 overexpression might potentially lead to increased motile ability. Secondly, one of the most prominent described genes regulating microglial migration towards Aβ plaques is *Trem2*. *Trem2* mutations constitute one of the strongest genetic risk factors that predispose to AD

and its deficiency directly impairs microglial migration, clustering and activation around amyloid plaques (Wang et al., 2015). Interestingly, we observed an increase in *Trem2* mRNA by microarray analysis. Moreover, other up-regulated genes, according to microarray data, could be promoting microglial migration. In this regard, genes encoding for chemotactic receptors were significantly induced in the microglia from *Egln3* $^{-/-}$*; App-Psen1 versus App-Psen1*. Among them, *Plxna2* and *Plxnc1* genes encode for Semaphorin receptors. Semaphorins are extracellular or secreted proteins that regulate different aspects of the nervous system, like axon guidance, and immune system response *via* signaling through Plexin receptors (Worzfeld & Offermanns, 2014). In hypoxic tumor areas, macrophages migration is regulated by the chemoattractant activity of Sema3A, that promotes macrophage motility and trapping *via* Nrp1 and PlexinA1/PlexinA4 binding (Casazza et al., 2013). Moreover, *Egln3* $^{-/-}$*; App-Psen1* microglia also up-regulated the expression of *Ccr2*, a well-characterized chemoreceptor that participates in the migration of immune cells (Liu et al., 2014). In spite of the overexpression of these genes, production of the ligands for their encoded receptors should be verified in plaques vicinity in order to establish a likely implication in PHD3 deficient AD microglia enhanced migration.

The increased microglia proximity to amyloid plaques correlated with a reduction in neuronal dystrophies surrounding amyloid plaques. fAβ has been associated to increased neurotoxicity and its compaction can be mediated by direct interaction with microglial processes (Condello et al., 2015; Yuan et al., 2016). We estimated the size of the fAβ halo surrounding amyloid plaques with the same features than the ones used for neuronal dystrophies quantification and it remained unchanged. This result discards a microglia protective effect on plaques surrounding neurons based on modification of plaques conformation. On the other hand, microglia can act as a physical barrier to prevent neuronal contact with amyloid plaques (Yuan et al., 2016). We speculate that microglial insulation of amyloid plaques, potentially enhanced by increased microglia proximity, could account for the decreased neuronal damage observed in *Egln3* $^{-/-}$*; App-Psen1* mice. In fact, the increased clustered microglia burden in the cortex of *Egln3*$^{-/-}$*; App-Psen1* with respects to *App-Psen1* mice, without changes in microglia number, suggests a more extensive microglial coverage of plaques vicinity. Moreover, we discarded a contribution of

morphological changes in non-clustered microglia to the increased calculated burden, since their morphology remained unaltered, something consistent with the low mRNA levels of *Egln3* in these cells in *App-Psen1* mice that we obtained by *in situ* hybridization. Furthermore, morphological alterations in clustered microglia that increase their plaque coverage could also be implicated, since *Egln3* $^{-/-}$*; App-Psen1* microglia exhibit more CD45 protein load and CD45 has been linked to morphological changes in macrophages (St-Pierre & Ostergaard, 2013). In any case, the precise protective mechanism and whether it relies directly on microglial barrier effect remains unclear.

Behavioural experiments aimed to test motor and short-term memory assessment of control mice, *App-Psen1* and *Egln3* $^{-/-}$*; App-Psen1* revealed a protection of AD-related impairment. However, we cannot confirm whether it is due to a delay of behavioural symptoms occurrence or a complete prevention. On the other hand, microglial conditional knock-out *Egln3* mice should be used to confirm whether these results rely exclusively on microglia *Egln3* deletion or if they could be due to *Egln3* deficiency in other cell types. Moreover, whether PHD3 absence would exert beneficial effects once the disease is developed is an open question. Furthermore, we could not confirm a synaptic defect and subsequent rescue of AD upon PHD3 deficiency. In spite of that, the fact that we did not detect a decrease in synaptic proteins could obey to compensatory mechanisms consisting in enlargement of remaining synapses, keeping a constant load of synaptic markers. Thus, an existing decline in the number of synapses might not be detected by measuring synaptic proteins load, so a more detailed imaging approach would be needed to ascertain synaptic changes. Hence, mechanistic insights linking histological and behavioural phenotypes are lacking.

We analyzed the microarray data of isolated microglia of from *App-Psen1* and *Egln3* $^{-/-}$*; App-Psen1* mice in order to identify the molecular mechanisms that explain the microglial phenotype observed upon PHD3 absence. As PHD3 if a well-known HIF1α prolyl-hydroxylase, we expected a further increase in HMS elicited mediated by increased HIF1α stabilization in *Egln3* $^{-/-}$*; App-Psen1*. We did not observe either higher levels of HIF1α protein or over-expression of the HMS in *Egln3* $^{-/-}$*; App-Psen1 versus App-Psen1* microglia. We did not observe any clues

about elicited compensatory mechanisms to reduce HIF1α stabilization either. In this regard, we did not obtain transcriptional changes in *Egln1, Egln2, Epas1* or *Arnt* genes in microarray data, although a significant low-magnitude change was detected for *Arnt2* gene. This is in agreement with myeloid specific *Egln3* knock-out MDM in which no compensatory induction of other PHDs and HIF1α or HIF2α levels remained unaltered (Swain et al., 2014). By contrast, Kiss et al. found enhanced HIF1α stabilization, but not HIF2α, in macrophages subjected to LPS treatment in the absence of PHD3 (Kiss et al., 2012). Therefore, compensatory mechanisms might be promoted in a context-dependent manner. On the other hand, this absence of compensatory mechanisms suggests additional functions for PHD3 in AD microglia. In this sense, PHD3 has been suggested to have non-HIF targets and downstream effectors and even non-catalytic effects have been attributed to PHD3 (Jaakkola & Rantanen, 2013; Rodriguez et al., 2016; Walmsley et al., 2011).

A complex metabolic readjustment was manifested *Egln3* $^{-/-}$*; App-Psen1 versus App-Psen1* microglia from GSEA analysis using "KEGG pathway database". Even though we did not go deeper into metabolic regulation due to PHD3 deficiency, it has broadly been described the close interaction between metabolic status and immune response (Ganeshan & Chawla, 2014; Osborn & Olefsky, 2012) so further analysis could be worthwhile. Notable enough was the prominent repression of antimicrobial modules in general and IFN-β response in particular, in *Egln3* $^{-/-}$*; App-Psen1* microglia. Interestingly, IFN-β response has been described upon HIF1α stabilization (Hwang et al., 2006). Conversely, a potentiation of other AD-microglial transcriptional responses was observed in *Egln3* $^{-/-}$*; App-Psen1* microglia. In spite of the fact that PHD3 had not previously been associated with antimicrobial responses, it was induced in macrophages from patients suffering from ulcerative colitis or Crohn's disease (Escribese et al., 2012). Interestingly, the absence of PHD3 has been associated with clinical improvement in mouse models of ulcerative colitis and acute lung injury, through HIF-independent mechanisms (Walmsley et al., 2011), but with worse outcome in a HIF1α-dependent manner in a sepsis mouse model (Kiss et al., 2012). We hypothesize that microglial fitness has not been under selective pressure to confront pathological Aβ accumulation since it is an aging-associated event that takes place after fertile age has culminated.

Microglia, as immune cells, are equipped with an arsenal of receptors (Hickman et al., 2013), many of which are activated by Aβ (Lucin & Wyss-Coray, 2009). We propose that the IFN-β-related response activated by the HIF1α-PHD3 pathway in AD microglia is maladaptive, inducing the activation of microglial cells against a non-real threat, like viruses or bacteria. Similar "sterile" (in the absence of pathogen) activation of immune cells has been observed in the peripheral immune system and can be pathogenic (Rock et al., 2010). Silencing of this "sterile" response could favor beneficial modules, like CD33 decrease to promote Aβ phagocytosis. Our results also indicate that the reduction of the anti-microorganism modules observed in AD microglia by PHD3 deficiency allows a better microglial response to the pathology, strongly suggesting that specific pathways can be modulated in microglia to optimize biological responses to AD.

6. Conclusions

1. Both ASH and CSH protocols used in this study promote a cellular and systemic hypoxic response in mice.
2. Neither ASH nor CSH significantly impact on the mRNA levels of *App*, α-secretase (*Adam9, Adam10,* and *Adam17/TACE*), β-secretase (*Bace1*), ɣ-secretase (*Psen1, Psen2, Ncstn, Pen2, Aph1a,* and *Aph1b-c*), and Aβ-degrading enzymes (*Bace2, Ide*, and *Mme*) genes in *wild-type* mice.
3. A reoxygenation cycle after sustained hypoxia protocols increases the mRNA levels of *Psen1* gene, after ASH, and *App* gene, after CSH, without altering mRNA levels of the rest of Aβ-related enzymes.
4. *Wild-type* mice under ASH or CHS do not modify protein levels of BACE1 or AβPP as well as C99/C83 ratio in CSH, discarding a pro-amyloidogenic shift of AβPP processing.
5. CSH in 8-month-old and 14-month-old *App-Psen1* mice does not alter protein levels of FL-AβPP, sAβPPα, $A\beta_{1-40}$ and $A\beta_{1-42}$, so a pro-amyloidogenic shift of AβPP processing is not promoted.
6. *Egln3* mRNA expression in microglia of *App-Psen1* mice is specifically induced in amyloid plaques vicinity.
7. PHD3 deficiency in *App-Psen1* mice does not affect microglia proliferation whereas increases CD45 protein load and microglial Aβ phagocytic capacity, what associates with decreased total $A\beta_{1-42}$ content but elevated number of small compact plaques and fAβ cortical coverage.
8. An increased microglia proximity to amyloid plaques correlates with decreased neuronal dystrophies in plaques vicinity and motor and memory defects in *App-Psen1* mice upon PHD3 absence.
9. Microarray data from PHD3 deficient microglia reveals a repression of anti-microbial responses elicited in *App-Psen1* microglia that correlates with a

potentiation of functional modules associated with beneficial outcomes for AD.

10. Hypoxia does not affect Aβ-related genes or AβPP processing by-products but can induce the activation of HIF target genes, like *Egln3*, whose expression entails detrimental outcomes for AD.

7. Materials and methods

7.1. Mice models, housing and handling

Mice were housed under controlled temperature (22 °C) and humidity (55 %) conditions in a 12 h light/dark cycle with *ad libitum* access to food and water. Housing and treatments were performed according to the animal care guidelines of European Community Council (86/60/EEC). The Animal Research Committee at the Hospital Universitario Virgen del Rocío approved all procedures. Experimental groups were homogenously distributed by sex and assigned to each experiment without previous observation of the mice by the experimenter. No randomization methods were employed. Mice were euthanized intraperitoneally by administration of 200 mg/Kg of sodium thiopental (Braun) at 5 % (m/v) in saline solution (Fresenius Kabi España S. A.). When sublethally anesthetized, a 150 mg/kg dosage of the same solution was used.

Mice of Objective 1 were sacrifice and their samples were obtained as described below. Mice of Objective 2 destined to ELISA, WB or immunostaining were euthanized and subjected to intracardiac perfusion of 30 mL of phosphate-buffered saline (PBS) to promote blood drainage. Whole brains were extracted from skulls and subsequently divided into two hemibrains. One of them was dissected to obtain cortical and hippocampal samples for ELISA and WB experiments. The remaining one was fixed over night for posterior immunostaining techniques in 4 % paraformaldehyde (Sigma) in PBS (m/v), pH 7.4.

7.1.1. Mouse models for Objective 1: Hypoxia on AβPP processing

Heterozygous B6.Cg-Tg(APPswe,PSEN1Δ9E)85Dbo/J (*App-Psen1*; stock number 005864) was obtained from Jackson Laboratories. This transgenic mouse was generated by genomic insertion in the same locus of two genetic constructions harboring fAD mutations, whose transcription is restricted to the CNS because of

being under the control of prion protein promoter (Jankowsky et al., 2001). One of these genetic constructions consists of human *Psen1* gene with a mutation that involves loss of exon 9 in *Psen1* mRNA during splicing, resulting in a PS1 version that promotes $A\beta_{1-42}$ production (Jankowsky et al., 2004). The other genetic construction is a chimeric version of the mouse *App* gene carrying two base pair transversions found in human fAD plus the human Aβ sequence, which replaces the mouse one within this *App* chimera. The resulting AβPP protein exhibits the substitution of a lysine for an asparagine and a methionine for a leucine (K594N/M595L) preceding the Aβ fragment, what turns it more prone to amyloidogenic processing (Haass et al., 1995). This animal model exhibits early amyloid deposition, with senile plaques detectable from 4-6 months old and modest neuronal loss surrounding plaques from 9 months old, although NTFs have not been reported. Therefore, it is considered as an appropriate AD mouse model to explore pathological and biochemical aspects related to Aβ deposition (Garcia-Alloza et al., 2006; Jackson et al., 2016)

Wild-type mice were obtained by crossing C57/Bl6J mice with *App-Psen1* mice.

7.1.2. Mouse models for Objective 2: PHD3 and AD microglia

Egln3 $^{-/-}$ (Bishop et al., 2008) mouse was a generous gift from Prof. Peter J. Ratcliffe. It was generated by introducing a neomycin resistance cassette within exon 1 of *Egln3* gene. *Wild-type, Egln3* $^{-/-}$*, App-Psen1* and *Egln3* $^{-/-}$*; App-Psen1* littermates were obtained by successive crosses among *Egln3* $^{-/-}$ and *App-Psen1* mice and resulting offspring.

7.2. Mouse genotyping

Mice biopsies were incubated with 75 µL of "Solution A" (NaOH 25 mM, EDTA 0.2 mM, in ultrapure H_2O) for 30 min at 98 ºC in a Thermomixer (Eppendorf) at 450 rpm in order to digest mice tissues and extract DNA. Then, 75 µL of "Solution B" (Tris-HCl 40 mM pH 5, in ultrapure H_2O) were added and vortexed to stop "Solution A" reaction.

Polymerase Chain Reaction (PCR) in a Thermocycler (Biometra Professional Trio) was performed with oligonucleotides collected in **Table 6,** following the programs

detailed in **Table 7.** Polymerase reaction was prepared in a final volume of 25 µL containing 5 µL NH_4 10x (Bioline), 2.5 mM MgCl2 (Bioline), 1 mM of each deoxyribonucleotide (dNTP, Invitrogen), 0.66 µM of *forward* primer (Sigma), 0.66 µM of *reverse* primer (Sigma), 5 µL of extracted DNA, 1.5 U of DNA polymerase enzyme (BIOTAQ™, Bioline) and fill up to 25 µL with sterilized distilled H_2O (dH_2O).

PCR	Forward primer sequence (5'→ 3')	Reverse primer sequence (5'→ 3')
Wild-type Egln3	GAGCACCCTTATAAAAAGCAAGTGA	TGCAGAAACACCCCAGATGA
***Egln3* Knock-out**	GGAAAAGCGCCTCCCCTA	GGTTATTTAGTGCAGAAACACCCC
App-Psen1	CTTGTAAGTTGGATTCTCTATATCCG	GACTGACCACTCGACCAGGTTCTG

Table 6. Primers used for genotyping.
Primers used for mice genotyping by polymerase chain reaction (PCR).

PCR	*Wild-type Egln3*		*Egln3* Knock-out		*App-Psen1* insertion	
Phases	**Temp.**	**Time**	**Temp.**	**Time**	**Temp.**	**Time**
DNA denaturation	94 °C	2 min	94 °C	2 min	94 °C	2 min
Amplification	94 °C	30 s	94 °C	30 s	94 °C	30 s
(41 cycles for both *Egln3* and	65 °C	30 s	65 °C	30 s	65 °C	30 s
36 cycles for *App-Psen1*)	72 °C	1 min	72 °C	1 min	72 °C	1 min
Final elongation	72 °C	10 min	72 °C	10 min	72 °C	10 min
Storage	4 °C	Pause	4 °C	Pause	4 °C	Pause
Amplicon size (Kb)	300		250		350	

Table 7. Polymerase chain reaction (PCR) conditions.
PCR conditions for the different genetic sequences using the primers from table 7.

Size of PCR products was tested by agarose gel electrophoresis. Briefly, 2.5 µL of loading buffer (bromophenol blue 0.25 % v/v, xylene-cyanol FF 0.25 %, glycerol 30 %) were added to each sample prior to loading 25 µL of each of them into 2.5 % agarose gel prepared in TBE buffer (Tris-base 0.09 M, boric acid 0.0899 M, EDTA 2 mM) and supplemented with 4 % Midori Green Advance™ (Nippon Genetics). PCR products were observed under UV light after migration.

7.3. Hypoxia treatment and hematocrit measurement

Mice were exposed to a 9 % O_2 environment by using a hermetic chamber specially designed for hypoxia studies in animals (Coy Laboratory Products, Inc., Grass Lake, MI). This chamber is equipped with O_2 and CO_2 controllers and temperature and

humidity monitoring. A pump connected with the humidity and CO_2 controllers mobilizes the air within the chamber and enables to regulate these parameters. O_2 levels were monitored every other day and only ±0.5 % differences were considered acceptable. CO_2 within the chamber was kept at a minimum (< 0.1 %) by filtering the air through a sodasorb (Grace) filter. Humidity was maintained below 70 % at all times by filtering the air through a silica gel (Panreac) filter. Access into the chamber to feed the mice and clean their cages was achieved without altering the experimental conditions through glove ports and an airlock (transfer chamber). Light/dark, feeding, and cleaning cycles were kept uniform for all groups.

2-3-month-old wild-type mice were exposed to either ASH (9 % O_2, 4 to 16 h), followed or not by subsequent 24 h of reoxygenation, or CSH (9 % O_2 uninterrupted for 21 or 30 d), with or without subsequent reoxygenation for 24 h. 8 and 14-month-old *App-Psen1* mice were exposed to CSH (9 % O_2, 21 d) without reoxygenation.

Littermate *wild-type* and *App-Psen1* "normoxic" control mice of the same ages as above were also exposed to the same chamber for the same period of time, but under a 21% O_2 environment.

Animals were euthanized within the hypoxia chamber in order to minimize potential reoxygenation effects after the ASH and CSH protocols. Brains were extracted within the hypoxia chamber, snap frozen in liquid nitrogen, and stored at -80 °C for later use -qRT-PCR, WB, and ELISA-.

Hematocrit was measured in 14-month-old *App-Psen1* mice subjected to CSH (21 d, 9 % O_2, n = 4) or normoxia (21 d, 21 % O_2, n = 4). Mice were sublethally anesthetized straight after taking them out of the chamber. After dissection of abdominal and thoracic skin, the hearth was exposed by thoracic cage removal. Blood from right atrium after a small incision was collected in capillaries for subsequent centrifugation at 5000 rpm for 5 min to isolate the granular component of the blood from the plasma (P Selecta Centrolit II). Hematocrit was calculated as the ratio of the length of the granular part, measured with a ruler, divided by the total length occupied by blood in the capillaries and multiplied by 100.

7.4. RNA extraction and qRT-PCR

7.4.1. Objective 1: Hypoxia on AβPP processing

Whole hemibrain samples of 2-3-month-old *wild-type* mice per group (n = 4) were digested with a tissue homogenizer (Omni TH) in the presence of TRIzol (Life technologies), following manufacturer's instructions to obtain RNA. RNA samples (0.5 µg) were treated with RNAase-free DNAse treatment (GE Healthcare) and subsequently retro-transcribed to cDNA with SuperScriptII reverse transcriptase (Invitrogen) in a final volume of 20 µL. ABI Prism 7500 Sequence Detection System (Applied Biosystems) using Power SYBR-Green PCR Master Mix (Applied-Biosystems) was used to perform the qRT-PCR. Normalization of results by input cDNA amount was performed by including a real time PCR for *18S* mRNA in each plate. ΔΔCt method was used for quantification (Livak & Schmittgen, 2001; Nolan et al., 2006). Primer sequences used are listed in **Table 8**.

Gene	Forward primer sequence (5' → 3')	Reverse primer sequence (5' → 3')
App	CAAAGAGACATGCAGCGAGAAG	AGCATGCCATAGTCGTGCAA
Adam9	GTGCATATGGCGACTGTTGTAAA	ATGGAGCCTCCTGGAAGGAA
Adam10	GTTGCCGCCTCCTAAACCA	GGCGGTCTCCTCCTCTTTAAAG
Adam17/TACE	AACAACGACACCTGCTGCAATA	CTGCACACCCGGCTTCAG
Bace1	CAATCAGTCCTTCCGCATCAC	ACCGGCCGTAGGTATTGCT
Bace2	TTTGGTATCTCCTCTTCCACAAATG	CATCACGGTCGCACCAATC
Aph1a	CCTTCTACAGGAAGTGTTCCGTTT	TCTGCCTTCTTAAGGAGCTTGTAGT
Aph1b-c	GCGACTGTTGGCCTATGTTTCT	CACTCCACTCATGATTCCAAAGC
Psen1	CTCATGGCCCTGGTATTTATCAA	GAGCCATGCGGTCCATTC
Psen2	GCGAAACGTGTGATCATGCTAT	CACGATCATACACAGCGTGACA
Ncstn	CAAGCAGTGCTATCAAGATCACAA	CTTGGTGCAGAGCCATTCTG
Pen2	AGTTGAACCTGTGCCGGAAGT	AAGGCAGGAACGCAAATCC
Ide	GAGGTGAACGCTGTCGATTCA	GGCATCGTTCATCACATTCTTCT
Mme	ATTAAGTCTGTCCCTAGTGGCTAAGAA	GCAACACAGATACAGTTAGACCCTTTC
Irf7	GAAGACCCTGATCCTGGTGAAG	GAAGACCCTGATCCTGGTGAAG
Rsad2	CTGATTGGCCGTGGTCAAG	CTGATTGGCCGTGGTCAAG
Trim30d	TGGAAAAGCTGGAAGAGTCTGAA	TGGAAAAGCTGGAAGAGTCTGAA
Ifit2	CACAGCAGTCATGAGTACAACGAG	CTTCTGCTATCAGGTTCCAGGTG
Oasl1	TCCTGAGGCAGGAGAATTTC	CCCAAAGCAGCCTACCTTGA
Mamdc2	TGCGTTTCTGCCTTGGATACT	TCCATATAGACATAATGGCCTTCCT
Postn	TGGAAACCATTGGAGGCAAA	TGGAAACCATTGGAGGCAAA
Cxcl14	GCGAGGAGAAGATGGTTATCGT	CCCGGTACCTGGACATGCT
Dkk2	TTTTGTTGTGCTCGCCACTT	ATGGAGCACTGGTTTGCAGAT
Cd33	GAGGCAGGAAGCGATCACAT	GTGTATGGAACATCCTGGAGTCAC

Table 8. Primers used for reverse transcription real-time polymerase chain reaction (qRT-PCR)

Primers used for mRNA levels quantification by qRT-PCR.

7.4.2. Objective 2: PHD3 and AD microglia

After microglia FACS of six pools of two 12-month-old mice per genotype (*n* = 3 of *App-Psen1* and *n* = 3 of *Egln3* $^{-/-}$*; App-Psen1)*, cells were pelleted with 200 g centrifugation for 5 min at 4 °C. Supernatant was removed and RNA was extracted with 1 mL TRIzol (Life technologies) following manufacturer's instructions. The quality of RNA was analyzed using Agilent 2100 Bioanalyzer (Agilent). Only RNA samples with RNA integrity number higher than 7 were further processed for microarray analysis and qRT-PCR. RNA was amplified and labeled using GeneChip WT Pico Reagent Kit (total isolated RNA was used as starting material; Affymetrix), subsequently treated with PerfeCTa DNase (Quanta Biosciences) and then copied to cDNA using qScript cDNA Supermix (Quanta Biosciences) in a final volume of 20 µL. The amplified cDNA was quantified and used for microarray analysis with GeneChip® Mouse Transcriptome 1.0 Array (Affymetrix) and qRT-PCR. ViiA 7 Real-Time PCR System (Applied-Biosystems) using Power SYBR-Green PCR Master Mix (Applied-Biosystems) was used to perform the qRT-PCR. Normalization of results by input cDNA amount was performed by including a real time PCR for *Hmbs* mRNA in each plate. ΔΔCt method was used for quantification (Livak & Schmittgen, 2001; Nolan et al., 2006). Primer sequences used are listed in **Table 8**.

7.5. Protein extraction and ELISA

7.5.1. Objective 1: Hypoxia on AβPP processing

Frozen hemibrains (*wild-type* mice) or hemicortices (*App-Psen1* mice) were homogenized with a dounce grinder (Sigma), in 4x m/v solution of PBS containing Protease Inhibitor Cocktail (Roche, 1:25) and Phosphatase Inhibitor (Sigma, 1:100). Afterwards, samples were subjected to a multistep centrifugation to separate soluble from insoluble fractions. First, the samples were centrifuged at 600 g for 5 min at 4 °C to pellet the nuclear fraction. Next, the supernatants were ultracentrifuged at 100000 g for 1 h at 4 °C to isolate PBS-insoluble material (pellets) from PBS-soluble proteins (supernatants). Nuclear and PBS-soluble fractions were stored at -80 °C until use. The 100000 g pellets were dissolved in buffer (8.2 guanidine HCl, 50 mM Tris-HCl), following dilution until 5 M guanidine

and incubated for 4 h at room temperature, with occasional inversion to promote dissolution. These samples were stored at -20 °C until use.

For *wild-type* mice, total protein concentration was quantified with RC-DC kit (Biorad), according to manufacturer's guidelines and using bovine serum albumin (BSA) for the standard curve. VEGF concentration in PBS-soluble fraction was tested in 2-3-month-old *wild-type* mice (*n* = 4 per condition) by ELISA (Quantikine), according to manufacturer's instructions.

For *App-Psen1* samples, total protein concentration was quantified in dissolved PBS-insoluble fraction with RC-DC kit (Biorad), according to manufacturer's guidelines and using bovine serum albumin (BSA) for the standard curve. $A\beta_{1-40}$ and $A\beta_{1-42}$ concentrations were tested in dissolved 100000 pellets of 8-month-old and 14-month-old mice (*n* = 3-4 per group) by using Human Aβ40 ELISA and Human Aβ42 ELISA (Invitrogen) kits, according to manufacturer's guidelines.

7.5.2. Objective 2: PHD3 and AD microglia

For total $A\beta_{1-40}$ and $A\beta_{1-42}$ quantification, 5 hemicortices of 6-month-old *App-Psen1* mice (*n* = 5) and 4 hemicortices of 6-month-old *Egln3* $^{-/-}$*; App-Psen1* mice (*n* = 4) were homogenized with a Dounce grinder (Sigma), in 8x m/v buffer (5 M guanidine HCl, 50 mM Tris-HCl pH 8.0) supplemented with Protease Inhibitor Cocktail (Roche, 1:25) and Phosphatase Inhibitor (Sigma, 1:100). Total protein concentration was quantified with RC-DC kit (Biorad), according to manufacturer's guidelines and using bovine serum albumin (BSA) for the standard curve. $A\beta_{1-40}$ and $A\beta_{1-42}$ concentrations were tested by using Human Aβ40 ELISA and Human Aβ42 ELISA (Invitrogen) kits, according to manufacturer's guidelines.

For soluble $A\beta_{1-40}$ and $A\beta_{1-42}$ quantification, 8 pools of 2 hemicortices from different 6-month-old *App-Psen1* (*n* = 4) and *Egln3* $^{-/-}$*; App-Psen1* (*n* = 4) were homogenized in 1 mL PBS supplemented with Protease Inhibitor Cocktail (Roche, 1:25), Phosphatase Inhibitor (Sigma, 1:100) and 1,10-Phenanthroline 2 mM (Sigma) with a Dounce grinder. Next, samples were subjected to a multistep centrifugation to separate soluble from insoluble fractions. First, the samples were centrifuged at 600 g for 5 min at 4 °C to pellet the nuclear fraction. Next, the supernatants were ultracentrifuge at 100000 g for 1 h at 4 °C to isolate PBS-

insoluble material (pellets) from PBS-soluble proteins (supernatants). Nuclear and PBS-soluble fractions were stored at -80 °C until use. Total protein concentration of 100000 g supernatants was quantified with RC-DC kit (Biorad), according to manufacturer's guidelines and using bovine serum albumin (BSA) for the standard curve. $A\beta_{1-40}$ and $A\beta_{1-42}$ concentrations were tested by using Human Aβ40 ELISA and Human Aβ42 ELISA (Invitrogen) kits, according to manufacturer's guidelines.

7.6. Protein extraction and WB

WB was performed in order to quantify the amount of specific proteins or fragments in different samples and fractions, both for objectives 1 and 2 (Mahmood & Yang, 2012). For objective 1, samples were prepared as previously described for ELISA measurements and particular fractions were used to detect the different protein or samples. In particular, AβPP, C99 and C83 fragments, and BACE1 were detected in the PBS-insoluble fraction; HIF1α was quantified in the nuclear fraction and; sAβPPα was analyzed in the PBS-soluble fraction. For objective 2, HIF1α protein was quantified in the nuclear fraction obtained in the protein extraction process for ELISA $A\beta_{1-40}$ and $A\beta_{1-42}$ measurements and for synaptic proteins detection, total extracts from hemihippocampi were obtained as described next. Protein hippocampal extracts were obtained by homogenization of 6 *wild-type*, 6 *Egln3* $^{-/-}$, 6 *App-Psen1* and 6 *Egln3* $^{-/-}$*; App-Psen1* hemihippocampi in lysis buffer (Tris-HCl 30 mM, Thiourea 2 M, Urea 7 M, CHAPS 4 % m/v, pH 8.5). Control group was integrated by *wild-type* and *Egln3* $^{-/-}$ measurements to increase statistical power, since no differences were observed between these two groups. Tissue homogenization was performed in a tissue homogenizer (Bullet Blender, Next Advance) in the presence of glass beads. Supernatant protein concentration after 15000 g spin was quantified with RC-DC kit (Biorad), according to manufacturer's guidelines and using bovine serum albumin (BSA) for the standard curve.

In brief, WBs were performed on sodium dodecyl sulfate polyacrylamide gel electrophoresis (SDS-PAGE) in order to identify proteins from a complex mixture by molecular weight. Tris-glycine gels at 10 % polyacrylamide (40 % Acrylamide/Bis Solution, 29:1, 3.3 % C, Biorad) gels were used for all WBs

except for C99/C83 gels, which were based on Tris-tricine gels at 16 % polyacrylamide. Gels were polymerized using Mini-Protean® II Cell (Biorad) system and protein samples were boiled in the presence of 2-mercaptoethanol (Sigma) prior electrophoretic migration, except from V-GLUT 1 samples. Protein transfer from protein-containing gels to polyvinylidene difluoride (PVDF, Millipore) previously activated membranes, following manufacturer's instructions, was performed with semi-dry system (Sigma). Protein-containing membranes were blocked with 5 % skimmed milk in PBS-Tween20 0.1 % (m/v) and incubated over night with corresponding primary antibodies diluted in blocking solution. Secondary antibodies were diluted in PBS-Tween20 0.1 % and applied to protein-containing membranes for 1 h at room temperature. Secondary antibody signal was detected in ImageQuant™ LAS 4000 (GE Healthcare) system after incubation with Clarity™ Western ECL Substrate (Biorad), following manufacturer's guidelines. Acquired images were quantified with ImageQuant software and protein load was obtained after normalization by corresponding lane control load protein.

Table 9 lists all identified proteins or fragments, used samples for identification, protein loads in each well of the corresponding gels and antibodies used in each case. **Table 10** contains relevant data on the antibodies utilized.

Protein	Sample	Load (ug)	Antibodies (manufacturer)
HIF1α	Nuclear fraction	50	Anti-HIF1a (Cayman)
BACE1	PBS-insoluble fraction	20	Anti-Bace (Cell signaling)
FL-AβPP	PBS-insoluble fraction	40	Anti-CTF (Millipore)
sAβPPα	PBS-soluble fraction	30	Anti-sAPPa (Takara)
Synaptophysin 1	LB1 hippocampal extract	1	Anti-Synaptophysin 1 (Synaptic Systems)
PSD-95	LB1 hippocampal extract	5	Anti-PSD95 (Millipore)
V-GLUT 1	LB1 hippocampal extract	10	Anti-VGLUT 1 (Synaptic Systems)
C99 and C83	PBS-insoluble fraction	30	Anti-Ab 6e10 clone (Biolegend) and Anti-Ab 82E1 clone (IBL)

Table 9. Proteins or peptides detected by western blot (WB) and corresponding antibodies.

Detected proteins or peptides by WB, fraction or sample of origin, protein load in the gel for electrophoresis, and used antibodies. Loading control proteins are excluded. Abbreviations: HIF1α, hypoxia-inducible factor 1α; FL-AβPP: full length amyloid-β precursor protein; sAβPPα, soluble amyloid-β precursor protein; PSD-95,

postsynaptic-density-95; VGLUT-1, vesicular glutamate transporter-1; C83, α C-terminal fragment; C99; β C-terminal fragment.

Antibody	Manufacturer	Catalog #	Dilution	Approximate MW
Rabbit anti-HIF1α (C-Term)	Cayman	10006421	1:100	140 KDa
Rabbit anti-Bace (D10E5)	Cell signaling	#5606	1:1000	70 Kda
Rabbit anti-Amyloid β Precursor Protein, C-Terminal (751-770)	Millipore	171610	1:5000	110 Kda
Mouse anti-β-Amyloid, 1-16 Antibody (clon 6e10)	Biolegend	803003	1:6000	C99 11 Kda, C83 4 Kda
Mouse anti-Human Amyloid β (N) (clon 82E1)	IBL	10323	1:6000	C99 11 Kda, C83 4 Kda
Mouse anti-sAβPPα (2B3)	Takara	11088	1:500	95 Kda
Rabbit anti-synaptophysin 1	Synaptic Systems	101 002	1:5000	40 Kda
Mouse anti-PSD-95	Millipore	MAB1596	1:1000	95 Kda
Rabbit anti-VGLUT-1	Synaptic Systems	135 303	1:1000	60 Kda
Mouse anti-α-tubulin	SIGMA	T5168	1:4000	55 Kda
Mouse anti-β-actin	Abcam	ab6276	1:5000	45 Kda
Mouse anti-pan Cadherin	Abcam	ab6528	1:1000	130 Kda
Rabbit anti-RPL26	Sigma	R0655	1:1000	17 Kda
Goat anti-Rabbit IgG (H+L) Secondary Antibody, HRP	ThermoFisher	31460	1:10000	N/A
Sheep anti-Mouse IgG, HRP-Specific Whole Antibody	Amersham	NA931	1:10000	N/A

Table 10. Data on used antibodies for western blot (WB).
List of all antibodies utilized for protein quantification by WB with additional data. Abbreviations: MW, molecular weight; HIF1α, hypoxia-inducible factor 1α; sAβPPα, soluble amyloid-β precursor protein; PSD-95, postsynaptic-density-95; VGLUT-1, vesicular glutamate transporter-1; C83, α C-terminal fragment; C99; β C-terminal fragment; RPL26, ribosomal protein L26.

7.7. Microglia FACS and *in vivo* phagocytosis assay

Microglia isolation was performed as previously described (Orre, Kamphuis, Osborn, Melief, et al., 2014) in 6 *wild-type*, 3 *Egln3* $^{-/-}$, 5 *App-Psen1* and 5 *Egln3* $^{-/-}$*; App-Psen1* mice. In order to increase statistical power, *wild-type* and *Egln3* $^{-/-}$ data were pooled as control group (n = 9) since no differences were observed in any of the analyzed parameters. Briefly, mice were anesthetized and transcardially perfused with HBSS (-$CaCl_2$/-$MgCl_2$) (Gibco) and complete cortex was dissected and subsequently subjected to dissociation using a Tissue Chopper (Vibratome 800 series). A chemical digestion was performed using a combination of Papain

(Worthington) at a final concentration of 8 U/mL and DNAse I at a final concentration of 80 Kunitz units/mL (Sigma) followed by a Percoll gradient (GE healthcare) at 90 % in PBS (v/v) for microglia enrichment. Cells were incubated with anti-CD11b-APC and anti-CD45-PE antibodies at 4 °C for 30 min. Staining with isotype control-PE and isotype control-APC was used as negative control staining. Both control and experimental samples were incubated with anti-CD16/CD32 blocker antibody. All antibodies were used at 1:200 dilution. **Table 11** lists antibodies, manufacturers and catalog number. 7-AAD (BD Pharmingen) was added at a concentration of 1:100 to samples to confirm alive microglia isolation, as previously described (Orre, Kamphuis, Osborn, Melief, et al., 2014). Cells were washed and sorted using a FACS Aria Fusion (Becton Dickinson) flow cytometer and data were acquired and analysed with FACSDiva software 8.0 (Becton Dickinson).

Antibody	Host species	Manufacturer	Catalog #
Anti-CD16/CD32 (Mouse BD Fc Block)	Rat	BD Biosciences	553142
Anti-CD45 PE	Rat	Thermo scientific	12-0451
Rat IgG2b Kappa Isotype Control PE	Rat	Thermo scientific	12-4031
Anti-CD11b APC	Rat	Thermo scientific	17-0112
Rat IgG2b K Isotype Control APC	Rat	Thermo scientific	17-4031

Table 11. Data on used antibodies for flow cytometry.
List of antibodies used for fluorescent-activated cell sorting (FACS) and phagocytic assays.

Gating strategy and data analysis was made according to guidelines and previous reports (Herzenberg et al., 2006; Orre, Kamphuis, Osborn, Melief, et al., 2014) (**Figure 34**). Debris and dead cells were discarded by forward and side scatter pattern. Alive cells were selected by 7-AAD fluorescence. FSC-A and FSC-H events distribution was used to gate single cells. Microglial cells were identified as a positive population for both CD11b and CD45 markers. Microglial subpopulation gating was performed on contour density plot scaled at 15% probability. A second microglial population was considered when more than one independent focus was observed with these settings. Percentages are relative to total single cells.

Microglial phagocytosis was tested by measuring % of microglia from total single cells incorporating methoxy-X04 (Tocris Bioscience) as previously described (Heneka et al., 2013). Concisely, 3 *App-Psen1* and 3 *Egln3* $^{-/-}$*; App-Psen1* 12-month-old mice were injected with 10 mg/Kg of methoxy-X04 in 50 % DMSO/50 % NaCl 0.9 % intraperitoneally. After 3 h of incubation, the same microglia isolation protocol previously described was applied. Cells were analysed in FACSCanto II (Becton Dickinson) and data were acquired and analysed with FACSDiva software 8.0 (Becton Dickinson). The same gating strategy was used to select microglia and negative threshold for methoxy-X04 was established considering microglia from *Egln3* $^{-/-}$ mice subjected to this protocol and *App-Psen1* mice without methoxy-X04 injections.

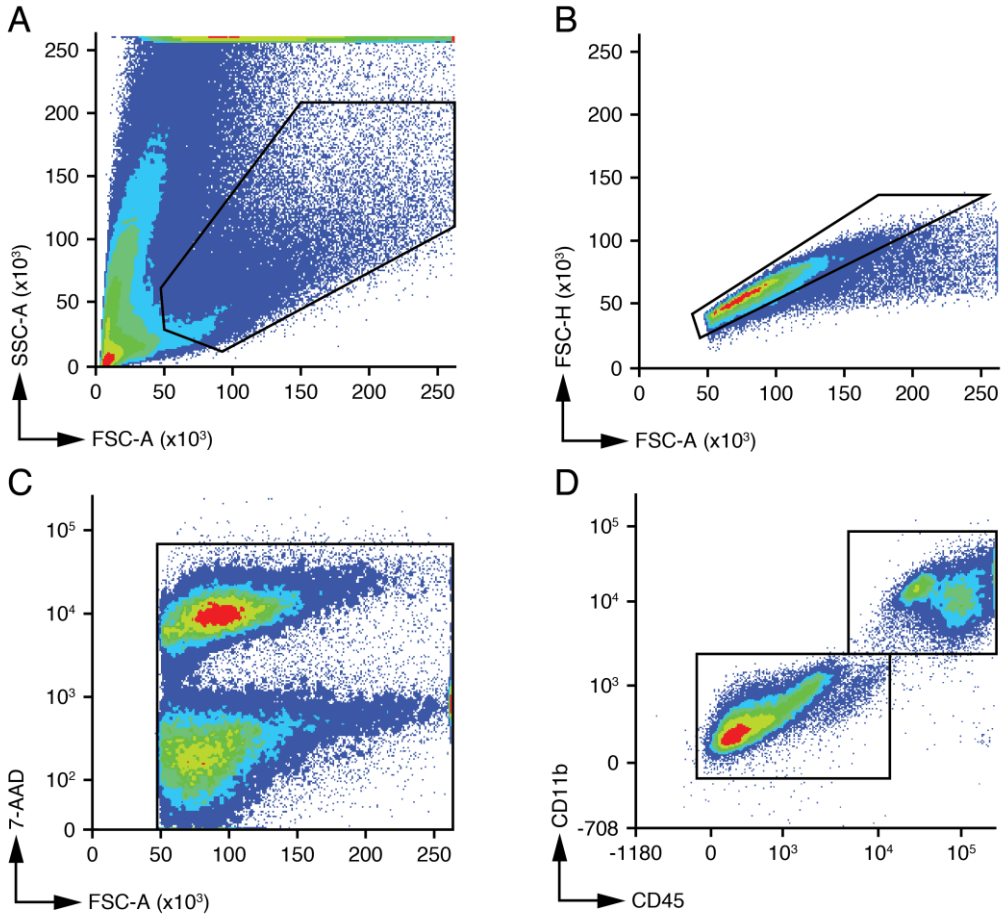

Figure 34. Gating strategy used for isolation and analysis of viable microglial cells *in vivo* and microglial amyloid-β phagocytosis measurement.

(A-D) Gating strategy was performed according to guidelines and previous reports (Herzenberg et al., 2006; Orre et al., 2014) in contour density plots. (A) Debris and dead cells were discarded by forward (FSC) and side (SSC) scatters dispersion of events. (B) Singlets of events were selected according to FSC area *versus* height. (C)

7-ADD staining was performed as control to test alive microglial cells isolation. (D) Microglial cells, positive for CD45 and CD11b markers, were selected and a subdivided according to CD45 axis when a second microglial subpopulation was observed.

7.8. Tissue processing for immunostaining

Mice were euthanized and cerebral samples fixed as previously described. Except for tissues for *in situ* hybridization protocol, tissues were included in paraffin by an automated tissue processor (Leica) that sequentially dehydrates the sample until final embed in paraffin. Paraffin samples were further embedded in paraffin blocks for posterior 20 µm slicing with a paraffin microtome (Leica). Tissue slices were kept at 37 °C over night to allow full drying of samples.

7.9. Immunofluorescent staining for IBA1, Aβ, Thio-S and DAPI

Slices were deparaffinized and rehydrated by sequential incubation in xylene, declining ethanol concentration washes, and H_2Od. Antigen retrieval was performed in an automated system (2100 Retriever) in sodium citrate buffer (10 mM Tri-sodium citrate dehydrate (Merk), pH 6). Next, slices were washed and permeabilized with PBS washes, a PBS-Triton X100 (Amresco) 0.3 % (v/v) and PBS-Triton X100 0.1 % (v/v) washes. Following blocking and over-night corresponding primary anti-IBA1 (Wako, Cat.# 019-19741, 1:500) and/or anti-Aβ antibody (Biolegend, , Cat.# 803001, 1:1000) incubation were performed with blocking solution (1 % bovine serum albumin (m/v, Applichem), 10 % goat serum (v/v, Gibco), in PBS-Triton X100 0.1 % (v/v)).

After PBS-Triton X100 0.1 % (v/v) washes, secondary fluorescent antibodies anti-rabbit conjugated with Alexa-568 (Invitrogen, Cat.# A11011, 1:800), anti-mouse conjugated with Alexa-488 (Invitrogen, Cat.# A11001, 1:800). Slices were mounted in aqueous medium (Fluoromount-G, Southern biotech) after PBS-Triton X100 0.1 % (v/v) and PBS washes.

When corresponding, prior to mounting, Thio-S (Sigma) 0.005 % (m/v) in PBS staining was performed and, whether appropriate, DAPI (Sigma, 1:1000) staining

was performed afterwards. After several PBS-Triton X100 0.1 % (v/v) and PBS washes, slices were mounted in aqueous medium (Fluoromount-G, Southern biotech).

7.10. Immunofluorescent staining for fAβ

All steps were common to previously described protocol for IBA1 and Aβ staining, but the protocol was extended after secondary antibody incubation. Also, both primary and secondary employed antibodies were different. Primary anti-OC (Millipore, Cat.#AB2286, 1:1000) and secondary anti-rabbit-biotin-SP-Conjugated (Jackson IR, Cat.#711-065-152, 1:800) antibodies were used. Then, after PBS washes, Cy3-conjugated streptavidin (Jackson IR, Cat.#016-160-084, 1:500) was used to amplify primary antibody's signal. Thio-S staining, as previously described, and mounting were the final steps.

7.11. Immunochemical staining for IBA1, fAβ and P-Tau

Slices were deparaffinized, rehydrated, and their antigens were retrieved as previously described for immunofluorescent staining. Then, tissue endogenous peroxidase was neutralized with 3 % H_2O_2 (DAKO) for 5', with previous and posterior H_2O washes. Blocking was performed with 1 % bovine serum albumin (m/v), 5 % goat serum (v/v), in PBS-Triton X100 0.2 % (v/v) and followed by primary antibody incubation, either anti-OC (Millipore, Cat.#AB2286, 1:500), anti-IBA1 (Wako, Cat.# 019-19741, 1:500) or anti-phosphorylated-Tau (Pierce, Cat.#MN1020, 1:300) in 1 % BSA (m/v), 5 % goat serum (v/v), in PBS overnight.

After PBS washes, labeled polymer-HRP anti-rabbit (DAKO) was used to label anti-OC and anti-IBA1 antibodies and labeled polymer-HRP anti-mouse (DAKO) was used to label anti-phosphorylated-Tau antibody.

Chemical reaction to visualize antibodies location was performed with Master Diagnostica Kit, according to manufacturer's guidelines, and samples were subsequently washed.

In the case of anti-OC and anti-IBA1 antibody staining, samples were dehydrated with increasing ethanol concentration washes, ended up in xylene prior to DPX mounting (Sigma).

In the case of anti-phosphorylated-Tau staining, amyloid plaques were stained with Thio-S 0.05% in ethanol 50 % (m/v) and mounted in Fluoromount-G afterwards.

7.12. *In situ* hybridization in combination with immunostaining and image acquisition

Mice were euthanized and cerebral samples fixed as previously described. Tissues were cryoprotected in sucrose 10 %, 20 % and 30 % in PBS (m/v) at 4 °C for 18 h and embedded in OCT compound (Tissue-Tek) prior to -80 °C storage. Coronal slices of 10 µm were obtained with a cryostat (Leyca) and stored at -80 °C until use.

RNAscope 2.5 (ACD) protocol was used to detect *Egln3* mRNA with *Egln3* probe (ACD) according to manufacturer's instructions for frozen tissue, using a HybEZ oven (ACD). Subsequent immunostaining was performed for microglia staining (with IBA1 marker) and nuclear staining (DAPI dye). After RNAscope 2.5 protocol, slices were incubated for 10 min in PBS-Triton X100 0.3 % (v/v) and washed in PBS. Anti-IBA1 antibody (Wako, Cat.# 019-19741, 1:500) was prepared in PBS-Triton X100 0.05 % (v/v), goat serum 2 % (v/v, Gibco) and used to incubate the samples over night at 4 °C. After several PBS washes, slices were incubated with anti-rabbit conjugated with Alexa 488 (Invitrogen, A11034, 1:400) for 1 h at room temperature. Several PBS washes and DAPI (Sigma, 1:1000) for 5 min were the final steps before mounting with Fluoromount-G.

Images from compact amyloid plaques in cortical regions of *App*-Psen1 mice were acquired in a confocal microscope (Nikon) in Z-stack series and colocalization images were performed by decreasing opacity of the fluorescent images.

7.13. Burden quantification of IBA1, Thio-S, Aβ and fAβ

Staining of paraffin-embedded hemibrain slices was performed as previously described for each marker, with immunofluorescent staining in the case of IBA1, Thio-S, and Aβ, and immunochemical staining of fAβ with anti-OC antibody.

Measurements were performed in superimages, blind to the genotypes and neuroanatomy was assessed using The Mouse Brain in Stereotaxic Coordinates (Franklin & Paxinos, 2008). Superimages were obtained at 10x magnification from 3 whole hemicortices of 3-6 *App-Psen1* and 3-6 *Egln3* $^{-/-}$*; App-Psen1* 6-month-old mice with New CAST BX61 (Olympus), by using the same microscope settings for all images of the same staining. Briefly, 3 slices of each mouse, from -1.70 mm to -2.30 mm relative to Bregma, were selected. With New CAST BX61, upper-left and bottom-right limits of every hemibrain slice were set, delimiting a virtual rectangle that comprised the whole area to be pictured in the superimage. Then, an automated acquisition was launched with the microimager utility that resulted in a superimage composed of all the different pictures taken at the specified settings to cover the whole previously delimited area.

Fiji software (Schindelin et al., 2012) was utilized to analyze the superimages. Superimages were transformed into 8-bit images and only cortical area was selected for analyses. Cortical area was manually outlined and regions with evident noise or artifacts were subtracted from the analysis. A specific upper and lower threshold was applied for each marker and maintained throughout all the quantifications to create segmented binary masks (**table 12**). Analyze particles utility was used to calculate the total area covered by all particles contained in the segmented binary mask, meeting size criteria of the analyze particles utility. The percentage of occupancy was calculated as the ratio of total particles area divided by total cortical area for each slice and multiplied by 100. In the case of Thio-S stained amyloid plaques, number and size of each quantified particle was obtained for further analysis. Amyloid plaques density was calculated for each slice as the total number of particles quantified in each cortical area divided by total cortical area of that specific slice. Average size was obtained as the mean size of all the particles quantified in each hemicortex. Size distribution plot was obtained with

Graphpad Prism 6.0 version by calculating the mean number of particles of each size interval detected in each cortex. All showed data and statistical analyses correspond to the consideration of every slice as a replicate (*n* for each marker is listed in **table 12**).

Marker	Minimum detected size (μm^2)	Lower threshold	Upper threshold	Number of replicates
IBA1	14.2	21	255	18
Thio-S	42.50	25	255	9
Aβ	1.5	13	255	18
OC	11.0	78	169	18

Table 12. Settings used for image analysis with Fiji software.
Quantified markers with more limiting settings and number of considered replicates for statistical analysis of results. Abbreviations: IBA1, ionized calcium-binding adapter molecule 1; Thio-S, Thioflavine-S; Aβ, amyloid-β.

7.14. Neuronal dystrophies occupied area

Staining of paraffin-embedded hemibrain slices was performed as previously described for both markers in the same samples, with immunofluorescent staining in the case of Thio-S and immunochemical staining of P-Tau.

Compact Thio-S stained plaques along the whole hemicortex of 5 *App-Psen1* and 5 *App-Psen1, Egln3* $^{-/-}$ 6 month-old mice (24 plaques in 3 slices per animal) of same size were randomly pictured, with the same settings in all cases. 16-slice-Z-projections at 40x magnification were performed to acquire all P-Tau signal of each selected plaque by generating a maximum intensity projection image afterwards, in an Olympus BX61 microscope, from -1.70 mm and -2.06 mm relative to Bregma. Fiji software (Schindelin et al., 2012) was used to quantify occupied area by amyloid plaques and P-Tau. Pictures were transformed into 8-bit images and automated thresholding segmentation with lower threshold of 16 for Thio-S area and 0 for P-Tau area and upper threshold of 255 for both markers was carried out and subsequent analyze particles utility revealed calculated sizes. Ratio P-Tau area/amyloid plaque area was calculated. All showed data and statistical analyses correspond to the consideration of every slice as a replicate (n = 15).

7.15. fAβ from individual plaques

Immunofluorescent staining of paraffin-embedded hemibrain slices was performed as previously described for both Thio-S and OC markers in the same samples.

Compact Thio-S stained plaques along the whole hemicortex of 6 *App-Psen1* and 6 *App-Psen1, Egln3* $^{-/-}$ 6 month-old mice (15 plaques in 3 slices per animal) of same size were randomly pictured, with the same settings in all cases. Fluorescent OC signal of each selected plaque was also acquired, with same settings for all images. Images were acquired in an Olympus BX61 microscope at 40x magnification, from -1.70 mm and -2.06 mm relative to Bregma.

Fiji software (Schindelin et al., 2012) was used to quantify occupied area by dense core of Aβ plaques and fAβ (OC signal). A third analysis omitting occupied area of Thio-S calculated dense core was performed to exclusively quantify fAβ halo. Pictures were transformed into 8-bit images and automated thresholding segmentation with lower threshold of 35 for Thio-S area and 0 for OC area and upper threshold of 255 for both markers was carried out and subsequent analyze particles utility revealed calculated sizes. Ratio OC halo area / Aβ dense core area was calculated. All showed data and statistical analyses correspond to the consideration of every slice as a replicate (n = 18).

7.16. MPI

Immunofluorescent staining of paraffin-embedded hemibrain slices was performed as previously described for all DAPI, Aβ, with anti-Aβ antibody, and IBA1 markers in the same samples.

MPI was calculated as the proportion of microglial cells in contact with each Aβ plaque considering all microglia closer than 40 μm from Aβ plaque's border. It was obtained through the analysis of randomly compact selected plaques of the same size from 3 *App-Psen1* and 3 *App-Psen1, Egln3*$^{-/-}$ 6 months old mice (15 plaques in 3 slices per mouse). All pictures were taken with New CAST BX61 (Olympus) at 40x magnification, with 3 pictures per plaque in Z-axis and generating a maximum intensity projection image afterwards. Sampling area included the whole cortex

areas from Auditory Cortex to Piriform Cortex from -1.94 mm and -2.30 mm relative to Bregma.

Aβ plaques area was measured by using Fiji software (Schindelin et al., 2012), by transforming pictures into 8-bit images, applying a lower threshold of 0 and an upper threshold of 255, and using analyze particles utility. The region of interest generated after amyloid plaques measurement by Fiji was submitted to enlarge function of this software in order to extend its periphery 40 μm. All microglia whose soma was within the increased halo was quantified by IBA1 marker colocalization with nuclear DAPI staining. Separately, microglia directly in contact with Aβ plaque within the increased halo was also quantified. A ratio between microglia directly in contact with Aβ plaque and previously quantified total microglia in each plaque was obtained. All showed data and statistical analyses correspond to the consideration of every slice as a replicate (n = 9).

7.17. Microglia morphology

Immunochemical staining of paraffin-embedded hemibrain slices was performed as previously described for IBA1 marker.

Individual microglial cells from the dorso-lateral hemicortex of 6 *App-Psen1* and 6 *App-Psen1, Egln3* $^{-/-}$ 6 month-old mice (12 cells in 3 slices per animal) were randomly pictured, with the same settings in all cases. Images were acquired in 18 Z-stacks in an Olympus BX61 microscope at 100x magnification, from -1.70 mm and -2.06 mm relative to Bregma. Maximum intensity projections were obtained for further analysis.

The described process in results section was used to get insights in the ramification levels of microglia and their occupied area, as well as their ratio of projections size and soma size. Blue circumference area was 1108.24 μm^2, green circumference area was 667.91 μm^2 and red circumference area was 155.02 μm^2. All quantified data and statistical analyses correspond to the consideration of every slice as a replicate (n = 18).

7.18. Stereological microglia density estimation

Immunofluorescent staining of paraffin-embedded hemibrain slices was performed as previously described for both DAPI and IBA1 markers in the same samples.

Microglia density estimation by unbiased stereological analysis was accomplished by systematic random sampling using a CAST Grid System (Olympus). A 25 % of complete hemicortex was sampled with dissectors of 106954.7 μm^2 in 3 slices per animal, with 6 *App-Psen1* and 4 *Egln3* $^{-/-}$; *App-Psen1* of 6 month-old mice, from -1.70 mm and -2.06 mm relative to Bregma. Cortical area was manually outlined at 4x magnification. Microglia cell number in dissectors was quantified by IBA1 marker colocalization with nuclear DAPI staining at 20x magnification. For each hemicortex, total sampled area was obtained by multiplying dissector area by number of dissectors. Microglial density was obtained by dividing total microglial cell number by total sampled area. All showed data and statistical analyses correspond to the consideration of every slice as a replicate (n = 18 for *App-Psen1* and n = 12 for *Egln3* $^{-/-}$; *App-Psen1* mice).

7.19. Stereological amyloid plaques density estimation

Immunofluorescent staining of paraffin-embedded hemibrain slices was performed as previously described for Thio-S.

All Thio-S positive dense-core amyloid plaques bigger than 55 μm^2 were quantified in the whole cortical area and classified into filamentous, if no dense core was visible, or compact plaques, in which a dull and compact dense core is identifiable. Plaques were visualized at 20x magnification in CAST Grid System (Olympus). Total cortical area was calculated in this microscope with the Cavalieri method. Plaque densities, in terms of number of plaques per area, were obtained by dividing total number of each type of plaques by total cortical area. Quantifications were performed in 3 slices per animal, with 6 *App-Psen1* and 7 *Egln3* $^{-/-}$; *App-Psen1* of 6 month-old mice, from -1.46 mm to -1.82 mm relative to Bregma. All showed

data and statistical analyses correspond to the consideration of every slice as a replicate (n = 18 for *App-Psen1* and n = 21 for *Egln3* $^{-/-}$; *App-Psen1* mice).

7.20. Behavioural tests

Wild-type and *Egln3* $^{-/-}$ were grouped as control mice given that no differences were shown in any of the analyzed parameters.

For behavioural assessment of locomotion activity and open field test was used. 6 month-old mice were filmed in a 45 x 45 cm floor box using an automatic tracking system (SMART). 16 control mice, 18 *App-Psen1* and 14 *App-Psen1, Egln3* $^{-/-}$ mice were recorded for 15 min following the protocol from the International Mouse Phenotyping Resource of Standardized Screens (IMPRESS; https://www.mousephenotype.org/impress/protocol/81/7) and the travelled distance was calculated using the SMART software 3.0 (Panlab-Harvard Apparatus).

Short-term memory was evaluated following a previously published protocol (Leger et al., 2013) based on a novel object recognition strategy. 14 control mice, 21 *App-Psen1* mice and 14 *App-Psen1, Egln3* $^{-/-}$ mice of 6 months old were submitted to the test. In brief, two objects were presented to each mouse for 15 min. After one hour, the mouse was exposed to one of the previous objects being the other one replaced for a new object. A short-term memory index was calculated by subtracting the number of the approaches to the novel object minus the number of approaches to the old object divided by the total number of approaches. Recording and analyzing software was SMART 3.0 (Panlab-Harvard Apparatus).

7.21. Statistical analysis

All measurements were performed in at least 3 independent mice.

7.21.1. Statistical analysis for objective 1

Given the small size of the groups, only non-parametric statistical tests were used. Comparisons between two groups were performed with Mann-Whitney *U* test,

whereas comparisons among three groups were done with Kruskal-Wallis ANOVA with Dunn's multiple comparison test. Level of significance was set at $p < 0.05$. Data are expressed as mean ± s.e.m. Statistical analyses and graphs were performed in GraphPad Prism version 7.0 (GraphPad Inc.).

7.21.2. Statistical analysis for objective 2

Samples with an $n \geq 5$ were evaluated for normal distribution using Kolmogorov-Smirnov's normality test. Non-normal samples were analysed using non-parametric tests. Samples with an $n < 5$ were analysed using parametric tests. Comparisons between two groups were performed with two-tail unpaired Student's *t*-test (for normally distributed data) or Mann Whitney's *U* test (non-normally distributed data). Comparison among more than two groups was done with Kruskal-Wallis's ANOVA with Dunn's multiple comparison test, if data were not-normally distributed or with ANOVA followed by Tukey's test or Newman-Keuls' test, if more power was required, for normally-distributed data. Plots are represented with mean ± s.e.m.; $p \leq 0.05$ was considered statistically significant. Statistical analyses and graphs were performed in GraphPad Prism version 6.0 (GraphPad Inc.).

8. Bibliography

Arriagada, P. V, Growdon, J. H., Hedley-Whyte, E. T., & Hyman, B. T. (1992). Neurofibrillary tangles but not senile plaques parallel duration and severity of Alzheimer's disease. *Neurology*, *42*(3), 631–631.

Augustinack, J. C., Schneider, A., Mandelkow, E. M., & Hyman, B. T. (2002). Specific tau phosphorylation sites correlate with severity of neuronal cytopathology in Alzheimer's disease. *Acta Neuropathologica*, *103*(1), 26–35.

Bazan, N. G., & Lukiw, W. J. (2002). Cyclooxygenase-2 and presenilin-1 gene expression induced by interleukin-1beta and amyloid beta 42 peptide is potentiated by hypoxia in primary human neural cells. *The Journal of Biological Chemistry*, *277*(33), 30359–30367.

Benita, Y., Kikuchi, H., Smith, A. D., Zhang, M. Q., Chung, D. C., & Xavier, R. J. (2009). An integrative genomics approach identifies Hypoxia Inducible Factor-1 (HIF-1)-target genes that form the core response to hypoxia. *Nucleic Acids Research*, *37*(14), 4587–4602.

Berra, E., Benizri, E., Ginouvès, A., Volmat, V., Roux, D., & Pouysségur, J. (2003). HIF prolyl-hydroxylase 2 is the key oxygen sensor setting low steady-state levels of HIF-1α in normoxia. *EMBO Journal*, *22*(16), 4082–4090.

Bettens, K., Sleegers, K., & Van Broeckhoven, C. (2013). Genetic insights in Alzheimer's disease. *The Lancet Neurology*, *12*, 92-104.

Bierer, L. M., Carlin, L., Schmeidler, J., Davis, K. L., Hof, P. R., Purohit, D. P., & Perl, D. P. (1995). Neocortical Neurofibrillary Tangles Correlate with Dementia Severity in Alzheimer's Disease. *Archives of Neurology*, *52*(1), 81–88.

Birch, A. M. (2014). The contribution of astrocytes to Alzheimer's disease. *Biochemical Society Transactions*, *42*(5), 1316–1320.

Bishop, T., Gallagher, D., Pascual, A., Lygate, C. A., de Bono, J. P., Nicholls, L. G., … Ratcliffe, P. J. (2008). Abnormal Sympathoadrenal Development and Systemic Hypotension in PHD3-/- Mice. *Molecular and Cellular Biology*, *28*(10), 3386–

Braak, F., Braak, H., & Mandelkow, E. M. (1994). A sequence of cytoskeleton changes related to the formation of neurofibrillary tangles and neuropil threads. *Acta Neuropathologica*, *87*(6), 554–567.

Burdick, D., Soreghan, B., Kwon, M., Kosmoski, J., Knauer, M., Henschen, A., … Glabell, C. (1992). Assembly and Aggregation Properties of Synthetic Alzheimer's A4/Beta Amyloid Peptide Analogs. The Journal of Biologycal Chemistry, *267*(1), 546–554.

Cai, H., Wang, Y., McCarthy, D., Wen, H., Borchelt, D. R., Price, D. L., & Wong, P. C. (2001). BACE1 is the major β-secretase for generation of Aβ peptides by neurons. *Nature Neuroscience*, *4*(3), 233–234.

Campanella, M., Sciorati, C., Tarozzo, G., & Beltramo, M. (2002). Flow cytometric analysis of inflammatory cells in ischemic rat brain. *Stroke*, *33*(2), 586–592.

Casazza, A., Laoui, D., Wenes, M., Rizzolio, S., Bassani, N., Mambretti, M., … Mazzone, M. (2013). Impeding Macrophage Entry into Hypoxic Tumor Areas by Sema3A/Nrp1 Signaling Blockade Inhibits Angiogenesis and Restores Antitumor Immunity. *Cancer Cell*, *24*(6), 695–709.

Charbonneau, H., Tonks, N. K., Walsh, K. A., & Fischer, E. H. (1988). The leukocyte common antigen (CD45): A putative receptor-linked protein tyrosine phosphatase. *Biochemistry*, *85*, 7182–7186.

Chen, G.-J., Xu, J., Lahousse, S. a, Caggiano, N. L., & de la Monte, S. M. (2003). Transient hypoxia causes Alzheimer-type molecular and biochemical abnormalities in cortical neurons: potential strategies for neuroprotection. *Journal of Alzheimer's Disease : JAD*, *5*, 209–228.

Chung, H., Brazil, M. I., Soe, T. T., & Maxfield, F. R. (1999). Uptake, degradation, and release of fibrillar and soluble forms of Alzheimer's amyloid beta-peptide by microglial cells. *J Biol Chem*, *274*(45), 32301–32308.

Colgan, S. P., & Taylor, C. T. (2010). Hypoxia: An alarm signal during intestinal inflammation. *Nature Reviews Gastroenterology and Hepatology*, *7*, 281-287.

Colton, C. A. (2009). Heterogeneity of microglial activation in the innate immune response in the brain. *Journal of Neuroimmune Pharmacology*, *4*, 399-418.

Combs, C. K. (2009). Inflammation and microglia actions in alzheimer's disease. *Journal of Neuroimmune Pharmacology*, *4*, 380-388.

Condello, C., Yuan, P., & Grutzendler, J. (2017). Microglia-Mediated Neuroprotection, TREM2, and Alzheimer's Disease: Evidence From Optical Imaging. *Biological Psychiatry*, *83*, 377–387.

Condello, C., Yuan, P., Schain, A., & Grutzendler, J. (2015). Microglia constitute a barrier that prevents neurotoxic protofibrillar Aβ42 hotspots around plaques. *Nature Communications*, *6*, 6176.

Cooke, J. R., Ayalon, L., Palmer, B. W., Loredo, J. S., Corey-Bloom, J., Natarajan, L., … Ancoli-Israel, S. (2009). Sustained use of CPAP slows deterioration of cognition, sleep, and mood in patients with Alzheimer's disease and obstructive sleep apnea: A preliminary study. *Journal of Clinical Sleep Medicine*, *5*(4), 305–309.

Corder, E. H., Saunders, A. M., Strittmatter, W. J., Schmechel, D. E., Gaskell, P. C., Small, G. W., … Pericak-Vance, M. A. (1993). Gene dose of apolipoprotein E type 4 allele and the risk of Alzheimer's disease in late onset families. *Science*, *261*(5123), 921–923.

Cramer, T., Yamanishi, Y., Clausen, B. E., Förster, I., Pawlinski, R., Mackman, N., … Johnson, R. S. (2003). HIF-1α is essential for myeloid cell-mediated inflammation. *Cell*, *112*(5), 645–657.

Crotti, A., & Ransohoff, R. M. (2016, March 15). Microglial Physiology and Pathophysiology: Insights from Genome-wide Transcriptional Profiling. *Immunity*. Elsevier.

Cummins, E. P., Berra, E., Comerford, K. M., Ginouves, A., Fitzgerald, K. T., Seeballuck, F., … Taylor, C. T. (2006). Prolyl hydroxylase-1 negatively regulates IkB kinase-beta, giving insight into hypoxia-induced NF-kB activity. *Proceedings of the National Academy of Sciences*, *103*(48), 18154–18159.

D'Anglemont de Tassigny, X., Pardal, R., Gomez-pinedo, U., & Capilla-gonzalez, V. (2015). Resistance of subventricular neural stem cells to chronic hypoxemia despite structural disorganization of the germinal center and impairment of neuronal and oligodendrocyte. *Hypoxia*, *3*, 15–33.

De Strooper, B., Iwatsubo, T., & Wolfe, M. S. (2012). Presenilins and γ-secretase: Structure, function, and role in Alzheimer disease. *Cold Spring Harbor Perspectives in Medicine*, *2*(1), a006304.

DeKosky, S. T., & Scheff, S. W. (1990). Synapse loss in frontal cortex biopsies in Alzheimer's disease: Correlation with cognitive severity. *Annals of Neurology*, *27*(5), 457–464.

del Peso, L., Castellanos, M. C., Temes, E., Martin-Puig, S., Cuevas, Y., Olmos, G., & Landazuri, M. O. (2003). The von Hippel Lindau/hypoxia-inducible factor (HIF) pathway regulates the transcription of the HIF-proline hydroxylase genes in response to low oxygen. *The Journal of Biological Chemistry*, *278*(49), 48690–48695.

Denker, S. P., Ji, S., Dingman, A., Lee, S. Y., Derugin, N., Wendland, M. F., & Vexler, Z. S. (2007). Macrophages are comprised of resident brain microglia not infiltrating peripheral monocytes acutely after neonatal stroke. *Journal of Neurochemistry*, *100*(4), 893–904.

Dickerson, B. C., Bakkour, A., Salat, D. H., Feczko, E., Pacheco, J., Greve, D. N., … Buckner, R. L. (2009). The cortical signature of Alzheimer's disease: Regionally specific cortical thinning relates to symptom severity in very mild to mild AD dementia and is detectable in asymptomatic amyloid-positive individuals. *Cerebral Cortex*, *19*(3), 497–510.

Dickson, T. C., King, C. E., McCormack, G. H., & Vickers, J. C. (1999). Neurochemical diversity of dystrophic neurites in the early and late stages of Alzheimer's disease. *Experimental Neurology*, *156*(1), 100–110.

Eltzschig, H. K., & Carmeliet, P. (2011). Hypoxia and Inflammation. *New England Journal of Medicine*, *364*(7), 656–665.

Elvidge, G. P., Glenny, L., Appelhoff, R. J., Ratcliffe, P. J., Ragoussis, J., & Gleadle, J. M. (2006). Concordant regulation of gene expression by hypoxia and 2-oxoglutarate-dependent dioxygenase inhibition: The role of HIF-1α, HIF-2α, and other pathways. *Journal of Biological Chemistry*, *281*(22), 15215–15226.

Escribese, M. M., Sierra-Filardi, E., Nieto, C., Samaniego, R., Sanchez-Torres, C., Matsuyama, T., … Corbi, A. L. (2012). The Prolyl Hydroxylase PHD3 Identifies

Proinflammatory Macrophages and Its Expression Is Regulated by Activin A. *The Journal of Immunology*, *189*(4), 1946–1954.

Farlow, M. R., Miller, M. L., & Pejovic, V. (2008). Treatment options in Alzheimer's disease: Maximizing benefit, managing expectations. *Dementia and Geriatric Cognitive Disorders*.

Felfly, H., Zambon, A., Xue, J., Muotri, A., Zhou, D., Snyder, E., & Haddad, G. (2011). Severe Hypoxia: Consequences to Neural Stem Cells and Neurons. *Journal of Neurology Research*, *1*(5), 177–189.

Finder, V. H., & Glockshuber, R. (2007). Amyloid-β aggregation. *Neurodegenerative Diseases*, *4*(1), 13–27.

Forsythe, J. A., Jiang, B. H., Iyer, N. V, Agani, F., Leung, S. W., Koos, R. D., & Semenza, G. L. (1996). Activation of vascular endothelial growth factor gene transcription by hypoxia-inducible factor 1. *Molecular and Cellular Biology*, *16*(9), 4604–4613.

Franco-Obregón, A., & López-Barneo, J. (1996). Differential oxygen sensitivity of calcium channels in rabbit smooth muscle cells of conduit and resistance pulmonary arteries. *Journal of Physiology*, *491*(2), 511–518.

Franklin, K. B. J., & Paxinos, G. (2008). *The Mouse Brain in Stereotaxic Coordinates*. *The Mouse Brain in Stereotaxic Coordinates* (3rd ed.). New York, NY: Academic Press.

Fukami, S., Watanabe, K., Iwata, N., Haraoka, J., Lu, B., Gerard, N. P., … Saido, T. C. (2002). Aβ-degrading endopeptidase, neprilysin, in mouse brain: Synaptic and axonal localization inversely correlating with Aβ pathology. *Neuroscience Research*, *43*(1), 39–56.

Funato, H., Yoshimura, M., Yamazaki, T., Saido, T. C., Ito, Y., Yokofujita, J., … Ihara, Y. (1998). Astrocytes containing amyloid beta-protein (Abeta)-positive granules are associated with Abeta40-positive diffuse plaques in the aged human brain. *The American Journal of Pathology*, *152*(4), 983–992.

Ganeshan, K., & Chawla, A. (2014). Metabolic Regulation of Immune Responses. *Annual Review of Immunology*, *32*(1), 609–634.

Gao, L., Tian, S., Gao, H., & Xu, Y. (2013). Hypoxia increases Aβ-induced tau phosphorylation by calpain and promotes behavioral consequences in AD transgenic mice. *Journal of Molecular Neuroscience*, *51*(1), 138–147.

Garcia-Alloza, M., Robbins, E. M., Zhang-Nunes, S. X., Purcell, S. M., Betensky, R. A., Raju, S., … Frosch, M. P. (2006). Characterization of amyloid deposition in the APPswe/PS1dE9 mouse model of Alzheimer disease. *Neurobiology of Disease*, *24*(3), 516–524.

Giannakopoulos, P., Herrmann, F. R., Bussière, T., Bouras, C., Kövari, E., Perl, D. P., … Hof, P. R. (2003). Tangle and neuron numbers, but not amyloid load, predict cognitive status in Alzheimer's disease. *Neurology*, *60*(9), 1495–1500.

Ginhoux, F., Greter, M., Leboeuf, M., Nandi, S., See, P., Gokhan, S., … Merad, M. (2010). Fate mapping analysis reveals that adult microglia derive from primitive macrophages. *Science (New York, N.Y.)*, *330*(6005), 841–845.

Ginouves, A., Ilc, K., Macias, N., Pouyssegur, J., & Berra, E. (2008). PHDs overactivation during chronic hypoxia "desensitizes" HIF and protects cells from necrosis. *Proceedings of the National Academy of Sciences*, *105*(12), 4745–4750.

Griciuc, A., Serrano-Pozo, A., Parrado, A. R., Lesinski, A. N., Asselin, C. N., Mullin, K., … Tanzi, R. E. (2013). Alzheimer's disease risk gene cd33 inhibits microglial uptake of amyloid beta. *Neuron*, *78*(4), 631–643.

Grimshaw, M. J., Wilson, J. L., & Balkwill, F. R. (2002). Endothelin-2 is a macrophage chemoattractant: Implications for macrophage distribution in tumors. *European Journal of Immunology*, *32*(9), 2393–2400.

Grocott, M. P. W., Martin, D. S., Levett, D. Z. H., McMorrow, R., Windsor, J., & Montgomery, H. E. (2009). Arterial Blood Gases and Oxygen Content in Climbers on Mount Everest. *New England Journal of Medicine*, *360*(2), 140–149.

Guglielmotto, M., Aragno, M., Autelli, R., Giliberto, L., Novo, E., Colombatto, S., … Tabaton, M. (2009). The up-regulation of BACE1 mediated by hypoxia and ischemic injury: role of oxidative stress and HIF1alpha. *Journal of Neurochemistry*, *108*(4), 1045–1056.

Guglielmotto, M., Tamagno, E., & Danni, O. (2009). Oxidative stress and hypoxia contribute to Alzheimer's disease pathogenesis: Two sides of the same coin. *TheScientificWorldJournal*, *9*, 781-791.

Guilliams, M., Ginhoux, F., Jakubzick, C., Naik, S. H., Onai, N., Schraml, B. U., … Yona, S. (2014). Dendritic cells, monocytes and macrophages: A unified nomenclature based on ontogeny. *Nature Reviews Immunology*. Nature Publishing Group, *14*, 571-578.

Guzy, R. D., & Schumacker, P. T. (2006). Oxygen sensing by mitochondria at complex III: The paradox of increased reactive oxygen species during hypoxia. In *Experimental Physiology*, *91*, 807–819.

Haass, C., Kaether, C., Thinakaran, G., & Sisodia, S. (2012). Trafficking and Proteolytic Processing of APP. *Cold Spring Harbor Perspectives in Medicine*, *2*, 1–26.

Haass, C., Lemere, C. A., Capell, A., Citron, M., Seubert, P., Schenk, D., … Selkoe, D. J. (1995). The Swedish mutation causes early-onset Alzheimer's disease by β-secretase cleavage within the secretory pathway. *Nature Medicine*, *1*(12), 1291–1296.

Haass, C., & Selkoe, D. J. (2007). Soluble protein oligomers in neurodegeneration: Lessons from the Alzheimer's amyloid β-peptide. *Nature Reviews Molecular Cell Biology*.

Hackett, P. H., & Roach, R. C. (2001). Current concepts: High-altitude illness. *The New England Journal of Medicine*, *345*(2), 107–114.

Hanisch, U. K., & Kettenmann, H. (2007, November 1). Microglia: Active sensor and versatile effector cells in the normal and pathologic brain. *Nature Neuroscience*, *10*, 1387-1394.

Hansen, D. V, Hanson, J. E., & Sheng, M. (2018). Microglia in Alzheimer's disease. *The Journal of Cell Biology*, *217*(2), 459–472.

Hardy, J. A., & Higgins, G. A. (1992). Alzheimer's Disease: The Amyloid Cascade Hypothesis. *Science*, *256*(5054), 184–185.

Hardy, J., Selkoe, D. J., Hardy1, J., & Selkoe2, D. J. (2002). The Amyloid Hypothesis of

Alzheimer's Disease: Progress and Problems on the Road to Therapeutics. *Science, 297,* 353-356.

Harris, A., Thompson, A., Whyte, M., & Walmsley, S. (2014). HIF-mediated innate immune responses: cell signaling and therapeutic implications. *Hypoxia*, *2*, 47–58.

Haschemi, A., Kosma, P., Gille, L., Evans, C. R., Burant, C. F., Starkl, P., … Wagner, O. (2012). The sedoheptulose kinase CARKL directs macrophage polarization through control of glucose metabolism. *Cell Metabolism*, *15*(6), 813–826.

Heneka, M. T., Kummer, M. P., Stutz, A., Delekate, A., Schwartz, S., Vieira-Saecker, A., … Golenbock, D. T. (2013). NLRP3 is activated in Alzheimer's disease and contributes to pathology in APP/PS1 mice. *Nature*, *493*(7434), 674–678.

Hernansanz-Agustín, P., Izquierdo-Álvarez, A., Sánchez-Gómez, F. J., Ramos, E., Villa-Piña, T., Lamas, S., … Martínez-Ruiz, A. (2014). Acute hypoxia produces a superoxide burst in cells. *Free Radical Biology and Medicine*, *71*, 146–156.

Herzenberg, L. a, Tung, J., Moore, W. a, Herzenberg, L. a, & Parks, D. R. (2006). Interpreting flow cytometry data: a guide for the perplexed. *Nature Immunology*, *7*(7), 681–685.

Hickman, S. E., Kingery, N. D., Ohsumi, T. K., Borowsky, M. L., Wang, L. C., Means, T. K., & El Khoury, J. (2013). The microglial sensome revealed by direct RNA sequencing. *Nature Neuroscience*, *16*(12), 1896–1905.

Howell, K., Ooi, H., Preston, R., & McLoughlin, P. (2004). Structural basis of hypoxic pulmonary hypertension: The modifying effect of chronic hypercapnia. *Experimental Physiology*, *89*(1), 66–72.

Hubbi, M. E., & Semenza, G. L. (2015). Regulation of cell proliferation by hypoxia-inducible factors. *American Journal of Physiology - Cell Physiology*, *309*(12), C775–C782.

Hunting, P. (2015). Alois Alzheimer (1864–1915). *Journal of Medical Biography*, *23*(4), 238–239.

Hwang, I. I. L., Watson, I. R., Der, S. D., & Ohh, M. (2006). Loss of VHL Confers Hypoxia-Inducible Factor (HIF)-Dependent Resistance to Vesicular Stomatitis

Virus: Role of HIF in Antiviral Response. *Journal of Virology*, *80*(21), 10712–10723.

Itagaki, S., McGeer, P. L., Akiyama, H., Zhu, S., & Selkoe, D. (1989). Relationship of microglia and astrocytes to amyloid deposits of Alzheimer disease. *Journal of Neuroimmunology*, *24*(3), 173–182.

Iturria-Medina, Y., Sotero, R. C., Toussaint, P. J., Mateos-Pérez, J. M., Evans, A. C., Weiner, M. W., … Furst, A. J. (2016). Early role of vascular dysregulation on late-onset Alzheimer's disease based on multifactorial data-driven analysis. *Nature Communications*, *7*, 11934.

Jaakkola, P. M., & Rantanen, K. (2013). The regulation, localization, and functions of oxygen-sensing prolyl hydroxylase PHD3. *Biological Chemistry*, *394*(4), 449–457.

Jackson, R. J., Rudinskiy, N., Herrmann, A. G., Croft, S., Kim, J. S. M., Petrova, V., … Spires-Jones, T. L. (2016). Human tau increases amyloid β plaque size but not amyloid β-mediated synapse loss in a novel mouse model of Alzheimer's disease. *European Journal of Neuroscience*, *44*(12), 3056–3066.

Jankowsky, J. L., Fadale, D. J., Anderson, J., Xu, G. M., Gonzales, V., Jenkins, N. A., … Borchelt, D. R. (2004, January). Mutant presenilins specifically elevate the levels of the 42 residue β-amyloid peptide in vivo: Evidence for augmentation of a 42-specific γ secretase. *Human Molecular Genetics*, *13*, 159-170.

Jankowsky, J. L., Slunt, H. H., Ratovitski, T., Jenkins, N. A., Copeland, N. G., & Borchelt, D. R. (2001). Co-expression of multiple transgenes in mouse CNS: A comparison of strategies. *Biomolecular Engineering*, *17*(6), 157–165.

Jeong, Y. H. (2006). Chronic stress accelerates learning and memory impairments and increases amyloid deposition in APPV717I-CT100 transgenic mice, an Alzheimer's disease model. *The FASEB Journal*, *20*(6), 729–731.

Jha, N. K., Jha, S. K., Kumar, D., Kejriwal, N., Sharma, R., Ambasta, R. K., & Kumar, P. (2015). Impact of insulin degrading enzyme and neprilysin in Alzheimer's disease biology: Characterization of putative cognates for therapeutic applications. *Journal of Alzheimer's Disease*, *48*(4), 891–917.

Jung, Y. J., Isaacs, J. S., Lee, S., Trepel, J., & Neckers, L. (2003). IL-1beta-mediated up-regulation of HIF-1alpha via an NFkappaB/COX-2 pathway identifies HIF-1 as a critical link between inflammation and oncogenesis. *The FASEB Journal : Official Publication of the Federation of American Societies for Experimental Biology*, *17*(14), 2115–2117.

Kaelin, W. G. (2005). Proline hydroxylation and gene expression. *Annual Review of Biochemistry*, *74*(1), 115–128.

Kaelin, W. G., & Ratcliffe, P. J. (2008). Oxygen Sensing by Metazoans: The Central Role of the HIF Hydroxylase Pathway. *Molecular Cell*. Cell Press, *30*, 393-402.

Kalaria, R. N. (2000). The role of cerebral ischemia in Alzheimer's disease. *Neurobiology of Aging*, *21*(2), 321–330.

Kamphuis, W., Orre, M., Kooijman, L., Dahmen, M., & Hol, E. M. (2012). Differential cell proliferation in the cortex of the APPswePS1dE9 Alzheimer's disease mouse model. *GLIA*, *60*(4), 615–629.

Kashani, A., Lepicard, È., Poirel, O., Videau, C., David, J. P., Fallet-Bianco, C., … El Mestikawy, S. (2008). Loss of VGLUT1 and VGLUT2 in the prefrontal cortex is correlated with cognitive decline in Alzheimer disease. *Neurobiology of Aging*, *29*(11), 1619–1630.

Kato, H., Takahasi, K., & Fujita, T. (2011). RIG-I-like receptors: Cytoplasmic sensors for non-self RNA. *Immunological Reviews*, *1*, 91-98.

Kay, D. W., Beamish, P., & Roth, M. (1964). Old age mental disorders in Newcastle-upon-Tyne. I. A study of prevalence. *The British Journal of Psychiatry : The Journal of Mental Science*, *110*, 146–158.

Keren-Shaul, H., Spinrad, A., Weiner, A., Matcovitch-Natan, O., Dvir-Szternfeld, R., Ulland, T. K., … Amit, I. (2017). A Unique Microglia Type Associated with Restricting Development of Alzheimer's Disease. *Cell*, *169*(7), 1276–1290.

Kerridge, C., Belyaev, N. D., Nalivaeva, N. N., & Turner, A. J. (2014). The Aβ-clearance protein transthyretin, like neprilysin, is epigenetically regulated by the amyloid precursor protein intracellular domain. *Journal of Neurochemistry*, *130*(3), 419–431.

Kerridge, C., Kozlova, D. I., Nalivaeva, N. N., & Turner, A. J. (2015). Hypoxia affects neprilysin expression through caspase activation and an APP intracellular domain-dependent mechanism. *Frontiers in Neuroscience*, *9*, 426.

Kiss, J., Mollenhauer, M., Walmsley, S. R., Kirchberg, J., Radhakrishnan, P., Niemietz, T., … Schneider, M. (2012). Loss of the Oxygen Sensor PHD3 Enhances the Innate Immune Response to Abdominal Sepsis. *The Journal of Immunology*, *189*(4), 1955–1965.

Kuhlicke, J., Frick, J. S., Morote-Garcia, J. C., Rosenberger, P., & Eltzschig, H. K. (2007). Hypoxia inducible factor (HIF)-1 coordinates induction of toll-like receptors TLR2 and TLR6 during hypoxia. *PLoS ONE*, *2*(12), e1364.

Kumar, A., Singh, A., & Ekavali. (2015). A review on Alzheimer's disease pathophysiology and its management: An update. *Pharmacological Reports*, *67*, 195-203.

Lazarov, O., Robinson, J., Tang, Y. P., Hairston, I. S., Korade-Mirnics, Z., Lee, V. M.-Y., … Sisodia, S. S. (2005). Environmental enrichment reduces Aβ levels and amyloid deposition in transgenic mice. *Cell*, *120*(5), 701–713.

Lee, C. Y. D., & Landreth, G. E. (2010). The role of microglia in amyloid clearance from the AD brain. *Journal of Neural Transmission*, *117*, 949-960.

Lee, P. H., Hwang, E. M., Hong, H. S., Boo, J. H., Mook-Jung, I., & Huh, K. (2006). Effect of ischemic neuronal insults on amyloid precursor protein processing. *Neurochemical Research*, *31*(6), 821–827.

Leek, R. D., Hunt, N. C., Landers, R. J., Lewis, C. E., Royds, J. A., & Harris, A. L. (2000). Macrophage infiltration is associated with VEGF and EGFR expression in breast cancer. *Journal of Pathology*, *190*(4), 430–436.

Leger, M., Quiedeville, A., Bouet, V., Boulouard, M., Schumann-Bard, P., & Freret, T. (2013). Object recognition test in mice. *Nature Protocols*, *8*, 2531-2537.

Li, L., Zhang, X., Yang, D., Luo, G., Chen, S., & Le, W. (2009). Hypoxia increases Aβ generation by altering β- and γ-cleavage of APP. *Neurobiology of Aging*, *30*(7), 1091–1098.

Lin, F. ching, & Young, H. A. (2014). Interferons: Success in anti-viral

immunotherapy. *Cytokine and Growth Factor Reviews*, *4*, 369-376.

Litvak, V., Ratushny, A. V., Lampano, A. E., Schmitz, F., Huang, A. C., Raman, A., … Aderem, A. (2012). A FOXO3–IRF7 gene regulatory circuit limits inflammatory sequelae of antiviral responses. *Nature*, *490*(7420), 421–425.

Liu, C., Cui, G., Zhu, M., Kang, X., & Guo, H. (2014). Neuroinflammation in Alzheimer's disease: Chemokines produced by astrocytes and chemokine receptors. *International Journal of Clinical and Experimental Pathology*, 7, 8342-8355.

Liu, H., Qiu, H., Yang, J., Ni, J., & Le, W. (2016). Chronic hypoxia facilitates Alzheimer's disease through demethylation of γ-secretase by downregulating DNA methyltransferase 3b. *Alzheimer's and Dementia*, *12*(2), 130–143.

Liu, J., Song, N., Tian, S., & Yu, J. (2014). Neuroepithelial body increases in bleomycin-treated mice. *Respiratory Physiology and Neurobiology*, *193*(1), 52–54.

Livak, K. J., & Schmittgen, T. D. (2001). Analysis of relative gene expression data using real-time quantitative PCR and the 2-ΔΔCT method. *Methods*, *25*(4), 402–408.

Lopez-Barneo, J., Pardal, R., & Ortega-Sáenz, P. (2001). Cellular Mechanisms of Oxygen Sensing. *Annu. Rev. Physiol*, *63*, 259–287.

Lucin, K. M., & Wyss-Coray, T. (2009). Immune Activation in Brain Aging and Neurodegeneration: Too Much or Too Little? *Neuron*, *64*(1), 110–122.

Mahmood, T., & Yang, P. C. (2012). Western blot: Technique, theory, and trouble shooting. *North American Journal of Medical Sciences*, *4*(9), 429–434.

Marsch, E., Sluimer, J. C., & Daemen, M. J. A. P. (2013). Hypoxia in atherosclerosis and inflammation. *Current Opinion in Lipidology*, *24*(5), 393–400.

Marshall, A. J., Rattray, M., & Vaughan, P. F. T. (2006). Chronic hypoxia in the human neuroblastoma SH-SY5Y causes reduced expression of the putative α-secretases, ADAM10 and TACE, without altering their mRNA levels. *Brain Research*, *1099*(1), 18–24.

Martin, S. B., Dowling, A. L. S., Lianekhammy, J., Lott, I. T., Doran, E., Murphy, M. P.,

… Head, E. (2014). Synaptophysin and synaptojanin-1 in down syndrome are differentially affected by Alzheimer's disease. *Journal of Alzheimer's Disease*, *42*(3), 767–775.

Mattson, M. P., Cheng, B., Davis, D., Bryant, K., Lieberburg, I., & Rydel, R. E. (1992). beta-Amyloid peptides destabilize calcium homeostasis and render human cortical neurons vulnerable to excitotoxicity. *The Journal of Neuroscience : The Official Journal of the Society for Neuroscience*, *12*(2), 376–389.

Metzen, E., Berchner-Pfannschmidt, U., Stengel, P., Marxsen, J. H., Stolze, I., Klinger, M., … Fandrey, J. (2003). Intracellular localisation of human HIF-1 alpha hydroxylases: implications for oxygen sensing. *Journal of Cell Science*, *116*, 1319–1326.

Moussavi Nik, S. H., Wilson, L., Newman, M., Croft, K., Mori, T. A., Musgrave, I., & Lardelli, M. (2012). The BACE1-PSEN-AβPP regulatory axis has an ancient role in response to low oxygen/oxidative stress. *Journal of Alzheimer's Disease*, *28*(3), 515–530.

Murphy, E., & Steenbergen, C. (2008). Mechanisms Underlying Acute Protection From Cardiac Ischemia-Reperfusion Injury. *Physiological Reviews*, *88*(2), 581–609.

Nanduri, J., & Nanduri, R. P. (2007). Cellular mechanisms associated with intermittent hypoxia. *Essays In Biochemistry*, *43*, 91–104.

Nayak, D., Roth, T. L., & McGavern, D. B. (2014). Microglia Development and Function. *Annual Review of Immunology*, *32*(1), 367–402.

Neuropathology Group. Medical Research Council Cognitive Function and Aging Study. (2001). Pathological correlates of late-onset dementia in a multicentre, community-based population in England and Wales. *Lancet*, *357*(9251), 169–175.

Nhan, H. S., Chiang, K., & Koo, E. H. (2015, January). The multifaceted nature of amyloid precursor protein and its proteolytic fragments: friends and foes. *Acta Neuropathologica*, *1*, 1-19.

Nicotra, L., Loram, L. C., Watkins, L. R., & Hutchinson, M. R. (2012). Toll-like

receptors in chronic pain. *Experimental Neurology*, *2*, 316-329.

Nimmerjahn, A., Kirchhoff, F., & Helmchen, F. (2005). Resting microglial cells are highly dynamic surveillants of brain parenchyma in vivo. *Science*, *308*(5726), 1314–1318.

Nolan, T., Hands, R. E., & Bustin, S. A. (2006). Quantification of mRNA using real-time RT-PCR. *Nature Protocols*, *1*(3), 1559–1582.

O'Connor, T., Sadleir, K. R., Maus, E., Velliquette, R. A., Zhao, J., Cole, S. L., … Vassar, R. (2008). Phosphorylation of the Translation Initiation Factor eIF2α Increases BACE1 Levels and Promotes Amyloidogenesis. *Neuron*, *60*(6), 988–1009.

Okun, E., Griffioen, K. J., & Mattson, M. P. (2011). Toll-like receptor signaling in neural plasticity and disease. *Trends in Neurosciences*, *34*(5), 269–281.

Olmos-Alonso, A., Schetters, S. T. T., Sri, S., Askew, K., Mancuso, R., Vargas-Caballero, M., … Gomez-Nicola, D. (2016). Pharmacological targeting of CSF1R inhibits microglial proliferation and prevents the progression of Alzheimer's-like pathology. *Brain*, *139*(3), 891–907.

Orre, M., Kamphuis, W., Osborn, L. M., Jansen, A. H. P., Kooijman, L., Bossers, K., & Hol, E. M. (2014). Isolation of glia from Alzheimer's mice reveals inflammation and dysfunction. *Neurobiology of Aging*, *35*, 2746–2760.

Orre, M., Kamphuis, W., Osborn, L. M., Melief, J., Kooijman, L., Huitinga, I., … Hol, E. M. (2014). Acute isolation and transcriptome characterization of cortical astrocytes and microglia from young and aged mice. *Neurobiology of Aging*, *35*(1), 1–14.

Ortiz-Barahona, A., Villar, D., Pescador, N., Amigo, J., & del Peso, L. (2010). Genome-wide identification of hypoxia-inducible factor binding sites and target genes by a probabilistic model integrating transcription-profiling data and in silico binding site prediction. *Nucleic Acids Research*, *38*(7), 2332–2345.

Osborn, O., & Olefsky, J. M. (2012). The cellular and signaling networks linking the immune system and metabolism in disease. *Nature Medicine*, 18, 363-374.

Palazon, A., Goldrath, A. W., Nizet, V., & Johnson, R. S. (2014). HIF Transcription

Factors, Inflammation, and Immunity. *Immunity*, *41*, 518-528.

Parathath, S., Mick, S. L., Feig, J. E., Joaquin, V., Grauer, L., Habiel, D. M., … Fisher, E. A. (2011). Hypoxia is present in murine atherosclerotic plaques and has multiple adverse effects on macrophage lipid metabolism. *Circulation Research*, *109*(10), 1141–1152.

Park, S. A., Shaked, G. M., Bredesen, D. E., & Koo, E. H. (2009). Mechanism of cytotoxicity mediated by the C31 fragment of the amyloid precursor protein. *Biochemical and Biophysical Research Communications*, *388*(2), 450–455.

Patel, S. A., & Simon, M. C. (2008, April). Biology of hypoxia-inducible factor-2α in development and disease. *Cell Death and Differentiation*, 15, 628-634.

Peng Yuan, C. C., C. Dirk Keene, ..., M. C., & David Baddeley, J. G. (2016). TREM2 Haplodeficiency in Mice and Humans Impairs the Microglia Barrier Function Leading to Decreased Amyloid Compaction and Severe Axonal Dystrophy. *Neuron*, *92*, 252-264.

Peyssonnaux, C., Datta, V., Cramer, T., Doedens, A., Theodorakis, E. A., Gallo, R. L., … Johnson, R. S. (2005). HIF-1α expression regulates the bactericidal capacity of phagocytes. *Journal of Clinical Investigation*, *115*(7), 1806–1815.

Philpott, D. J., Sorbara, M. T., Robertson, S. J., Croitoru, K., & Girardin, S. E. (2014). NOD proteins: Regulators of inflammation in health and disease. *Nature Reviews Immunology*, *14*, 9-23.

Pimenova, A. A., Raj, T., & Goate, A. M. (2018). Untangling Genetic Risk for Alzheimer's Disease. *Biological Psychiatry, 83,* 300-310.

Pooler, A. M., Noble, W., & Hanger, D. P. (2014,). A role for tau at the synapse in Alzheimer's disease pathogenesis. *Neuropharmacology*, *76*, 1-8.

Rangaraju, S., Raza, S. A., Li, N. X., Betarbet, R., Dammer, E. B., Duong, D., … Levey, A. I. (2018). Differential Phagocytic Properties of CD45low Microglia and CD45high Brain Mononuclear Phagocytes—Activation and Age-Related Effects. *Frontiers in Immunology*, *9*, 405.

Ransohoff, R. M., & Perry, V. H. (2009). Microglial Physiology: Unique Stimuli, Specialized Responses. *Annual Review of Immunology*, *27*(1), 119–145.

Reitz, C., & Mayeux, R. (2014). Alzheimer disease: Epidemiology, diagnostic criteria, risk factors and biomarkers. *Biochemical Pharmacology*, *8*, 640-651.

Riboldi, E., Porta, C., Morlacchi, S., Viola, A., Mantovani, A., & Sica, A. (2013). Hypoxia-mediated regulation of macrophage functions in pathophysiology. *International Immunology*, *25*(2), 67–75.

Rio-Hortega, P. (1919). El tercer elemento "de los centros nerviosos. I. La microglia en estado normal. II. Intervención de la microglia en los procesos patológicos. III. Naturaleza probable de la microglia. *Biol. Madrid*, *VIII*, 69–120.

Rius, J., Guma, M., Schachtrup, C., Akassoglou, K., Zinkernagel, A. S., Nizet, V., … Karin, M. (2008). NF-κB links innate immunity to the hypoxic response through transcriptional regulation of HIF-1α. *Nature*, *453*(7196), 807–811.

Rock, K. L., Latz, E., Ontiveros, F., & Kono, H. (2010). The Sterile Inflammatory Response. *Annual Review of Immunology*, *28*(1), 321–342.

Rodriguez, J., Pilkington, R., Garcia Munoz, A., Nguyen, L. K., Rauch, N., Kennedy, S., … von Kriegsheim, A. (2016). Substrate-Trapped Interactors of PHD3 and FIH Cluster in Distinct Signaling Pathways. *Cell Reports*, *14*(11), 2745–2760.

Rovelet-Lecrux, A., Hannequin, D., Raux, G., Le Meur, N., Laquerrière, A., Vital, A., … Campion, D. (2006). APP locus duplication causes autosomal dominant early-onset Alzheimer disease with cerebral amyloid angiopathy. *Nature Genetics*, *38*(1), 24–26.

Rusanen, M., Ngandu, T., Laatikainen, T., Tuomilehto, J., Soininen, H., & Kivipelto, M. (2013). Chronic obstructive pulmonary disease and asthma and the risk of mild cognitive impairment and dementia: a population based CAIDE study. *Current Alzheimer Research*, *10*(5), 549–555.

Saido, T., & Leissring, M. A. (2012). Proteolytic degradation of amyloid-β protein. *Cold Spring Harbor Perspectives in Medicine*, *2*(6), a006379.

Schindelin, J., Arganda-Carreras, I., Frise, E., Kaynig, V., Longair, M., Pietzsch, T., … Cardona, A. (2012). Fiji: an open-source platform for biological-image analysis. *Nature Methods*, *9*(7), 676–682.

Schneider, J. A., Arvanitakis, Z., Bang, W., & Bennett, D. A. (2007). Mixed brain

pathologies account for most dementia cases in community-dwelling older persons. *Neurology*, *69*(24), 2197–2204.

Schödel, J., Mole, D. R., & Ratcliffe, P. J. (2013). Pan-genomic binding of hypoxia-inducible transcription factors. *Biological Chemistry*, *394*, 507-517.

Schödel, J., Oikonomopoulos, S., Ragoussis, J., Pugh, C. W., Ratcliffe, P. J., & Mole, D. R. (2011). High-resolution genome-wide mapping of HIF-binding sites by ChIP-seq. *Blood*, *117*(23), e207-17.

Schofield, C. J., & Ratcliffe, P. J. (2004, May 1). Oxygen sensing by HIF hydroxylases. *Nature Reviews Molecular Cell Biology*, *5*, 343-354.

Schreier, D. A., Hacker, T. A., Hunter, K., Eickoff, J., Liu, A., Song, G., & Chesler, N. (2014). Impact of increased hematocrit on right ventricular afterload in response to chronic hypoxia. *Journal of Applied Physiology*, *117*(8), 833–839.

Schuster, S. J., Badiavas, E. V, Costa-Giomi, P., Weinmann, R., Erslev, A. J., & Caro, J. (1989). Stimulation of erythropoietin gene transcription during hypoxia and cobalt exposure. *Blood*, *73*(1), 13–16.

Selkoe, D., & Dennis, J. (2003, November). Aging, Amyloid, and Alzheimer's Disease: A Perspective in Honor of Carl Cotman. *Neurochemical Research*.

Selkoe, D. J. (2001). Alzheimer's Disease: Genes, Proteins, and Therapy. *Physiological Reviews*, *81*(2), 741–766.

Semenza, G. L. (2012). Hypoxia-inducible factors in physiology and medicine. *Cell*, *3*, 399-408.

Semenza, G. L., Nejfelt, M. K., Chi, S. M., & Antonarakis, S. E. (1991). Hypoxia-inducible nuclear factors bind to an enhancer element located 3' to the human erythropoietin gene. *Proceedings of the National Academy of Sciences*, *88*(13), 5680–5684.

Semenza, G. L., Roth, P. H., Fang, H. M., & Wang, G. L. (1994). Transcriptional regulation of genes encoding glycolytic enzymes by hypoxia-inducible factor 1. *The Journal of Biological Chemistry*, *269*(38), 23757–23763.

Serrano-Pozo, A., Frosch, M. P., Masliah, E., & Hyman, B. T. (2011). Neuropathological alterations in Alzheimer disease. *Cold Spring Harbor*

Perspectives in Medicine, *1*(1), a006189.

Serrano-Pozo, A., Gómez-Isla, T., Growdon, J. H., Frosch, M. P., & Hyman, B. T. (2013). A phenotypic change but not proliferation underlies glial responses in Alzheimer disease. *American Journal of Pathology*, *182*(6), 2332–2344.

Serrano-Pozo, A., Muzikansky, A., Gómez-Isla, T., Growdon, J. H., Betensky, R. A., Frosch, M. P., & Hyman, B. T. (2013). Differential relationships of reactive astrocytes and microglia to fibrillar amyloid deposits in alzheimer disease. *Journal of Neuropathology and Experimental Neurology*, *72*(6), 462–471.

Serrano-Pozo, A., Sánchez-García, M. A., Heras-Garvín, A., March-Díaz, R., Navarro, V., Vizuete, M., … Pascual, A. (2017). Acute and Chronic Sustained Hypoxia Do Not Substantially Regulate Amyloid-β Peptide Generation In Vivo. *PLoS ONE*, *12*(1), 1-17.

Shankar, G. M., & Walsh, D. M. (2009). Alzheimer's disease: Synaptic dysfunction and Aβ. *Molecular Neurodegeneration*, *4*(1), 1-13.

Shima, D. T., Adamis, A. P., Ferrara, N., Yeo, K. T., Yeo, T. K., Allende, R., … D'Amore, P. A. (1995). Hypoxic induction of endothelial cell growth factors in retinal cells: identification and characterization of vascular endothelial growth factor (VEGF) as the mitogen. *Mol Med*, *1*(2), 182–193.

Shiota, S., Takekawa, H., Matsumoto, S. E., Takeda, K., Nurwidya, F., Yoshioka, Y., … Takahashi, K. (2013). Chronic intermittent hypoxia/reoxygenation facilitate amyloid-β generation in mice. *Journal of Alzheimer's Disease*, *37*(2), 325–333.

Silvola, J. M. U., Saraste, A., Forsback, S., Laine, V. J. O., Saukko, P., Heinonen, S. E., … Knuuti, J. (2011). Detection of hypoxia by [18F]EF5 in atherosclerotic plaques in mice. *Arteriosclerosis, Thrombosis, and Vascular Biology*, *31*(5), 1011–1015.

Singh, B., Mielke, M. M., Parsaik, A. K., Cha, R. H., Roberts, R. O., Scanlon, P. D., … Petersen, R. C. (2014). A prospective study of chronic obstructive pulmonary disease and the risk for mild cognitive impairment. *JAMA Neurology*, *71*(5), 581–588.

Sisodia, S. S. (1992). Beta-amyloid precursor protein cleavage by a membrane-bound protease. *Proceedings of the National Academy of Sciences of the United*

States of America, *89*(13), 6075–6079.

Smith, I. F., Boyle, J. P., Green, K. N., Pearson, H. A., & Peers, C. (2004). Hypoxic remodelling of Ca2+ mobilization in type I cortical astrocytes: involvement of ROS and pro-amyloidogenic APP processing. *Journal of Neurochemistry*, *88*(4), 869–877.

St-Pierre, J., & Ostergaard, H. L. (2013). A Role for the Protein Tyrosine Phosphatase CD45 in Macrophage Adhesion through the Regulation of Paxillin Degradation. *PLoS ONE*, *8*(7), e71531.

St George-Hyslop, P., Tanzi, R., Polinsky, R., Haines, J., Nee, L., Watkins, P., … Al., E. (1987). The genetic defect causing familial Alzheimer's disease maps on chromosome 21. *Science*, *235*(4791), 885–890.

Strassnig, M., & Ganguli, M. (2005). About a Peculiar Disease of the Cerebral Cortex : Alzheimer's Original Case. *Psychiatry (Edgmont)*, *2*(9), 30–33.

Strehl, C., Fangradt, M., Fearon, U., Gaber, T., Buttgereit, F., & Veale, D. J. (2014). Hypoxia: how does the monocyte-macrophage system respond to changes in oxygen availability? *Journal of Leukocyte Biology*, *95*(2), 233–241.

Streit, W. J., Xue, Q. S., Tischer, J., & Bechmann, I. (2014). Microglial pathology. *Acta Neuropathologica Communications*, *2*(1), 142.

Su, J. H., Cummings, B. J., & Cotman, C. W. (1993). Identification and distribution of axonal dystrophic neurites in Alzheimer's disease. *Brain Research*, *625*(2), 228–237.

Su, J. H., Cummings, B. J., & Cotman, C. W. (1996). Plaque biogenesis in brain aging and Alzheimer's disease. II. Progressive transformation and developmental sequence of dystrophic neurites. *Brain Research*, *739*(1–2), 79–87.

Sun, X., He, G., Qing, H., Zhou, W., Dobie, F., Cai, F., … Song, W. (2006). Hypoxia facilitates Alzheimer's disease pathogenesis by up-regulating BACE1 gene expression. *Proceedings of the National Academy of Sciences*, *103*(49), 18727–18732.

Swain, L., Wottawa, M., Hillemann, A., Beneke, A., Odagiri, H., Terada, K., … Katschinski, D. M. (2014). Prolyl-4-hydroxylase domain 3 (PHD3) is a critical

terminator for cell survival of macrophages under stress conditions. *Journal of Leukocyte Biology*, *96*(3), 365–375.

Tamagno, E., Guglielmotto, M., Aragno, M., Borghi, R., Autelli, R., Giliberto, L., … Tabaton, M. (2008). Oxidative stress activates a positive feedback between the γ- and β-secretase cleavages of the β-amyloid precursor protein. *Journal of Neurochemistry*, *104*(3), 683–695.

Tarasoff-Conway, J. M., Carare, R. O., Osorio, R. S., Glodzik, L., Butler, T., Fieremans, E., … de Leon, M. J. (2015). Clearance systems in the brain—implications for Alzheimer disease. *Nature Reviews Neurology*, *11*(8), 457–470.

Tátrai, E., Bartal, A., Gacs, A., Paku, S., Kenessey, I., Garay, T., … József Tóvári, A. (2017). Cell type-dependent HIF1α-mediated effects of hypoxia on proliferation, migration and metastatic potential of human tumor cells. *Oncotarget*, *8*(27), 44498–44510.

Taylor, C. T. (2008, September 1). Interdependent roles for hypoxia inducible factor and nuclear factor-κB in hypoxic inflammation. *Journal of Physiology*. Wiley/Blackwell (10.1111).

Tesco, G., Koh, Y. H., Kang, E. L., Cameron, A. N., Das, S., Sena-Esteves, M., … Tanzi, R. E. (2007). Depletion of GGA3 Stabilizes BACE and Enhances β-Secretase Activity. *Neuron*, *54*(5), 721–737.

Tu, S., Okamoto, S., Lipton, S. A., & Xu, H. (2014). Oligomeric Aβ-induced synaptic dysfunction in Alzheimer's disease. *Molecular Neurodegeneration*, *9*(1), 48.

Van Raamsdonk, J. M. (2015). Levels and location are crucial in determining the effect of ROS on lifespan. *Worm*, *4*(4), e1094607.

van Uden, P., Kenneth, N. S., & Rocha, S. (2008). Regulation of hypoxia-inducible factor-1α by NF-κB. *Biochemical Journal*, *412*(3), 477–484.

Vassar, R., Bennett, B. D., Babu-Khan, S., Kahn, S., Mendiaz, E. A., Denis, P., … Citron, M. (1999). β-Secretase cleavage of Alzheimer's amyloid precursor protein by the transmembrane aspartic protease BACE. *Science*, *286*(5440), 735–741.

Walker, J. M., Fowler, S. W., Miller, D. K., Sun, A. Y., Weisman, G. A., Wood, W. G., … Schachtman, T. R. (2011). Spatial learning and memory impairment and

increased locomotion in a transgenic amyloid precursor protein mouse model of Alzheimer's disease. *Behavioural Brain Research*, *222*, 169–175.

Walmsley, S. R., Chilvers, E. R., Thompson, A. A., Vaughan, K., Marriott, H. M., Parker, L. C., … Whyte, M. K. B. (2011). Prolyl hydroxylase 3 (PHD3) is essential for hypoxic regulation of neutrophilic inflammation in humans and mice. *The Journal of Clinical Investigation*, *121*(3), 1053–1063.

Walmsley, S. R., Print, C., Farahi, N., Peyssonnaux, C., Johnson, R. S., Cramer, T., … Chilvers, E. R. (2005). Hypoxia-induced neutrophil survival is mediated by HIF-1α–dependent NF-κB activity. *The Journal of Experimental Medicine*, *201*(1), 105–115.

Walsh, D. M., & Selkoe, D. J. (2007). Aβ oligomers - A decade of discovery. *Journal of Neurochemistry*, *101*(5), 1172–1184.

Wang, R., Zhang, Y. W., Zhang, X., Liu, R., Zhang, X., Hong, S., … Xu, H. (2006). Transcriptional regulation of APH-1A and increased gamma-secretase cleavage of APP and Notch by HIF-1 and hypoxia. *The FASEB Journal : Official Publication of the Federation of American Societies for Experimental Biology*, *20*(8), 1275–1277.

Wang, V., Davis, D. A., Haque, M., Huang, L. E., & Yarchoan, R. (2005). Differential gene up-regulation by hypoxia-inducible factor-1 alpha and hypoxia-inducible factor-2 alpha in HEK293T cells. *Cancer Research*, *65*(8), 3299–3306.

Wang, Y., Cella, M., Mallinson, K., Ulrich, J. D., Young, K. L., Robinette, M. L., … Colonna, M. (2015). TREM2 lipid sensing sustains the microglial response in an Alzheimer's disease model. *Cell*, *160*(6), 1061–1071.

Wang, Y., Ulland, T. K., Ulrich, J. D., Song, W., Tzaferis, J. A., Hole, J. T., … Colonna, M. (2016). TREM2-mediated early microglial response limits diffusion and toxicity of amyloid plaques. *The Journal of Experimental Medicine*, *213*(5), 667–675.

Webster, N. J., Green, K. N., Peers, C., & Vaughan, P. F. T. (2002). Altered processing of amyloid precursor protein in the human neuroblastoma SH-SY5Y by chronic hypoxia. *Journal of Neurochemistry*, *83*(6), 1262–1271.

Webster, N. J., Green, K. N., Settle, V. J., Peers, C., & Vaughan, P. F. T. (2004). Altered processing of the amyloid precursor protein and decreased expression of ADAM 10 by chronic hypoxia in SH-SY5Y: No role for the stress-activated JNK and p38 signalling pathways. *Molecular Brain Research*, *130*(1–2), 161–169.

Weir, E. K., & Archer, S. L. (1995). The mechanism of acute hypoxic pulmonary vasoconstriction: the tale of two channels. *The FASEB Journal : Official Publication of the Federation of American Societies for Experimental Biology*, *9*(2), 183–189.

Wilson, M. H., Newman, S., & Imray, C. H. (2009). The cerebral effects of ascent to high altitudes. *The Lancet Neurology*, *8*, 175-191.

Worzfeld, T., & Offermanns, S. (2014). Semaphorins and plexins as therapeutic targets. *Nature Reviews Drug Discovery*, *13*(8), 603–621.

Wyss-Coray, T., Loike, J. D., Brionne, T. C., Lu, E., Anankov, R., Yan, F., … Husemann, J. (2003). Adult mouse astrocytes degrade amyloid-β in vitro and in situ. *Nature Medicine*, *9*(4), 453–457.

Yaffe, K., Laffan, A. M., Harrison, S. L., Redline, S., Spira, A. P., Ensrud, K. E., … Stone, K. L. (2011). Sleep-disordered breathing, hypoxia, and risk of mild cognitive impairment and dementia in older women. *JAMA - Journal of the American Medical Association*, *306*(6), 613–619.

Yan, R., Blenkowski, M. J., Shuck, M. E., Miao, H., Tory, M. C., Pauley, A. M., … Gurney, M. E. (1999). Membrane-anchored aspartyl protease with Alzheimer's disease β- secretase activity. *Nature*, *402*(6761), 533–537.

Yu, J.-T., Tan, L., & Hardy, J. (2014). Apolipoprotein E in Alzheimer's Disease: An Update. *Annual Review of Neuroscience*, *37*(1), 79–100.

Yuan, P., Condello, C., Keene, C. D., Wang, Y., Bird, T. D., Paul, S. M., … Grutzendler, J. (2016). TREM2 Haplodeficiency in Mice and Humans Impairs the Microglia Barrier Function Leading to Decreased Amyloid Compaction and Severe Axonal Dystrophy. *Neuron, 92*, 252-264.

Zeisel, A., Moz-Manchado, A. B., Codeluppi, S., Lönnerberg, P., Manno, G. La, Juréus, A., … Linnarsson, S. (2015). Cell types in the mouse cortex and hippocampus

revealed by single-cell RNA-seq. *Science*, *347*(6226), 1138–1142.

Zhang, X., Li, L., Zhang, X., Xie, W., Li, L., Yang, D., … Le, W. (2013). Prenatal hypoxia may aggravate the cognitive impairment and Alzheimer's disease neuropathology in APPSwe/PS1A246Etransgenic mice. *Neurobiology of Aging*, *34*(3), 663–678.

Zhang, X., Zhou, K., Wang, R., Cui, J., Lipton, S. A., Liao, F. F., … Zhang, Y. W. (2007). Hypoxia-inducible factor 1α (HIF-1α)-mediated hypoxia increases BACE1 expression and β-amyloid generation. *Journal of Biological Chemistry*, *282*(15), 10873–10880.

Zhang, Y., Thompson, R., Zhang, H., & Xu, H. (2011). APP processing in Alzheimer's disease. *Molecular Brain*, *4*(1), 3.

Zheng, H., & Koo, E. H. (2006, July 3). The amyloid precursor protein: Beyond amyloid. *Molecular Neurodegeneration*, *1*, 1-5.

Zhou, J., Schmid, T., & Brüne, B. (2003). Tumor Necrosis Factor- Causes Accumulation of a Ubiquitinated Form of Hypoxia Inducible Factor-1 through a Nuclear Factor- B-Dependent Pathway. *Molecular Biology of the Cell*, *14*(6), 2216–2225.

Zhu, Y., Hou, H., Rezai-Zadeh, K., Giunta, B., Ruscin, A., Gemma, C., … Tan, J. (2011). CD45 deficiency drives amyloid-β peptide oligomers and neuronal loss in Alzheimer's disease mice. *The Journal of Neuroscience : The Official Journal of the Society for Neuroscience*, *31*(4), 1355–1365.

Zinkernagel, A. S., Johnson, R. S., & Nizet, V. (2007). Hypoxia inducible factor (HIF) function in innate immunity and infection. *Journal of Molecular Medicine*, *85,* 1339-1346.

Zlokovic, B. V., Yamada, S., Holtzman, D., Ghiso, J., & Frangione, B. (2000). Clearance of amyloid beta-peptide from brain: transport or metabolism? *Nature Medicine*, *6*(7), 718–719.

9. Attached material

9.1. Table 5

Table 5. Differentially expressed genes in microglia from *Egln3 $^{-/-}$; App-Psen1 versus App-Psen1* mice.

Gene name/loci	logFC	linealFC	P.Value
Mamdc2	2,13	4,39	0,00009
Prkd1	2,02	4,05	0,00000
H2-Eb1	1,99	3,96	0,00009
Postn	1,98	3,95	0,00003
Dkk2	1,81	3,51	0,00018
Gdpd3	1,76	3,38	0,00007
Cxcl14	1,54	2,92	0,00009
Ly6k	1,45	2,74	0,00010
D630028G08Rik	1,43	2,70	0,04255
Lgi2	1,42	2,68	0,01549
Ctnna3	1,41	2,65	0,00216
Gpnmb	1,36	2,57	0,02569
H2-Ab1	1,36	2,57	0,00019
Spp1	1,35	2,56	0,00611
Flt1	1,29	2,44	0,00007
Lpl	1,26	2,39	0,00006
BC018473	1,25	2,37	0,00237
Klrb1a	1,22	2,33	0,01011
Pianp	1,22	2,33	0,00001
Abi3bp	1,22	2,32	0,04246
H2-Aa	1,22	2,32	0,00051
Gm13669	1,18	2,27	0,00604
Trpc4	1,16	2,24	0,00012
Cd74	1,11	2,16	0,00021
Colec12	1,10	2,15	0,00431
Slc41a2	1,10	2,15	0,00027
Tgfb2	1,09	2,13	0,00310
Fn1	1,07	2,10	0,00390
Cspg4	1,07	2,09	0,00116
Actr3b	1,07	2,09	0,00126
Cxcl13	1,05	2,07	0,01451
Plp2	1,03	2,05	0,00294
Gm6166	1,03	2,04	0,00029
Fam189a2	1,02	2,03	0,00074
Fam19a2	1,02	2,03	0,01948

Ahr	1,02	2,03	0,00007
Gm14328	1,00	2,01	0,00011
Sh3pxd2b	0,99	1,99	0,00250
Fabp5	0,97	1,96	0,00019
Fabp5l2	0,97	1,96	0,00030
Gm6100	0,95	1,93	0,00001
Alcam	0,94	1,92	0,00064
Gm3601	0,94	1,92	0,00077
Tmem163	0,93	1,90	0,00006
Atp6v0d2	0,92	1,89	0,01671
Gm5423	0,91	1,87	0,00238
Yipf7	0,90	1,86	0,00228
Perp	0,89	1,86	0,00024
Elovl7	0,88	1,84	0,00137
Gm13998	0,88	1,84	0,00030
Sulf2	0,88	1,84	0,00074
Fbln5	0,87	1,83	0,00008
Adssl1	0,86	1,82	0,00166
Mxra8	0,86	1,82	0,00692
Msr1	0,85	1,81	0,01291
Agap1	0,84	1,79	0,00072
Hal	0,83	1,78	0,00012
Fxyd6	0,82	1,77	0,00487
Olr1	0,81	1,75	0,00372
St8sia6	0,80	1,74	0,00152
Plxna2	0,80	1,74	0,03748
Igfbp5	0,80	1,74	0,01142
Mrc2	0,80	1,74	0,00244
Cxcr4	0,79	1,73	0,01018
Lgals1	0,79	1,73	0,01309
Ptprg	0,78	1,72	0,01286
Gm25911	0,78	1,72	0,00011
Cacnb4	0,77	1,71	0,00847
Gm14584	0,77	1,70	0,00244
Wdr35	0,76	1,70	0,00021
Plxnc1	0,75	1,68	0,00142
Galc	0,74	1,67	0,00012
Gm25732	0,73	1,66	0,00037
Clec7a	0,72	1,65	0,00543
Tmem176a	0,72	1,65	0,00009
Vegfa	0,71	1,64	0,00177
Fyn	0,71	1,64	0,00400
Efr3b	0,71	1,63	0,00222
Kif1a	0,71	1,63	0,00392
Atp1a3	0,70	1,63	0,00094
Fndc4	0,70	1,63	0,00104

Igsf10	0,70	1,63	0,02138
Rnf128	0,70	1,63	0,00157
Gm19386	0,70	1,62	0,00257
Gpr81	0,69	1,62	0,00223
5430435G22Rik	0,68	1,60	0,01909
Gm11166	0,68	1,60	0,02907
Gas7	0,68	1,60	0,00274
Itgax	0,67	1,59	0,00163
AI504432	0,66	1,58	0,00949
Ephx1	0,66	1,58	0,00398
Ank	0,65	1,57	0,00074
Asb10	0,65	1,57	0,00009
Tmem176b	0,64	1,56	0,00032
Laptm4a	0,64	1,56	0,00010
Zfp618	0,63	1,55	0,00200
Galns	0,63	1,55	0,00043
Arap2	0,63	1,55	0,00195
Fgf13	0,63	1,55	0,00043
Etl4	0,63	1,55	0,00213
Crip1	0,63	1,55	0,00149
Ccr2	0,63	1,55	0,03799
Chst11	0,63	1,54	0,00050
Wif1	0,63	1,54	0,00965
Maoa	0,62	1,54	0,00110
n-R5s54	0,62	1,53	0,02924
Fam214a	0,62	1,53	0,00022
Vim	0,61	1,53	0,01223
Rasd1	0,61	1,53	0,00074
Procr	0,61	1,52	0,00171
Myo5a	0,61	1,52	0,00609
Emp2	0,60	1,52	0,00383
Ighv1-69	0,60	1,52	0,00863
Gm24245	0,60	1,51	0,00070
Gm24270	0,60	1,51	0,00070
Gm24187	0,60	1,51	0,00054
Gm26993	0,60	1,51	0,00994
Gm26214	0,60	1,51	0,02184
Apoc1	0,59	1,51	0,02315
Bambi	0,59	1,51	0,00789
Cers4	0,59	1,51	0,00076
Usp30	0,59	1,50	0,00123
Wfdc17	0,59	1,50	0,02544
Gm8034	0,58	1,50	0,00685
Leprel4	0,58	1,50	0,00105
Naaa	0,58	1,50	0,00227
Pdcd1	0,58	1,49	0,00729

Gm3788	0,58	1,49	0,00162
Slc44a1	0,57	1,49	0,00166
Gm23388	0,57	1,49	0,00047
Arnt2	0,57	1,49	0,01024
Nr4a2	0,57	1,48	0,00282
Iqcg	0,57	1,48	0,00196
Gm15418	0,57	1,48	0,02237
Lama3	0,57	1,48	0,00510
Ppap2a	0,56	1,48	0,00329
Arrdc4	0,56	1,48	0,00304
Rai14	0,56	1,48	0,00237
Gpx3	0,55	1,46	0,04271
Selm	0,55	1,46	0,00429
Tmem203	0,55	1,46	0,00168
Acp5	0,55	1,46	0,00438
Mcam	0,54	1,46	0,00569
Gm25554	0,54	1,46	0,00362
Lyzl4	0,54	1,45	0,03060
Ipcef1	0,53	1,45	0,00864
Fmr1nb	0,53	1,45	0,01723
A830039N20Rik	0,53	1,44	0,00578
F2r	0,53	1,44	0,00078
Dapk1	0,53	1,44	0,00543
Tbc1d4	0,53	1,44	0,00163
Kcnk3	0,52	1,44	0,00053
Prr15	0,52	1,44	0,02006
Arg2	0,52	1,44	0,00642
Olfr152	0,52	1,44	0,01459
St14	0,52	1,44	0,00509
Hdac9	0,52	1,44	0,00210
Sycp3	0,52	1,44	0,03402
Gramd3	0,52	1,43	0,00078
Crtap	0,52	1,43	0,00856
S100a1	0,52	1,43	0,00930
Gyg	0,52	1,43	0,00613
Rgs1	0,52	1,43	0,01377
Ptn	0,52	1,43	0,02694
Mptx1	0,51	1,43	0,03055
Pvrl1	0,51	1,42	0,02228
Maged1	0,51	1,42	0,00090
Mt2	0,51	1,42	0,00216
Naglu	0,51	1,42	0,02009
Cd34	0,50	1,42	0,00971
Fabp3-ps1	0,50	1,42	0,01169
mmu-mir-6398	0,50	1,42	0,04493
Tmem181a	-0,50	0,71	0,01863

Vsnl1	-0,50	0,71	0,01248
Egr3	-0,50	0,71	0,02021
Gm11883	-0,50	0,71	0,00105
D130012P04Rik	-0,51	0,70	0,00455
AA667203	-0,51	0,70	0,02651
Gm10337	-0,51	0,70	0,00925
Gm11912	-0,51	0,70	0,02735
Optn	-0,51	0,70	0,03637
C5ar1	-0,51	0,70	0,01158
Prkab2	-0,51	0,70	0,03554
Rab1	-0,51	0,70	0,04144
BC094916	-0,51	0,70	0,00068
Gbp10	-0,52	0,70	0,01346
Stard9	-0,52	0,70	0,00078
Tmem181b-ps	-0,52	0,70	0,02214
Dst	-0,52	0,70	0,00756
Trim25	-0,52	0,70	0,00927
Gm7278	-0,52	0,70	0,00211
Gm11261	-0,52	0,70	0,00222
Gm25271	-0,52	0,70	0,02986
Mir342	-0,52	0,70	0,04072
Mir342	-0,52	0,70	0,04072
Mir221	-0,52	0,70	0,01455
G2e3	-0,52	0,70	0,00987
Lilra5	-0,52	0,70	0,02375
Man1a	-0,52	0,70	0,02555
Grap	-0,52	0,70	0,00432
Gm22060	-0,53	0,69	0,02348
Rbbp8	-0,53	0,69	0,02864
Gm21886	-0,53	0,69	0,00089
Dock4	-0,53	0,69	0,00354
Gm14737	-0,53	0,69	0,00421
Mir3074-1	-0,53	0,69	0,00733
Peg10	-0,54	0,69	0,00122
Bzw1	-0,54	0,69	0,04535
Gm25109	-0,54	0,69	0,02185
Gm12812	-0,54	0,69	0,00682
Mir325	-0,54	0,69	0,02566
Phxr4	-0,54	0,69	0,02530
Il12rb2	-0,54	0,69	0,00860
Ifnb1	-0,54	0,69	0,02909
Fth-ps2	-0,54	0,69	0,02475
Mir103-2	-0,54	0,69	0,01741
Gm14265	-0,55	0,69	0,00105
Gm11886	-0,55	0,68	0,00037
Ptpn23	-0,55	0,68	0,01372

Gm14888	-0,55	0,68	0,00196
Ifitm3	-0,55	0,68	0,02003
4930486L24Rik	-0,56	0,68	0,02427
Gm13570	-0,56	0,68	0,00473
Gm23121	-0,56	0,68	0,02856
Camkk2	-0,56	0,68	0,02477
Gm12840	-0,56	0,68	0,00735
Gem	-0,56	0,68	0,04839
Cryba4	-0,56	0,68	0,00759
Gm15186	-0,56	0,68	0,01144
Lilrb3	-0,57	0,68	0,00540
Gm11652	-0,57	0,68	0,00792
Gm26857	-0,57	0,67	0,00084
Btaf1	-0,57	0,67	0,02151
Oasl2	-0,57	0,67	0,01245
Zfhx3	-0,57	0,67	0,01429
mmu-mir-6541	-0,57	0,67	0,01666
Gm11995	-0,58	0,67	0,00220
Gm5844	-0,58	0,67	0,03148
B230325K18Rik	-0,58	0,67	0,03465
AC168977.2	-0,58	0,67	0,00276
Abl2	-0,58	0,67	0,00048
Gm15368	-0,58	0,67	0,02492
Gm13710	-0,58	0,67	0,00238
Enpp4	-0,58	0,67	0,00110
Hbb-bs	-0,58	0,67	0,00245
Tmem181c-ps	-0,58	0,67	0,02008
RP23-142E18.5	-0,58	0,67	0,00388
AW046200	-0,58	0,67	0,02614
Gm26520	-0,58	0,67	0,00083
Cd40	-0,58	0,67	0,00127
Bco2	-0,58	0,67	0,00621
Lonrf1	-0,59	0,67	0,02994
Gm26430	-0,59	0,66	0,01300
Stab1	-0,59	0,66	0,00396
Gm13765	-0,59	0,66	0,00488
Gm24273	-0,59	0,66	0,01784
Gm4583	-0,60	0,66	0,02542
BC035044	-0,60	0,66	0,00494
Gm10099	-0,60	0,66	0,00162
Trim30a	-0,60	0,66	0,00517
Hivep1	-0,60	0,66	0,00531
Clec4a3	-0,60	0,66	0,02731
Gm23247	-0,61	0,66	0,00741
LOC432823	-0,61	0,66	0,00350
Pira2	-0,61	0,66	0,00601

Gm10091	-0,61	0,66	0,00730
Trim12c	-0,61	0,65	0,01290
Gm14749	-0,61	0,65	0,00076
Gm19279	-0,61	0,65	0,00960
Gm23734	-0,61	0,65	0,00525
Ddx58	-0,61	0,65	0,01245
Rufy3	-0,62	0,65	0,01806
Gm12346	-0,62	0,65	0,02916
Gm25993	-0,62	0,65	0,04386
Gm23553	-0,62	0,65	0,02554
fasapoptosis	-0,63	0,65	0,01117
Pttg1	-0,63	0,65	0,00481
ST7-OT4_4	-0,63	0,65	0,01146
Gm23730	-0,63	0,65	0,04994
Crybb1	-0,63	0,65	0,00121
Gm19703	-0,63	0,65	0,03090
Gm22888	-0,63	0,65	0,02123
Xdh	-0,63	0,65	0,00189
Elmo1	-0,63	0,65	0,00264
LOC432823	-0,63	0,64	0,00118
Gm13519	-0,64	0,64	0,00014
Swap70	-0,64	0,64	0,00670
Atp6v1d	-0,64	0,64	0,00667
Gm12437	-0,64	0,64	0,00637
Gm24198	-0,64	0,64	0,00793
Olfr755-ps1	-0,64	0,64	0,00342
Tank	-0,64	0,64	0,01364
Gm20689	-0,64	0,64	0,00353
LOC432823	-0,64	0,64	0,00119
Ap4s1	-0,64	0,64	0,00272
Ccl5	-0,64	0,64	0,00138
Parp14	-0,65	0,64	0,00500
Gm25966	-0,65	0,64	0,04124
Mir5124	-0,65	0,64	0,00191
Gm4992	-0,65	0,64	0,00091
Gm24959	-0,65	0,64	0,04018
Pira1	-0,65	0,64	0,00416
Lst1	-0,66	0,63	0,00020
Gm17024	-0,66	0,63	0,01789
Gm22731	-0,66	0,63	0,00089
Gm14063	-0,66	0,63	0,00081
Tnfsf9	-0,66	0,63	0,00486
Dock10	-0,66	0,63	0,01132
mmu-mir-7679	-0,67	0,63	0,00269
Gm11545	-0,67	0,63	0,03635
Ifit2	-0,67	0,63	0,01858

Gm15971	-0,67	0,63	0,01723
Epha2	-0,67	0,63	0,00059
Gm14814	-0,68	0,63	0,00066
Dapp1	-0,68	0,62	0,02917
Gm10933	-0,68	0,62	0,02700
Ccl9	-0,69	0,62	0,00623
B230217C12Rik	-0,69	0,62	0,03068
Gm11753	-0,70	0,62	0,02018
Trim30b	-0,70	0,62	0,00500
Gbp7	-0,70	0,62	0,00481
Usp18	-0,70	0,62	0,00747
Lgals3bp	-0,70	0,61	0,01330
Mir505	-0,70	0,61	0,00683
Gm14941	-0,70	0,61	0,00168
4930594C11Rik	-0,70	0,61	0,02950
Gm13701	-0,71	0,61	0,00295
Gm14702	-0,71	0,61	0,00272
Gm13468	-0,71	0,61	0,00150
Gm20100	-0,71	0,61	0,01098
Gm14928	-0,72	0,61	0,00041
Slc2a5	-0,72	0,61	0,04417
Gm14672	-0,72	0,61	0,00682
Gm14654	-0,72	0,61	0,00273
AC133103.3	-0,73	0,60	0,00307
Sp100	-0,73	0,60	0,00112
Odc1	-0,73	0,60	0,00066
LOC432823	-0,73	0,60	0,00098
Gm3513	-0,74	0,60	0,00047
Gm23136	-0,74	0,60	0,01239
Gm16558	-0,74	0,60	0,00619
Gm13357	-0,75	0,60	0,02617
Gm14969	-0,75	0,60	0,00006
Baiap2	-0,75	0,60	0,00328
D130007C19Rik	-0,75	0,59	0,02376
Gm14700	-0,75	0,59	0,00554
Slfn8	-0,75	0,59	0,00337
n-R5s47	-0,76	0,59	0,03126
Hba-a1	-0,76	0,59	0,00696
Gm14708	-0,76	0,59	0,00041
Gm15470	-0,77	0,59	0,00056
Gm4955	-0,77	0,59	0,00357
Bank1	-0,78	0,58	0,00235
Rtp4	-0,78	0,58	0,01008
Gm13574	-0,78	0,58	0,00300
F830016B08Rik	-0,79	0,58	0,00251
Mnda	-0,79	0,58	0,01373

Sorl1	-0,80	0,57	0,00434
Gm14778	-0,80	0,57	0,00150
mmu-mir-6963	-0,80	0,57	0,02001
Gm12197	-0,80	0,57	0,00454
Gm24783	-0,80	0,57	0,02781
Gm23300	-0,81	0,57	0,00019
Gm9115	-0,81	0,57	0,00033
Gm13840	-0,81	0,57	0,00294
LOC215866	-0,82	0,57	0,00570
4931406H21Rik	-0,82	0,57	0,02206
Trim5	-0,82	0,57	0,00059
6330407A03Rik	-0,82	0,56	0,00995
Gm11187	-0,83	0,56	0,00978
Gm15371	-0,84	0,56	0,00617
Gm15146	-0,84	0,56	0,01155
Gm17709	-0,85	0,56	0,00047
Gm14734	-0,85	0,56	0,01189
Mir15a	-0,85	0,55	0,00627
Hbb-bt	-0,85	0,55	0,01025
Gm15724	-0,87	0,55	0,00719
Gm19313	-0,87	0,55	0,00434
mmu-mir-6972	-0,88	0,54	0,00057
Il1f9	-0,89	0,54	0,04514
Gm13018	-0,89	0,54	0,01099
Mir3075	-0,90	0,54	0,01756
Rbpms	-0,90	0,54	0,01504
Gm12651	-0,90	0,53	0,00344
Ggta1	-0,91	0,53	0,00016
Hba-a1	-0,92	0,53	0,00501
Mrgpra2a	-0,92	0,53	0,00867
Ccl12	-0,92	0,53	0,01106
Mir5123	-0,92	0,53	0,01465
Nlrp1b	-0,92	0,53	0,00150
Gm14693	-0,93	0,53	0,00987
Mir146	-0,93	0,53	0,01968
Gm24112	-0,94	0,52	0,00961
Gm24927	-0,94	0,52	0,00387
Trim12a	-0,96	0,52	0,00015
Rsad2	-0,96	0,51	0,00140
Ifi27l2a	-0,98	0,51	0,00309
Gm25931	-0,98	0,51	0,00977
Myo1g	-0,99	0,51	0,00223
Gm12424	-0,99	0,50	0,00434
Gm14604	-1,00	0,50	0,00655
Gm25138	-1,00	0,50	0,00008
Gm25549	-1,02	0,49	0,00176

Gm11247	-1,03	0,49	0,00370
Gm24842	-1,04	0,49	0,01264
AI607873	-1,04	0,49	0,00396
Gm11522	-1,04	0,49	0,00053
Oas2	-1,04	0,49	0,00080
Ifi204	-1,08	0,47	0,00323
2610024D14Rik	-1,08	0,47	0,01072
Gm12785	-1,11	0,46	0,01148
Gm14060	-1,13	0,46	0,00329
Rnf213	-1,13	0,46	0,00128
Pyhin1	-1,14	0,45	0,00104
Oas1g	-1,16	0,45	0,00122
Gm26497	-1,20	0,44	0,02295
G530011O06RIK	-1,23	0,43	0,01047
Hsph1	-1,24	0,42	0,02032
Oas1a	-1,27	0,41	0,00445
Gm14801	-1,28	0,41	0,01429
Fpr1	-1,33	0,40	0,03973
Gm15445	-1,33	0,40	0,00402
Trim30c	-1,36	0,39	0,00023
Cwc22	-1,37	0,39	0,02667
Mid1	-1,42	0,37	0,00080
Mir34a	-1,50	0,35	0,00314
Gm25720	-1,53	0,35	0,00720
Gm15064	-1,53	0,35	0,02397
Gm13800	-1,56	0,34	0,01458
Zfp125	-1,56	0,34	0,00001
Gm13691	-1,57	0,34	0,03382
Gm21742	-1,65	0,32	0,00022
Nlrp1c-ps	-1,67	0,31	0,00183
Trim30d	-1,72	0,30	0,00832
S100a9	-1,81	0,29	0,02556
Gm13695	-1,81	0,29	0,02972
Gm13698	-1,81	0,29	0,03023
Gm13693	-1,81	0,29	0,03023
Gm13696	-1,81	0,29	0,03023
Gm13694	-1,81	0,29	0,03023
Gm13697	-1,81	0,29	0,03023
Retnlg	-1,93	0,26	0,03561
Gm22748	-2,13	0,23	0,00000
S100a8	-2,29	0,20	0,04194
Egln3	-3,48	0,09	0,00000

Table 5. Transcriptional changes in isolated microglia from *Egln3* $^{-/-}$; *App-Psen1 versus App-Psen1* mice.

Up-regulated and down-regulated genes in 12-month-old isolated microglia from *Egln3* $^{-/-}$; *App-Psen1 versus App-Psen1* mice (logFC ≥ ±0.5, $p < 0.05$).

9.2. Figure index

9.3. Table index